ISTANBUL TECHNICAL UNIVERSITY ★ GRADUATE SCHOOL

DEFINING DENUDATION RATES IN CARBONATE ROCKS USING COSMOGENIC ^{36}Cl

Ph.D. THESIS

Ayda HASHEMI

Department of Solid Earth Sciences

Geodynamics Programme

JANUARY 2024

ISTANBUL TECHNICAL UNIVERSITY ★ GRADUATE SCHOOL

DEFINING DENUDATION RATES IN CARBONATE ROCKS USING COSMOGENIC ^{36}Cl

Ph.D. THESIS

Ayda HASHEMI
(602162002)

Department of Solid Earth Sciences

Geodynamics Programme

Thesis Advisor: Prof. Dr. Mehmet Akif SARIKAYA

JANUARY 2024

ISTANBUL TEKNİK ÜNİVERSİTESİ ★ LİSANSÜSTÜ EĞİTİM ENSTİTÜSÜ

KARBONATLI KAYAÇLARIN DENÜDASYON HIZININ KOZMOJENİK ^{36}Cl KULLANILARAK BELİRLENMESİ

DOKTORA TEZİ

Ayda HASHEMI
(602162002)

Katı Yer Bilimleri Anabilim Dalı

Jeodinamik Programı

Tez Danışmanı: Prof. Dr. Mehmet Akif SARIKAYA

OCAK 2024

Ayda HASHEMI, a Ph.D. student of ITU Graduate School student ID 602162002, successfully defended the thesis entitled "DEFINING DENUDATION RATES IN CARBONATE ROCKS USING COSMOGENIC ^{36}Cl", which she prepared after fulfilling the requirements specified in the associated legislations, before the jury whose signatures are below.

Thesis Advisor :	**Prof. Dr. Mehmet Akif SARIKAYA** Istanbul Technical University	……
Jury Members :	**Prof. Dr. Tolga GÖRÜM** Istanbul Technical University	……
	Assoc. Prof. Dr. Muhammed Zeynel ÖZTÜRK Niğde Ömer Halisdemir University	…….
	Prof. Dr. Gürsel SUNAL Istanbul Technical University	……...
	Assoc. Prof. Dr. Cihan BAYRAKDAR Istanbul University	……

Date of Submission : 25 December 2023
Date of Defense : 31 January 2024

To my beloved mother, Roghaiyeh JABBARIVAND SADABAD, for her endless love and support throughout my life,

FOREWORD

First and foremost, I would like to express my deepest gratitude to my mother, Roghaiyeh JABBARIVAND SADABAD, and my father, Seyedkarim HASHEMI, for their emotional and financial support and continuous encouragement throughout my Ph.D. journey. Without their help, I would never have been able to complete my studies. I am so thankful for everything you have done for me.

I wish to express my sincere appreciation to my supervisor, Prof. Dr. Mehmet Akif SARIKAYA, for generously sharing his knowledge with me and for his continuous support and guidance. I am also thankful to him for providing a field trip to my study area and teaching me cosmogenic nuclide procedures.

I am so thankful to Prof. Dr. Aral OKAY and Prof. Dr. Gültekin TOPUZ for providing access to their laboratory for the sample preparation. I am very grateful to Prof. Dr. Attila ÇİNER for his invaluable comments on my publications. I appreciate my thesis committee members, Prof. Dr. Tolga GÖRÜM and Assoc. Prof. Dr. Muhammed Zeynel ÖZTÜRK for their time and valuable feedback on my thesis. Furthermore, I would like to thank Assoc. Prof. Dr. Orkan ÖZCAN for his help in processing aerial photos. Thanks should also go to Mr. Mahir ALTINBAĞA for his help with cutting my rock samples in the laboratory. I am thankful to Mr. Yüksel İLGAR for providing access to their laboratory and for his help in measuring the physical properties of rock samples. Many thanks to Prof. Dr. Cengiz YILDIRIM, Prof. Dr. Uroš STEPIŠNIK, Dr. Manja ŽEBRE, Dr. Oğuzhan KÖSE, Şeyma YILDIZ KÖSE, and Onur ALTINAY for their assistance during the fieldwork. I also appreciate Dr. Oğuzhan KÖSE's help with sample preparation in the İTÜ/KozmoLab during the Covid-19 lockdown.

I would like to give special thanks to my sister, Zahra HASHEMI, for always being there for me. Thanks a lot for accompanying me through the good and bad days. I am so grateful to have had you by my side.

Some people have a remarkable impression on our lives, and so was my master supervisor, Dr. Behnam OVEISI. His positive attitude, guidance, and motivation left an unforgettable impression on my life and inspired me throughout my Ph.D.

Finally, I praise ALLAH for bringing me success after hardship and helping me fulfill my long-held dream of pursuing a Ph.D. degree.

This thesis was supported by the Istanbul Technical University BAP Project [grant number MDK-2019-42116], and TÜBİTAK [grant number 118Y052]. Moreover, I appreciate the financial support from the Australian Government for the Centre for Accelerator Science at ANSTO (#AP12630) through the National Collaborative Research Infrastructure Strategy (NCRIS).

January 2024

Ayda HASHEMI
(Geologist)

TABLE OF CONTENTS

Page

FOREWORD ..... **ix**
TABLE OF CONTENTS ..... **xi**
ABBREVIATIONS ..... **xiii**
SYMBOLS ..... **xv**
LIST OF TABLES ..... **xvii**
LIST OF FIGURES ..... **xix**
SUMMARY ..... **xxiii**
ÖZET ..... **xxv**
1. INTRODUCTION **1**
1.1 Literature Review and Research Gap 2
1.1.1 ^{36}Cl-derived denudation rate of carbonates 2
1.1.2 ^{36}Cl surface exposure dating of prehistorical rock slope fauliers 4
1.2 Research Objectives 6
1.3 Thesis Outline 7
2. LITERATURE REVIEW **9**
2.1 Worldwide ^{36}Cl-derived Denudation Rates and Controling Factors 9
2.2 Surface Exposure Dating of Prehistoric Rock Slope Failures (RSF) 12
3. STUDY AREA **17**
3.1 Study Area of ^{36}Cl-derived Denudation Rates of Carbonate Outcrops 17
3.1.1 Geology 17
3.1.2 Climate 19
3.2 Study Area of the Namaras Rock Avalanche 22
4. MATERIALS AND METHODS **25**
4.1 Terrestrial Cosmogenic Nuclide (TCN) 25
4.1.1 Cosmic ray origins and in-situ ^{36}Cl production rates 25
4.1.2 Application of ^{36}Cl for quantifying the rate and age of surface processes 26
4.1.2.1 Surface exposure dating of rock avalanche blocks 26
4.1.2.2 ^{36}Cl-derived denudation rate of carbonate outcrops 27
4.1.3 Field sampling procedures 28
4.1.3.1 Sampling carbonate bedrocks for denudation studies 28
4.1.3.2 Sampling rock avalanche boulders for surface exposure dating 29
4.1.4 Chemical preparation 30
4.1.5 Calculations 31
4.1.5.1 Calculation of ^{36}Cl-derived denudation rates 31
4.1.5.2 Calculation of surface exposure ages 32
4.2 Compilation of Climatic and Topographic Metrics and Measuring Physical Properties of denudation samples 33
4.2.1 Climatic and topographic metrics 33
4.2.2 Schmidt Hammer measurements 33
4.2.3 Measuring bulk density, prosity and water absorption by weight 34
4.3 Geomorphological Analysis of the Rock Avalanche 34
5. LONG-TERM DENUDATION RATE OF CARBONATE OUTCROPS **37**

5.1 Results 37
5.1.1 ^{36}Cl-derived denudation Rates 37
5.1.2 Rock mechanical strength and physical properties 42
5.1.3 Correlation of ^{36}Cl- derived denudation rates with environmental and physical variables 43
5.2 Discussion 46
5.2.1 Sensitivity of denudation rates to bedrock bulk densities 46
5.2.2 Interpretation of denudation rates and controlling factors 47
5.2.2.1 Climatic control 47
5.2.2.2 Topographic/tectonic control 51
5.2.2.3 Lithologic control 53
5.2.3 Comparison of denudation rates with global records 54
6. THE NAMARAS RACK AVALANCHE: A MID-TO-LATE HOLOCENE PARAGLACIAL ACTIVITY IN THE CENTRAL TAURIDES 57
6.1 Results 57
6.1.1 Geomorphology of the Namaras rock avalanche (NRA) 57
6.1.2 Cosmogenic ^{36}Cl exposure dating results 66
6.2 Discussion 69
6.2.1 Preconditioning, preparatory and triggering factors 69
6.2.2 The comparison of the NRA with other mid-Holocene RSFs 74
7. CONCLUSIONS AND RECOMMENDATIONS 77
7.1 Conclusions 77
7.1.1 Conclusions concerning the ^{36}Cl-derived denudation rate of carbonate outcrops and their controlling factors 77
7.1.2 Conclusions concerning the age and geomorphology of the paraglacial Namaras rock avalanche 78
7.2 Recommendations 80
REFERENCES 81
APPENDICES 99
CURRICULUM VITAE 119

ABBREVIATIONS

AMS : Accelerator mass spectrometry
cal BP : Calibrated before present
CAP : Central Anatolian Plateau
CP : Central Pontides
CT : Central Taurides
DEM : Digital elevation model
EAF : Eastern Anatolian Fault
EAP : Eastern Anatolian Plateau
ELA : Equilibrium line altitude
Fm. : Formation
HMD : Hummocky moraine debris
ICP-MS : Inductively coupled plasma mass spectrometry
LGM : Last glacial maximum
LMD : Lateral moraine debris
MAP : Mean annual precipitation
MAT : Mean annual temperature
m asl : meters above sea level
NAF : North Anatolian Fault
NRA : Namaras Rock Avalanche
RFD : Rock fall debris
RSF : Rock slope failure
SLHL : Sea level high latitude
SRTM : Shuttle Radar Topography Mission
ST : Stone (2000) scaling (Scalling to local production rate of ^{36}Cl)
TCN : Terrestrial cosmogenic nuclides
UAV : Unmanned aerial vehicle
WAEP : Western Anatolian Extensional Province
WT : Western Taurides

SYMBOLS

AgCl	**:** Silver chloride
$Ba(NO_3)_2$	**:** Barium nitrate
^{10}Be	**:** Beryllium-10
$C_{(t)}$	**:** Cosmogenic nuclide concentration
C_{in}	**:** Inherited cosmogenic nuclide concentration
^{40}Ca	**:** Calcium-40
^{36}Cl	**:** Chlorine-36
^{35}Cl	**:** Chlorine-35
^{37}Cl	**:** Chlorine-37
CO_2	**:** Carbon Dioxide
D_{max}	**:** Maximum dissolution rate
HNO_3	**:** Nitric acid
^{39}K	**:** Potassium-39
ka	**:** Kilo annum (one-thousand years)
km	**:** Kilometer
K_1, K_2	**:** Equilibrium constants
K_C	**:** Calcite equilibrium constant
K_{CO2}	**:** Henry's law constant for CO_2
mm/ka	**:** millimeter per kilo annum
NaCl:	**:** Sodium chloride
$P_{(0)}$	**:** Production rate at the surface of rock
pCO_2	**:** CO_2 partial pressure
P–E	**:** Precipitation minus evapotranspiration
ppm	**:** Parts per million
σ	**:** Standart deviation
ε	**:** Erosion rate
ρ	**:** Density of rock or soil
λ	**:** Decay constant of nuclide of interest
Λ	**:** Attenuation length

LIST OF TABLES

Page

Table 4. 1 : Location, climate, topographic data, and local corrections to production rates for denudation samples. **29**
Table 4. 2 : Location, topographic data and local corrections to production rates for rock avalanche samples. **30**
Table 4. 3 : Major and trace element concentrations for denudation samples. **31**
Table 4. 4 : Major and trace element concentrations for rock avalanche samples.... **31**
Table 5. 1 : AMS analytical data and denudation rate results. **38**
Table 5. 2 : Physical properties of denudation samples. **42**
Table 6. 1 : Surface exposure ages of rock avalanche and moraine boulders. **66**
Table A. 1 : Major and trace elemens, AMS results, blank and spike data, and corrections to local production rates for denudation samples. **100**
Table A. 2 : Major and trace elemens, AMS results, blank and spike data, and corrections to local production rates for the rock avalanche samples. **103**
Table A. 3 : Compilation of ^{36}Cl-derived denudation rates for carbonate bedrock samples in the previous studies **106**
Table B. 1 : Schmidt Hammer measurements in each sampling location. **116**

LIST OF FIGURES

Page

Figure 3. 1 : (a) The carbonate outcrops extracted from a 1/500,000 geological map of the General Directorate of Mineral Research and Exploration of Türkiye (MTA). The simplified tectonic setting of the Anatolia is shown on the map: CAP (Central Anatolian Plateau); CT (Central Taurides); WT (Western Taurides); CP (Central Pontides); EAP (Eastern Anatolian Plateau); WAEP (Western Anatolian Extensional Province); NAF (North Anatolian Fault); EAF (Eastern Anatolian Fault). (b) Shaded relief map of the study area. White lines delineate the karstic doline areas, simplified from the Öztürk et al. (2018). The red box in (a) and (b) shows the study area (Figures 3.2a-d, and 5.1a). Two black boxes outline the location of elevation swath profiles along Transects A and B (Figures 5.7a and 5.7c). This figure was taken from Hashemi et al. (2023). **19**

Figure 3. 2 : (a) The map shows three sampled lithostratigraphic units, including two carbonate units and one marble unit. The white area shows an undifferentiated lithology. (b) Climate zones in the study area were derived from the Köppen-Geiger climate classification (Beck et al., 2018). (c) Mean annual precipitation map was derived from WorldClim 2.1 (Fick and Hijmans, 2017). Dark blue solid lines (isohyetal contours) show the distribution of mean annual precipitation (mm). (d) Map of mean annual temperature was derived from WorldClim 2.1 (Fick and Hijmans, 2017). The white shaded boxes in (c) and (d) outline the location of swath profiles (Figures 5.7b and 5.7d). This figure was taken from Hashemi et al. (2023)..... **21**

Figure 3. 3 : (a) The red box on the world map shows the extent of the map on the left. The overview map on the left is the Digital Elevation Model of Western and Central Taurides. The yellow box shows the location of the Namaras rock avalanche (Figure 3.3b). The location of Akdağ R.A. (rock avalanche) (Bayrakdar et al., 2020b) in the Western Taurides is marked on the map. (b) Digital Elevation Model (DEM) of the Geyikdağ Mountain. Moraine ages of the previously studied glacial valleys are from Çiner et al. (2015b) and Sarıkaya et al. (2017). The large box indicates the extent of geological map on the right. The black small box indicates the extent of NRA slope map (Figure 6.2) and the NRA geomorphological map (Figure 6.5). (c) The simplified geological map of NW of the Geyikdağ Mountain (data from the 1/25,000 geological map of Alanya, MTA). This figure was taken from Hashemi et al. (2022). **23**

Figure 5. 1 : (a) Shaded relief map of the study area showing sampling sites and ^{36}Cl-derived outcrop denudation rates. Sample names are abbreviated to 1–13 and are shown inside the circle. (b) Scatter plot of ^{36}Cl-derived denudation rates (mm/ka). Diamond, circle, and triangle symbols indicate the Mediterranean coastal region (Med. Cst.), the Central

Taurides, and the Central Anatolian Plateau (CAP) interior, respectively. Green, yellow, and blue colors represent Jurassic-Cretaceous limestone (jka), Miocene limestone (m2a), and Middle Triassic-Jurassic marble (mr), respectively, on the geological map (Figure 3.2a). The gray area shows the samples of the Central Taurides. The error of the points without a visible error bar is smaller than the symbol. (c) Boxplots for "All samples" and for "Central Taurides samples". The associated box shows 25th and 75th percentiles, the median (red vertical line), and the mean (green multiplication sign). The whiskers indicate the data range, excluding the statistical outlier (red cross sign). This figure was taken from Hashemi et al. (2023). **39**

Figure 5. 2 : Field photographs of the sampling sites. (a) and (b) sampling sites on the hilltops of Jurassic-Cretaceous neritic limestones. (c) Sampling site on the flat plateau with Miocene neritic limestone. (d) and (e) sampling sites on the hilltops of marble domes. The red arrow indicates the sampling locations. This figure was taken from Hashemi et al. (2023). **40**

Figure 5. 3 : Field photographs of sampling sites in the Central Taurides. (a), (b), and (c): sampling sites on the hilltops of Jurassic-Cretaceous neritic limestones. (d), (e), (f), (g), and (h): Sampling sites on the flat plateau with Miocene neritic limestone. The red arrow indicates the sampling locations. This figure was taken from Hashemi et al. (2023). **41**

Figure 5. 4 : Scatter plot of ^{36}Cl-derived denudation rates as a function of climatic and topographic variables: (a) elevation (m), (b) distance from the coastline (km), (c) mean annual precipitation (MAP) (mm), (d) mean annual temperature (MAT) (°C), and (e) latitude (°N). For all plots, the regression line belongs to the plateau samples. The two samples (DEN-01 and DEN-02) in the Mediterranean coastal region (diamond symbols with gray error bars) were removed from the regression analysis. The regression lines are shown in red. The error of the points without a visible error bar is smaller than the symbol. This figure was taken from Hashemi et al. (2023). **44**

Figure 5. 5 : Scatter plot of ^{36}Cl-derived denudation rates versus physical properties of carbonate rocks. (a) Schmidt Hammer rebound values (R-values), (b) porosity (%), and (c) water absorption by weight (%). The regression line belongs to the samples on the plateau. The two samples (DEN-01 and DEN-02) in the Mediterranean coastal region (diamond symbols with gray error bars) were removed from the regression analysis. For the interpretation of the symbols and colors see Figure 5.4. This figure wass taken from Hashemi et al. (2023). **45**

Figure 5. 6 : (a) Calculated denudation rates vs. theoretical maximum dissolution rates of the samples. The red line shows the 1:1 relationship. (b) Theoretical denudation rates for three different temperatures (5, 10, and 25 °C), representative of arctic-alpine, temperate, and tropical climates, and CO_2 pressures of $10^{-3.5}$, $10^{-2.5}$, and $10^{-1.5}$, representative of bare bedrock, normal soils, and organic-rich soils, respectively. We plotted our calculated denudation rates (blue circles) on the theoretical denudation curves. P-E is precipitation minus evapotranspiration. We assumed zero evaporation. This figure was taken from Hashemi et al. (2023), which they adapted from White (1984). **48**

Figure 5. 7 : (a) and (c) Elevation swath profiles, extracted from the 30 m DEM with a vertical exageration of 24, along transects A and B, respectively. (b) and (d) The mean annual precipitation (MAP) and mean annual temperature (MAT) swath profiles, extracted from the WorldClim v.2.1 along transects A and B, respectively. Abbreviations stand for P. (Plateau), B. (Basin), E.B. (Ermenek Basin). The location of transects are shown in Figures 3.1b, 3.2c and 3.2d. The width of the swath profiles is 26 km. This figure wass taken from Hashemi et al. (2023)..... **50**

Figure 5. 8 : (a) Denudation rate of carbonate bedrocks for all previous studies. (b) Denudation as a function of mean annual precipitation for all previous studies. The study of Marrero et al. (2018) was excluded from the precipitation graph because of uncertainty in precipitation data in Antarctica, as mentioned by the authors. This figure wass taken from Hashemi et al. (2023). **56**

Figure 6. 1 : (a) 3D view of the Namaras rock avalanche. RFD: rock fall debris, HMD: hummocky moraine debris, LMD: lateral moraine debris (b) Overall view of the Namaras rock avalanche indicating release area, travel path and deposit area. Sampling sites are marked on the photo: The blue and white colors indicate the location of the sampled boulders of the lateral moraine and the rock avalanche deposit, respectively. This figure was taken from Hashemi et al. (2022). **58**

Figure 6. 2 : Slope map of the Namaras rock avalanche and the surrounding area. Blue, white and yellow colors delineate the source area of the rock avalanche, older event deposit and younger event deposit, respectively. The black dashed line shows the travel path of the rock avalanche. This figure was taken from Hashemi et al. (2022). **59**

Figure 6. 3 : (a) A close view of the source area with the bedded limestone and joints on it. (b) A view towards the north from the NRA deposit. The orange and yellow lines delineate the boundary of the older and younger rock avalanche deposits, respectively. Sampling sites with blue, orange and yellow colors belong to moraine, older, and younger deposit boulders, respectively. (c) A close view of the black dashed box in (b). The red ovals show two people for scale. This photo shows huge boulders of the rock avalanche with 30-m run-up over the lateral moraine on the opposite side. This figure was taken from Hashemi et al. (2022)..... **61**

Figure 6. 4 : (a) Orthophoto with a resolution of 19-cm produced from high resolution aerial photos. The red color delineates the younger deposit. (b) The boulder size map of the rock avalanche deposit extracted from 19-cm resolution orthophoto. Darker and lighter colors indicate longer and shorter boulder lengths, respectively. (c) The rock avalanche block density distribution per 100 m^2. (d) This figure shows the block area density per 100 m^2. This figure was taken from Hashemi et al. (2022). **62**

Figure 6. 5 : Geomorphological map of the Namaras rock avalanche. S1 and S2 indicate traces of two across deposit topographic sections (Figure 6.6a). White lines (A–B, C–D, E–F) show traces of longitudinal profiles presented in Figure 6.6b. The outlier moraine sample is indicated in italic font. This figure was taken from Hashemi et al. (2022)..... **64**

Figure 6. 6 : (a) Two across deposit topographic sections (S1 and S2). (b) Three longitudinal profiles along the runout path. The location of sections and

the longitudinal profiles are shown on the geomorphological map (Figure 6.5). A–B, C–D and E–F are longitudinal profiles along the older rock avalanche deposit, the younger rock avalanche deposit and the older deposit and lateral moraine, respectively. Sampling sites are projected on the profiles C–D and E–F. Profile E-F shows deposit run-up over the lateral moraine. Different colors taken from the geomorphological map represent the bedrock outcrop, surface extension of each deposit, and moraines. The color thicknesses are not representative of the deposit thicknesses. Vertical and horizontal scales are equal (V = H). This figure was taken from Hashemi et al. (2022). **65**

Figure 6. 7 : Photo plate of sampled rock avalanche boulders. Three photos in the top row belong to the older deposit. Three photos in the bottom row are from the younger rock avalanche deposit. The location of sampling sites is shown on the field photos (Figures 6.1b and 6.3b) and the geomorphological map (Figure 6.5). This figure was taken from Hashemi et al. (2022)..... **68**

Figure 6. 8 : The two sampled moraine boulders which are located on the lateral moraine crest. This figure was taken from Hashemi et al. (2022)..... **68**

Figure 6. 9 : The probability density function of rock avalanche boulders showing two age clusters. The ages are reported in one sigma uncertainty. This figure was taken from Hashemi et al. (2022). **69**

Figure 6. 10 : Timing of the Namaras rock avalanche concerning the paleoclimatic variations recorded in central and south Türkiye. This figure was modified from Fig. 5 of Dean et al. (2015) and Fig. 2 of Roberts et al. (2011), with some data added from other sources mentioned on the figure. This figure was taken from Hashemi et al. (2022)..... **73**

Figure A. 1 : Field photos of sampling locations. P. stands for plateau..... **113**

Figure A. 2 : Sampling carbonate bedrocks for quantifying denudation rates..... **115**

Figure A. 3 : Some steps of sample preparation: A) Leaching with MilliQ water, B) Leaching with 10 % HNO_3, C) First Chlorine extraction, D) The final centrifuge to precipitate AgCl, E) AgCl precipitation in labeled Teflon vial. **115**

Figure B. 1 : Schmidt Hammer measurements in the field. **116**

DEFINING DENUDATION RATES IN CARBONATE ROCKS USING COSMOGENIC ^{36}Cl

SUMMARY

Quantifying the rate and type of erosional processes under different climate and tectonic settings are fundamental to understanding landscape evolution. Carbonate rocks may respond differently to climate and tectonic forcings from other rock types because of their tendency to dissolve congruently. Yet, there is little information on the long-term denudation rate of carbonate rocks and their controlling factors in different settings. This study presents the first detail information on the long-term denudation rate of carbonate rocks and their denudation style in the south of the Central Anatolian Plateau (CAP). The outcrop denudation rates were quantified using in-situ cosmogenic ^{36}Cl measured in 13 rock samples to evaluate spatial variations and potential controls on the style and rate of denudation. ^{36}Cl-derived denudation rates range from 1.92 ± 0.31 to 45.77 ± 3.91 mm/ka. On the plateau, denudation rates are strongly correlated with precipitation values in the area. The denudation rates are lower than the theoretical maximum dissolution rates predicted assuming zero evaporation, implying that climate exerts the major control on carbonate denudation. These results indicate that chemical weathering is the prevalent denudation style in the region. The denudation pattern of the study area shows spatial variability with a decreasing trend from SW to NE consistent with climate zones. High-to-moderate denudation rates occur in the continental climate of Central Taurides, while the lowest denudation rates occur in the arid CAP interior. In the Mediterranean coastal region, measured denudation rates are higher than the predicted maximum dissolution rates, reflecting a possible mechanical removal of overlying rock or soil in sampling locations. The low denudation rates in the plateau interior indicate a slowly evolving landscape with prolonged arid climate. The overall physical properties of sampled rocks, such as rock hardness, porosity and water absorption by weight, showed the weakest control on carbonate denudation. In the Central Taurides, significant infiltration of surface runoff resulted in strong subsurface karstification at the expense of surface drainage. This process caused disequilibrium between uplift and denudation and resulted in the preservation of high-elevation topography. Therefore, in the actively uplifting plateau margin, the influence of tectonics on carbonate denudation has been interfered with the impact of precipitation and subsurface karstification.

This thesis also investigated an example of instantaneous (i.e., short-term or episodic) denudation of carbonate rocks in the Central Taurides. The geomorphology and timing of an example of a rapid mass movement, the Namaras rock avalanche (NRA), were studied using cosmogenic ^{36}Cl. The NRA originated from the northern flank of the glaciokarstic Geyikdağ Mountain in the Central Taurides. The rock avalanche deposit has an area of ~0.430 km^2 and an estimated average thickness of 10 m, corresponding to 4.3 million m^3 volume. The fan-shaped deposit consists of Jurassic-Cretaceous neritic limestone boulders with <1 to >15 m diameter which sometimes reach house-sized boulders (~22 m) that overlie Late Quaternary aged lateral and hummocky moraines down into the valley. The geomorphological mapping and ^{36}Cl surface

exposure dating were used to obtain the ages of six boulder samples that unraveled the age of NRA, the number of failure events and their geometric features. The results indicate that the NRA consists of two successive mid-to-late Holocene events. The first high magnitude main event was occurred 4.59 ± 0.25 ka ago followed by a second low magnitude event at 3.77 ± 0.20 ka ago. The bedded limestone with cross-joints in the glacial cirque preconditioned the NRA slope failure. The significant lag time between deglaciation and the rock avalanche indicates that the glacial erosion and debuttressing acted as preparatory factors. The low seismic activity in the Central Taurides and the synchronicity of the rock avalanche with mid-to-late Holocene climatic transitions suggest that climatic factors may have triggered the NRA failure. The age of the older, main event coincides with the warm drought period of the mid-Holocene associated with torrential rainfalls in the Taurides, while the age of the younger event correlates with the long-wet period in the late Holocene. Thus, the main NRA event may have been triggered by the influence of warm temperatures and intense rainfall, while the second event may have been triggered by prolonged period of high precipitation. The two events of the NRA are coeval with the enhanced rock slope failures dating back to 5–3 ka in the Alps.

Overall, this thesis investigated the long-term denudation rate and the episodic erosion of carbonate rocks in the northeastern Mediterranean. The conducted geologic and chronologic analysis underlines the dominance of climate control on the erosional processes in this region. While the dissolution denudation (chemical weathering) is the dominant mechanism of the long-term denudation rate of carbonates, the physical mechanism is responsible for episodic rapid mass movements. Further studies can focus on denudation partitioning and quantifying physical erosion and chemical weathering. Moreover, future research can explore the basin-wide denudation rates and establish the timing of more paraglacial rock slope failures in the glaciated ranges of the Central Taurides.

KARBONATLI KAYAÇLARIN DENÜDASYON HIZININ KOZMOJENİK ^{36}Cl KULLANILARAK BELİRLENMESİ

ÖZET

Denüdasyon, kimyasal ayrışma ve fiziksel erozyon nedeniyle oluşan toplam kütle kaybı olarak tanımlanır. Farklı iklim ve tektonik özellikleri olan ortamlarda denüdasyon hızını ve türünü ölçmek, jeolojik olayları anlamak için önemlidir. Karbonat kayaçlar, yüksek çözünme eğilimleri nedeniyle iklimsel ve tektonik süreçlere diğer kaya türlerine göre daha farklı tepki verebilir. Ancak karbonat kayaçlar dünya kıta yüzeyinin önemli bir kısmını kapsamasına rağmen onların uzun süreli aşınma hızları ve farklı ortamlarda bunu kontrol eden faktörler hakkında çok az bilgi bulunmaktadır.

Dünya çapında ve çoğunlukla Akdeniz bölgesinde yapılan önceki çalışmalar karbonatlı kayaçlarda aşınma hızının farklı iklimsel ve topografik faktörler ile etkilediğini göstermektedir. Bu etkenler yağış, sıcaklık, yükseklik, topografik eğim, tepe eğriliği, ana kayaç özellikleri, toprak örtüsü ve CO_2 bulunması ve likenlerin varlığı gibi faktörler olabilir. Önceki çalışmaların çoğu, düşük tektonik aktiviteye sahip bölgelerde daha çok iklimin karbonat denüdasyonu üzerinde etkisine odaklanmıştır. Bu nedenle, orojenik plato kenarları gibi tektonik açıdan aktif olan ve hızlıca yükselen bölgelerde karbonatların denüdasyonu ve tektonik yükselmenin ve iklimin ona etkisi hakkında bilgi eksikliği vardır. Diğer yandan, her ne kadar Orta Anadolu Platosu'nun güney kenarı yükselme oranlarına yönelik çeşitli çalışmaların odak noktası olsa da tektonik, iklim ve erozyon süreçleri arasındaki etkileşimler bu bölgede yeterince anlaşılmamıştır. Özellikle plato kenarını geniş ölçüde kaplayan karbonatlı arazilerin aşınmasına ilişkin araştırma eksikliği bulunmaktadır. Bu çalışma, ilk kez Orta Anadolu Platosu'nun güneyindeki karbonatlı kayaçlarda uzun süreli aşınma hızları, türü ve aşınmayı kontrol eden fiziksel ve çevresel faktörler hakkında detaylı bilgiler sunmaktadır. Bu tezin temel amacı Akdeniz-karasal-kurak iklim bölgeleri arasında ve aktif olarak yükselen orojenik plato kenarında karbonatlı arazilerin aşınma hızındaki mekânsal değişimleri ve aşınmanın türü üzerine etki eden potansiyel faktörleri incelemektir.

Bu çalışmada karbonatlı kayaçlarda denüdasyon hızını ölçmek için 13 adet kaya örneğinde in-situ kozmojenik ^{36}Cl değerleri ölçülmüştür. Denüdasyon hızını belirlemek için sabit durum erozyon modeli kullanıldı. Bu model kozmojenik nüklid konsantrasyonunun sabit durumda olması için yeterli sürenin geçtiğini varsayıyor, buda üretilen kozmojenik nüklid ile bozulma ve erozyon yoluyla kayb olan nüklid sayısının dengeye ulaştığı anlamına gelmektedir. ^{36}Cl örnekleri Akdeniz kıyısından İç Anadolu bölgesine kadar farklı iklimlere sahip üç coğrafi bölgeden alınmıştır. Bu bölgeler güneyden kuzeye doğru Akdeniz kıyı bölgesi, karasal Orta Toroslar ve kurak İç Anadolu bölgelerini kapsıyor. Ayrıca bu örnekler litostratigrafik açıdan üç farklı karbonatlı kayaçtan alınmıştır. Alınan örneklerin kimyasal hazırlığı ve klor ayrıştırılması İTÜ/Kozmo Lab laboratuvarında yapılmıştır. ^{36}Cl'den türetilen denüdasyon hızlarını hesaplamak için CRONUScalc 2.1 MATLAB kodu kullanıldı.

Örnek lokasyonlarına ait ortalama yıllık yağış ve sıcaklık değerleri WorldClim 2.1 veri tabanından, yükseklik ve kıyıya mesafe değerleri ise 1/25,000 basılı topografik haritalar ve 30 metre DEM verilerinden elde edilmiştir. Örnek lokasyonlarında ortalama yıllık yağış değerleri 400 ile 770 mm arasında, ortalama yıllık sıcaklık değerleri 6 ile 16 derece arasında, yükseklik 670 ile 2200 m arasında ve kıyıya mesafe ise 6 ile 195 m arasında değişmektedir. Ek olarak örnek alınan karbonatlı kayaçlarda mekanik sertlik, yoğunluk, gözeneklik ve ağırlığa göre su emme oranı gibi fiziksel özellikler de ölçülmüştür.

^{36}Cl'den türetilen aşınma hızları 1.92 ± 0.31 ile 45.77 ± 3.91 mm/ka arasında değişmektedir. Ortalama denüdasyon hızı tüm örnekler için 14.40 ± 0.47 mm/ka ve yalnız Orta Torosların örnekleri için 13.29 ± 0.50 mm/ka elde edilmiştir. Medyan değeri ise tüm örnekler için 12.42 ± 1.31 mm/ka ve yalnız Orta Toroslar'ın örnekleri için 12.45 ± 0.91 mm/ka elde edilmiştir. Plato üzerinde aşınma hızları bölgedeki yağış değerleriyle güçlü bir şekilde ilişkilidir. Buharlaşmanın olmadığı varsayımıyla tahmin edilen teorik maksimum çözünme hızlarından daha düşük değerlere sahip aşınma hızları, bölgede iklimin ve özellikle yağışın karbonat denüdasyonu üzerinde ana kontrolü sağladığını göstermektedir. Bu sonuçlar bir yandan ve karbonatlı kayaçların mekanik sertliği ile denüdasyon hızları arasındaki zayıf korelasyonun olması diğer yandan, bölgede kimyasal ayrışmanın başlıca aşınma tarzı olduğunu belirtir. Aşınma modeli, iklim bölgeleriyle tutarlı olarak GB'dan KD'ye doğru azalan bir eğilimle mekânsal değişkenlik göstermektedir. Orta Toroslar'ın karasal ikliminde yüksek ve orta dereceli aşınma hızları meydana gelirken, en düşük aşınma hızı kurak plato içinde meydana gelmektedir. Akdeniz kıyı bölgesinde ölçülen aşınma oranları, tahmin edilen maksimum çözünme hızlarından daha yüksektir. Bu durum örnek alınan lokasyonlarda üstteki kaya veya toprak örtüsünün mekanik olarak kalkmış olabileceğini göstermektedir. Platonun iç kısmındaki düşük aşınma oranları, uzun süreli kurak iklime sahip, yavaş gelişen bir ortama işaret etmektedir. Yapılan kaya sertliği, gözeneklik ve ağırlığa göre su emme oranı analizleri kayaçların fiziksel özelliklerinin karbonat aşınımı üzerinde pek fazla etkili olmadığını göstermektedir.

Plato kenarında asimetrik yağış modeli asimetrik aşınma modeline sebebiyet veriyor. Bu aşınma modeli aynı anda asimetrik yükselme modeli ile de uyumludur ve aşınmanın, yağışın ve tektonik yükselmenin birbiriyle bağlantılı ve etkileşimde olduğunu göstermektedir. Diğer yandan yükselme oranlarının aşınma hızlarından kaç kat daha yüksek olması hala dengeye ulaşmayan bir ortamı göstermektedir. Orta Toroslar'da yüzey sularının önemli ölçüde derine sızması, bölgede güçlü bir karstlaşmanın olduğunu göstermektedir. Bu süreç zamanla kıtasal yükselme ve aşınma arasında yükselme yanlısı bir dengesizliğe neden olmakta ve Toroslarda yüksek rakımlı topoğrafyanın korunmasına yol açmaktadır. Bu nedenle, aktif olarak yükselen plato kenarlarında, tektonik özelliklerin karbonat aşınması üzerindeki etkisi, yağış ve karstlaşmanın müdahalesiyle kesintiye uğramıştır.

Bu çalışmada Orta Anadolu Platosu'nun güneyinde ölçülen karbonatlı kayaçların uzun süre aşınma hızları daha önce Doğu Akdeniz'de bildirilen aşınma hızlarıyla tutarlı olup, dünya çapındaki kayıtların alt seviyelerinde yer alıyor. Dahası, bu çalışma önceki çalışmalarla tutarlı olarak iklimin ve özellikle yağışın karbonatlı kayaçların aşınmasında en önemli etken olduğunun altını çiziyor.

Ayrıca bu tez kapsamında kısa süreli ve ani aşınma olaylarından bir örnek Orta Toroslar'da incelenmiştir. Kaya çığı, kayması veya düşmesi gibi hızlı kütle hareketleri, ortamı değiştiren ana erozyon süreçleridir. Dağlık alanlarda, buzul nedeniyle dikleşen

yamaçlar, buzul ortadan kalktıktan hemen sonra veya birkaç bin yıl içinde kırılmaya oldukça yatkınlar. Bu şiddetli ve düşük frekanslı olayların yaşını belirlemek, onların oluşmasına sebebiyet veren tektonik ve iklimsel olayları anlamamıza yardımcı olur. Dünya çapında ve özellikle Alpler'de birçok eski kaya çığı ^{36}Cl veya ^{10}Be gibi kozmojenik nüklidler kullanılarak tarihlendirilmiştir. Bu çalışmalar kaya çığlarının genellikle şiddetli hava olayları veya bir sismik aktiviteyle tetiklendiğini göstermektedir. Orta Toroslar'da buzul çökellerinin yüzey yaşlandırması geniş bir biçimde yapılsada, kaya çığları gibi diğer paraglasyal yer şekilleri daha az dikkat çekmiştir. Bu yüzden Türkiye'nin eski buzul alanlarında paraglasyal kaya çığlarının jeomorfolojik haritalanması ve tarihlendirilmesi konusunda bilgi eksikliği mevcuttur.

Bu çalışmada hızlı kütle hareketlerinden bir örnek olarak Namaras kaya çığının (NRA) jeomorfolojisi incelendi ve kozmojenik ^{36}Cl yüzey tarihlendirmesi yapılarak NRA'ın yaşı, olay sayısı ve bunların geometrik özellikleri ortaya çıkarıldı. Jeomorfolojik inceleme amaçlı kaya çığı jeomorfoloji haritası, eğim haritası, blok büyüklüğü haritası, blok dağılım haritası ve üç adet uzunlamasına profil hazırlandı. Ayrıca, kaya çığının birikim alanındaki 6 adet blokun yüzeyinden kozmojenik ^{36}Cl ölçmek için örnek alındı. Buna ek olarak 2 adet örnekte kaya çığı birikim alanı ile kısmen kaplanan yan morendeki bloklardan alındı. NRA, Orta Toroslar'da buzullaşma geçirmiş karstik bir alan olan Geyikdağı'nın kuzey yamacında Jura-Kratese neritik kireçtaşı kayaçlarında gelişmiştir. Kaya çığı birikim alanı yaklaşık ~0.430 km^2'lik bir alana yayılmış ve ortalama 10 m'lik bir kalınlıkla, kabaca 4.3 milyon m^3 hacme karşılık gelmektedir. Yelpaze şeklindeki birikim alanı ana vadiye doğru Geç Kuvaterner yaşlı yan ve tümsekli morenlerin üzerinde depolanmış. Birikim alanındaki blokların boyutları 1 m'den az ve 15 m'den çok aralığında değişmekte ve bazen çapı 22 m'ye ulaşan ev büyüklüğünde devasa bloklara rastlanılmaktadır. NRA'ın birikim alanındaki bloklar 600–640 m yükseklik kaybı ve ~1550–1700 m arasında maksimum yatay mesafe kat ederek, ~20–21° arasında ilerleme açısına ulaşmıştır. ^{36}Cl yüzey yaşlandırma sonuçları NRA'ın birbirini takip eden Orta-Geç Holosen yaşlı iki yenilmeden oluştuğunu göstermektedir. Birinci ana ve büyük yenilme 4.59 ± 0.25 bin yıl önce meydana gelmiş ve ardından ikinci ve küçük olay 3.77 ± 0.20 bin yıl önce oluşmuştur. Kaya çığı birikim alanıyla kaplı olan yan morenin yaşı ise yaklaşık 12.30 ± 1.20 bin yıla denk gelmektedir. Kaya çığları için önkoşulları oluşturan faktörler, hazırlık rolü olan faktörler ve en son tetikleyen faktörleri incelenmek ve belirlemek oldukça önemlidir. Bu çalışmada ana kaya çığının koptuğu buzul sirkindeki çatlaklı ve tabakalı kireçtaşları, NRA'ın yenilmesi için gerekli önkoşulları sağladığı düşünülmektedir. Geyikdağı'ında buzulların erimesi ile NRA'ın oluşumu arasında uzun bir gecikmenin yaşanması (~7.7 ve 8.5 bin yıl), buzul yükünün ortadan kalkmasının kaya çığı için başlıca hazırlık faktörü olduğunu göstermektedir. Ayrıca, buzul erozyonu ve kireçtaşının karstlaşmasıda bu kaya çığı için diğer hazırlık faktörleri olabilir. Orta Toroslar'daki düşük sismik aktivite ve kaya çığının Orta-Geç Holosen iklim geçişleriyle eşzamanlılığı, iklim faktörlerinin NRA oluşmasını tetiklemiş olabileceğini göstermektedir. Daha yaşlı olan ana yenilme, Toroslar'daki kuvvetli ani yağışlarla ilişkilendirilen Holosen ortasındaki sıcak kuraklık dönemiyle örtüşürken, daha genç olan olayın yaşı, Holosen sonundaki uzun ve nemli dönemle ilişkili olabilir. Dolayısıyla, NRA'ın ana olayı yüksek sıcaklık, yoğun ve ani yağışların etkisiyle tetiklenmiş olabilecekken, ikinci olay daha uzun süreli sağanak yağışların etkisiyle tetiklenmiş olabilir. NRA'ın bu iki olayı, aynı zamanda Alpler'de 5-3 bin yıl öncesine tarihlendirilmiş kaya yenilmeleriyle de eş zamanlıdır.

Genel olarak bu tez çalışmasında, Akdeniz'in kuzeydoğusunda karbonatlı kayaçların uzun süreli denüdasyon hızları ve ani aşınması incelenmiştir. Yapılan jeolojik ve kronolojik analizler, bu bölgedeki erozyon süreçlerinde iklimin en etkin faktör olduğunu göstermektedir. Çözünme denüdasyonu (kimyasal ayrışma), karbonatların uzun süreli aşınma hızının baskın mekanizması iken, fiziksel mekanizma episodik ve hızlı kütle hareketlerinden sorumludur. İleride yapılacak çalışmalar, denüdasyonun türünün bölgesel farklılıklarına, fiziksel ve kimyasal ayrışmanın derecesine odaklanabilir. Dahası, gelecekteki araştırmalar burada olduğu gibi noktasal ölçekli çalışmalardan, yamaç aşınmasına ve havza genelindeki denüdasyon hızlarını araştırmaya odaklanabilir. Ayrıca Orta Toroslarda buzullaşma geçirmiş diğer bölgelerde meydana gelen paraglasyal kaya yenilmelerinin tarihlendirilmesi de yapılarak, bu çalışma ile karşılaştırılabilir ve eski kaya çığlarının mekânsal ve zamansal dağılımı ve bunlara etki eden faktörler incelenebilir.

1. INTRODUCTION

Knowledge of erosional processes such as long-term denudation rates or episodic erosion (e.g., rapid mass movements) are essential for understanding landscape development. Although the southern margin of the Central Anatolian Plateau has been the focus of several studies on reconstructing uplift rates (e.g., Cosentino et al., 2012; Schildgen et al., 2012; Öğretmen et al., 2018), the interactions between tectonics, climate and erosional processes are poorly understood in this region. Particularly, there is a lack of research regarding denudation of carbonate terrains which widely cover the plateau margin. Moreover, in spite of extensive surface exposure dating of glacial deposits in the Central Taurides (Sarıkaya and Çiner, 2017), other paraglacial landforms such as rock avalanches are less considered.

This thesis aims to quantify the long-term denudation rate of carbonate outcrops and the age of a rapid mass movement in the south of the Central Anatolian Plateau and investigate their controlling factors. In more detail, it aims to determine the denudation rate of carbonate rocks across an actively uplifting plateau margin with a sharply varying climate gradient and to explore the influence of different factors on the spatial distribution of denudation rates. Moreover, it tries to provide a better understanding of the causes and triggers of rock slope failures by combining the ^{36}Cl age results with deglaciation and paleoclimate data. To do this, it uses the inventory of in-situ produced cosmogenic nuclides on long-time exposed surfaces to determine the long-term denudation rates and to measure the same nuclide on recently exposed rock surfaces to calculate the exposure ages of a paleo-rock avalanche. These data are used to explore the controlling factors of the long-term denudation rates and to discover the causes and triggers of the studied rock slope failure in relation to climate and tectonics.

This first chapter will provide an introduction to the topic by providing a literature review on the denudation rate of carbonates constrained using ^{36}Cl cosmogenic nuclide, followed by background about the dating and recurrence interval of large mass movements using cosmogenic nuclides. Then, the research gap, objectives, and research questions will be addressed.

1.1 Literature Review and Research Gap

1.1.1 ^{36}Cl-derived denudation rate of carbonates

Denudation is defined as the total mass loss due to chemical weathering and physical erosion (Granger & Riebe, 2014), and usually reported in mm/ka. To date, researchers have applied various methods, such as rock tablets (e.g., Plan, 2005; Krklec et al., 2016; Krklec et al., 2021), micro erosion meters (e.g., Cucchi et al., 2006; Furlani et al., 2009), solute load analyses (e.g., Lauritzen, 1990; Plan, 2005) or calcite dissolution experiments in the laboratory (e.g., Levenson et al., 2017), to quantify the short-term denudation rate of carbonates. However, these approaches measure mostly chemical dissolution rates under controlled conditions rather than total denudation. Moreover, since these methods provide information on short-term denudation rates, e.g., annual or decadal, they do not capture the influence of climate or tectonic forcings over geological times. Researchers traditionally used limestone pedestals to measure the long-term denudation rate of carbonates (e.g., Wilson et al., 2012), in which the pedestal height represents the amount of surface lowering. Thus, long-term denudation rates can be calculated by dividing pedestal height by the settlement age of the boulder. Because the pedestal formation occurs mostly on flat surfaces, where glacial erratic boulders or a tsunami-carried boulder form a caprock for the underlying carbonate rocks, this cannot apply to all carbonate landforms. Another method uses ^{36}Cl cosmogenic nuclide, which provides an ideal tool for measuring the long-term denudation rate of carbonates on different geomorphological settings (e.g., hilltops, flat plateau surfaces, hillslopes) and it could be applied over Quaternary time scale (e.g., Stone et al., 1994; Ryb et al., 2014a, 2014b).

Although research on determining the denudation rate of carbonates using ^{36}Cl cosmogenic nuclide began about three decades ago by pioneering studies of Dockhorn et al. (1991) and Stone et al. (1994), further research gained momentum in the last decade after significant improvements in the calibration of K and Ca spallation pathways for ^{36}Cl production (Marrero et al., 2016b). Previous studies employed ^{36}Cl cosmogenic nuclide to quantify the denudation rate of carbonates both on the catchment wide (e.g., Ryb et al., 2014b; Thomas et al., 2017; Ott et al., 2019, 2023) and outcrop scales (e.g., Stone et al., 1994; Ryb et al., 2014a; Thomas et al., 2018; Marrero et al., 2018). These studies determined the carbonate denudation rates and the

control of different variables on the evolution of the carbonate landscape. The researchers found a relationship between denudation rate of carbonate rocks with many parameters, such as precipitation (Ryb et al., 2014a, 2014b; Yang et al., 2020; Ott et al., 2023), temperature (Matsushi et al., 2010a; Xu et al., 2013), elevation (Avni et al., 2019), topographic gradients (Ryb et al., 2014a; Thomas et al., 2017), hilltop curvature (Godard et al., 2016), bedrock properties (Ben-Asher et al., 2021), soil cover and CO_2 availability (Avni et al., 2019), and the presence of lichens (Krklec et al., 2022). Some studies highlighted the rebost control of climate over denudation, which leads to similar patterns between carbonate denudation and climate zones (Stone et al., 1994; Ryb et al., 2014a; Thomas et al., 2017). This pattern indicates that low denudation rates occur in arid climates and moderate to high denudations in moist temperate environments. Some studies attributed climate control to the role of precipitation on carbonate dissolution (e.g., Ryb et al., 2014a, 2014b), whereas others emphasized the role of temperature (Matsushi et al., 2010a; Xu et al., 2013). Ryb et al. (2014b) showed that carbonate dissolution is the main controlling factor on annual, decadal, and 10^4-year time scales, while mechanical erosion has a minor role. In the carbonate terrains of central Israel, ^{36}Cl-derived denudation rates showed higher values in the Mediterranean zone and lower rates in the hyper-arid zone, suggesting a strong precipitation control (Ryb et al., 2014a). In the karst terrains of Japan, chemical dissolution was the dominant style of carbonate denudation in subtropical regions, while physical erosion prevailed in the subarctic areas (Matsushi et al., 2010a). In Antarctica, carbonate rocks showed trivial denudation rates, suggesting the inefficiency of chemical weathering in cold, arid regions (Marrero et al., 2018).

Topographic variables also affected the denudation of carbonate rocks. In the Luberon mountain range in France, there is a significant difference between the denudation of the summit surface and the flanks (Thomas et al., 2017). While carbonates on the summit denude through chemical dissolution, on the flanks, they denude at much higher rates, suggesting the influence of slope-dependent processes, which eventually will lead to the narrowing of the summit by regression of flanks through erosion (Thomas et al., 2017). Previous studies also indicated the relationship between carbonate denudation and hilltop curvature. They found that carbonate denudation rates rise with increasing hilltop convexity from 30 mm/ka up to 70 mm/ka (Godard et al., 2016), but from this point on, it remains insensitive to the increase in hilltop

convexity, implying a transition from the transport-limited hillslope evolution to the weathering-limited evolution. Ben-Asher et al. (2021) demonstrated that mean annual rainfall and bedrock properties control the denudation of carbonate hilltops. Thus, soft carbonate hilltops (chalk) show higher denudation rates than resistant carbonates (dolo-limestone) in the same rainfall regime. Avni et al. (2019) found that carbonate denudation rates at intermediate elevations (1000-1600 m) are higher than the subalpine regions (with 1700-2200 m elevation). Based on this result, they pointed out that the ideal condition for the dissolution of carbonates occurs below the tree line where there is a thick soil cover and high pCO_2 (Avni et al., 2019).

In addition, some studies investigated the influence of mineralogical composition (Levenson et al., 2017), lithological effect (Krklec et al., 2022), rock type and density (Xu et al., 2013), and rock mechanical strength and clay content (Ryb et al., 2014a), suggesting that these variables have a weak control on carbonate denudation.

These findings indicate that the information gap still exists, and the magnitude of carbonate denudation and its relationship with different environmental variables across various climatic and tectonic settings remains unclear. Most previous studies have focused on the effect of climate on carbonate denudation in regions with low tectonic activity. Therefore, there is a lack of knowledge about the influence of the interplay between tectonic uplift and climate on carbonate denudation in actively uplifting settings such as orogenic plateau margins. Moreover, although the uplift rates have been documented relatively well in the south of the Central Anatolian Plateau, the influence of tectonic and climate on the evolution of carbonate terrains that cover the plateau margin has not been explored yet.

1.1.2 ^{36}Cl surface exposure dating of prehistorical rock slope fauliers

Rock slope failures (RSFs) such as rock avalanches, rock slides, or rock falls are the main erosional processes that modify the landscape. These processes are considered as rapid and episodic erosion of the landscape. In mountainous regions, glacially over steepened rock walls are highly prone to failure immediately after deglaciation or several millennia later (Ballantyne et al., 2014). Paraglacial RSFs are non-glacial landforms conditioned by glaciation and deglaciation (Ballantyne, 2002; McColl, 2012). By determining the timing of these high magnitude-low frequency events, we can better understand their cause and triggers concerning tectonic and climatic events

(Ivy-Ochs and Schaller, 2009). Moreover, dating RSFs provide valuable information in relation to their role with other geomorphic processes (Cockburn and Summerfield, 2004).

The cosmogenic nuclides such as ^{36}Cl and ^{10}Be provide the best tool for dating bedrock and boulders of RSFs. Before the devolopment of the terrestrial cosmogenic nuclide (TCN) dating method, most researchers assumed that the RSF on the glaciated mountains occurs immediately after deglaciation (Heim, 1932). However, TCN dating of RSF boulders in many regions revealed they mostly occurred much later, i.e., during the Holocene. Although prehistoric RSFs are studied widely in some regions of the world, such as the Alps (Prager et al., 2008; Nagelisen et al., 2015; Grämiger et al., 2016; S. Ivy-Ochs et al., 2017; Gallach et al., 2018; Singeisen et al., 2020), there is still limited studies on the dating and causes of these landforms in some other regions such as the glaciated mountains of Türkiye.

Some studies that dated post-glacial RSFs using cosmogenic nuclides attributed the failure cause to climatic conditions (precipitation or temperature) (e.g., Prager et al., 2008; Ivy-Ochs et al., 2009). The boulders of the Flims landslide in Switzerland showed a mean age of 8900 ± 700 years, consisting with the timing of two nearby rockslides in the region, which all correlated with the transition to warmer and wetter climate during the early Holocene (Ivy-Ochs et al., 2009). A compilation of more than 480 landslides in Austria showed temporal distribution of the events in the early Holocene (10500-9400 cal BP) and at about 4200-3000 cal BP (Prager et al., 2008). Most of these landslides occurred at least 1000 years after glacial retreat, suggesting that deglaciation did not directly trigger these RSFs. Instead, a climatic phase with high water supply that increased pore pressures in the rock masses was attributed as the trigger of these RSFs (Prager et al., 2008). In the Tatra Mountains, Western Carpathians, ^{10}Be surface exposure dating of several RSFs showed that smaller events occurred immediately after ice retreat, while the larger ones with complex slope structures showed a significant time lag after deglaciation (Pánek et al., 2016). The timing of the latter group correlated with warmer and humid periods in the Late Glacial/Early Holocene (Pánek et al., 2016).

Furthermore, other studies found a relationship between the timing of the RSF and nearby seismic events. TCN dating of post-glacial RSFs using ^{10}Be in Scotland and NW Ireland showed that most RSFs occurred within ~5400 years after deglaciation.

This time lag suggested that rock mass strength reduction after deglaciation takes some time, and the final failure occurs spontaneously or through an external cause such as seismic activity (Ballantyne et al., 2014). The ^{36}Cl exposure dating of two rock avalanches in the Bernese Alps revealed an age of 9.8 ± 0.5 ka for both events. The significant lag time between these events and deglaciation showed that deglaciation could not trigger them, while instead, their coincidence with paleoseismic events suggested a seismic trigger (Grämiger et al., 2016). In addition, deposited boulders of two rock avalanches have been dated in the Granger Alps, Switzerland, revealing exposure ages of 12.6 ± 1.0 ka and 6.1 ± 0.8 ka. The coincidence of the first event with turbidite deposits in neighboring Lake Zurich suggested a high possibility of a seismic trigger (Nagelisen et al., 2015). In the El Capitan in Yosemite Valley, California, the ^{10}Be exposure age of rock avalanche boulders showed a mean age of 3.6 ± 0.2 ka (Stock and Uhrhammer, 2010). 13 ka time lag between this event and deglaciation suggested that glacial debutressing did not trigger the failure. The coincidence of this rock avalanche and the fault rupture of a nearby fault implied that an earthquake caused the failure (Stock and Uhrhammer, 2010).

Although glacial landforms, particularly moraines, have been extensively studied and dated using cosmogenic nuclides in the Taurides Mountains, Türkiye, other glacial landforms, especially RSFs, have not been explored enough. The only study on the timing and geomorphology of a prehistoric rock avalanche belongs to the Akdağ rock avalanche in SW Türkiye (Bayrakdar et al., 2020b). Oliva et al. (2018) stated that deglaciation around 21 ka in Anatolia was associated with an increase in RSFs. However, there is a lack of knowledge about geomorphological mapping and TCN dating of these landforms in Türkiye.

1.2 Research Objectives

In general, this thesis uses cosmogenic ^{36}Cl to unravel the rate and age of surface processes in the south of the Central Anatolian plateau.

Firstly, this research (1) constrains the magnitude of ^{36}Cl-derived denudation rate of carbonate rocks, (2) correlates the denudation rates with measured physical properties of the sampled rocks, (3) and a compilation of environmental parameters (4) to investigate its controlling factors in the south of the Central Anatolian Plateau. This research will cover the information gap regarding the long-term denudation rate of

carbonate outcrops and its controls across an actively uplifting plateau margin. Therefore, the primary aim of this project is to quantify the long-term denudation rates of carbonate rocks and discover their spatial variation as a function of climate, topography, tectonics, and physical properties of rock. The research questions are summarized as follows:

- How does the magnitude of the long-term denudation rates vary across the carbonate landscape?
- Does the distribution of denudation rates show any spatial pattern?
- What parameters control the magnitude and spatial variation of denudation rates?

Secondly, this research uses fieldwork, ^{36}Cl cosmogenic nuclide dating techniques, and geomorphological mapping to reconstruct the timing and morphology of a paraglacial rock avalanche in the Central Taurides. The results cover the information gap concerning the spatial and temporal distribution of paraglacial rock slope failures in the glaciated mountain ranges of the Central Taurides, Türkiye. The reseach questions about studied rock slope failure are summerised as follows:

- What is the cosmogenic surface exposure age of the rock avalanche?
- Is it the result of a single event or multiple events?
- What are the possible preparatory and triggering factors contributing to the slope failure?

1.3 Thesis Outline

This thesis includes seven chapters investigating erosional processes in carbonate rocks as long-term denudation rates or as spontaneous rock slope failure. The thesis outline is as follows:

- Chapter one presents an introduction, including a brief literature review, research gap, objectives, and questions.
- Chapter two provides a literature review on the ^{36}Cl-derived denudation rate of carbonate rocks and the evaluated parameters as controlling factors. In addition, it gives background information on prehistoric rock slope failures dated using

cosmogenic nuclides and their cause and triggers regarding seismic and climatic events.

- Chapter three provides an overview of the study area, including the geology, geomorphology, and climate. Moreover, it gives information on the geology and paleoclimate of the Geyikdağ Mountain, where the studied rock avalanche is located.
- Chapter four covers methodology, which explains the application of ^{36}Cl cosmogenic nuclides in quantifying the rate and age of the surface processes. It also includes sampling techniques, laboratory procedures for chemical preparation of cosmogenic samples, and denudation rate and surface exposure age calculations. This chapter covers the measurement of physical properties for denudation samples and a compilation of climatic and topographic parameters. Moreover, it includes geomorphological mapping and morphometric analysis of the rock avalanche.
- Chapter five presents the results of ^{36}Cl-derived denudation rates and the correlation results for evaluated parameters. This chapter also includes the discussion and interpretation of the obtained denudation rates as a function of climate, tectonics, and physical properties of carbonate rocks. Most of the data presented in this chapter have been published and taken from Hashemi et al. (2023).
- Chapter six addresses the result of the ^{36}Cl surface exposure age of the rock avalanche and discusses the possible preconditioning, preparatory, and triggering factors. Most of the data presented in this chapter have been published and taken from Hashemi et al. (2022).
- Chapter seven presents the main conclusions of the thesis and suggestions for possible future research.

2. LITERATURE REVIEW

2.1 Worldwide ^{36}Cl-derived Denudation Rates and Controling Factors

Previous studies not only quantified the long-term denudation rate of carbonates using ^{36}Cl cosmogenic nuclide but also investigated the influence of different environmental factors on their magnitude and dominant style of denudation. The first study that utilized ^{36}Cl cosmogenic nuclide to determine denudation rates in carbonate rocks goes back to three decades ago. Stone et al. (1994) sampled flat-lying limestone outcrops in different regions in and around Australia. Their study showed that limestone denudation rate ranges from 5 mm/ka in the arid regions to 200 mm/ka in the equatorial high-elevation areas of New Guinea, showing a high similarity to climate zones. Matsushi et al. (2010a) reported that the ^{36}Cl-derived denudation rate of carbonates ranges between 20-60 mm/ka in karst regions of Japan under subtropical to subarctic climates. They found that chemical weathering is the dominant style of denudation in subtropical regions, while physical weathering prevails in subarctic areas, through freeze-thaw alteration of rock surfaces. The long-term denudation rate of limestone on side slopes of solution dolines in the Akiyoshi karst, Japan (Matsushi et al., 2010b) showed a range of 63 ± 7 to 256 ± 26 g m^{-2} yr^{-1}, which strongly correlated with the size of the topographic contributing area, implying that the denudation of the carbonate terrain was controlled primarily by shallow groundwater runoff recharged from the upstream. The long-term denudation rate of carbonate rocks ranged between 20 and 50 mm/ka in the Guizhou Karst region, China, in which the denudation rates correlated negatively with mean temperature, implying the control of climate on denudation and the dominance of chemical weathering (Xu et al., 2013). Ryb et al. (2014a) quantified the long-term denudation rate of carbonate rocks in the Arugot watershed in central Israel. They found that the denudation rate of flat-lying carbonate outcrops ranges between 20 mm/ka in the Mediterranean zone and 1-3 mm/ka in the hyper-arid area. These denudation rates strongly correlated with precipitation, representing the governance of chemical weathering. On the contrary, the hillslope denudation rates showed a good agreement with slope gradient, indicating the role of mechanical erosion on the overall denudation mechanism. They demonstrated that the transition

from the chemically-dominated denudation to mechanically-dominated occurs over a mean annual precipitation of 100-200 mm. Investigation of denudation rates in a tectonically stable carbonate terrain in the Soreq drainage, Judea Hills, Israel, showed an average long-term denudation rate of 21 ± 7 mm/ka for bedrock outcrops (Ryb et al., 2014b). The obtained denudation rates correlated positively with modern mean annual precipitation (MAP) values, while they decoupled from elevation, rock mechanical strength, and hillslope gradient. Moreover, they demonstrated a complex relationship with the Mg content and a weak correlation with clay content of the rock. Godard et al. (2016) explored denudation rates across a carbonate range in South-Eastern France and investigated their relationship with hilltop convexity. They found that the denudation of flat-lying summit plateau surface starts from 30 mm/ka and increases to 70 mm/ka with increasing hilltop convexity. They observed that beyond this point, denudation rates are insensitive to the hilltop convexity, indicating the transition of the denudation regime from transport-limited to weathering-limited. To evaluate the role of mineral composition on the variability of denudation rates, Levenson et al. (2017) compared the ^{36}Cl-derived denudation rates with chemical weathering rates of the same samples measured through laboratory experiments. Although the results showed that the experimental chemical weathering rates decreased as the ratio of dolomite to calcite increased, no correlation was found between ^{36}Cl denudation rates and mineral composition, suggesting that the kinetics of dissolution did not control the diversity of long-term denudation rates in the field (Levenson et al., 2017). Thomas et al. (2017) considered the impact of morphological setting on the denudation of carbonates across a single mountain range under the Mediterranean climate in SE France. They found that the long-term denudation rates of carbonate outcrops from flat-summits averaged around 30 mm/ka, while the basin-wide denudation rates across both flanks ranged from 100 to 200 mm/ka. They pointed out that this denudation pattern suggests that while denudation rates on the flat summit are controlled by chemical dissolution, denudation on the flanks is primarily controlled by slope-dependent processes. Moreover, investigating the denudation pattern across some carbonate mountain ranges in SE France revealed a denudation range of 30-60 mm/ka, with no direct relationship with mean annual precipitation or temperature (Thomas et al., 2018). In the cold and arid Antarctica, carbonate rocks reflected low denudation rates (<1 mm/ka), which is lower than the obtained rates in other arid regions worldwide (Marrero et al., 2018). Avni et al. (2019) explored the denudation

patterns on a homogeneous limestone lithology across Mount Hermon, Israel, under Mediterranean to subalpine climatic conditions. They found that hilltops in the subalpine region denude more slowly (average rate: 19 mm/ka) than the intermediate altitudes (average rate: 42 mm/ka). They interpreted that the ideal condition for chemical weathering of carbonates occurs at intermediate elevations, below the tree line, where the soil cover is thick and CO_2 pressure is high. Yang et al. (2020) compiled global ^{36}Cl-derived bedrock denudation rates from different climatic gradients and plotted them versus modern precipitation. They showed that while the denudation rates increase with precipitation in arid regions (MAP < 700 mm), they remain constant and limited within 34.1 ± 11.7 mm/ka in humid climates (MAP > 700 mm), under the influence of dissolution kinetics of carbonates. The relationship between hilltop convexity and carbonate denudation has been examined in the Eastern Mediterranean across a significant rainfall gradient (Ben-Asher et al., 2021). This investigation demonstrated that the denudation rate of carbonates spans from 5 to 210 mm/ka, showing an increasing trend with mean annual rainfall. Furthermore, soft carbonates (chalk) experienced more rapid denudation rates than resistant carbonates (dolo-limestone). In the karst terrains of the Dalmatian Plain (Croatia), two different carbonate rocks with diverse weathering patterns show no evidence of lithological control on the topography of the carbonate landscape (Krklec et al., 2022). Exploring the denudation rates of these two lithologies using ^{36}Cl cosmogenic nuclide indicated long-term denudation rates of 14.7-22.8 mm/ka. Krklec et al. (2022) interpreted that the variable denudation rates of two units in the vicinity under the same climatic and morphological conditions are related to local factors such as the presence of lichens and the formation of pedogenic carbonates. Finally, Ott et al. (2023) compiled all the bedrock and basin-averaged denudation rates in carbonate terrains and compared them with the weathering rates. Their findings showed that the bedrock denudation rates are similar to weathering rates ranging between 20 and 40 mm/ka, suggesting the dominant role of chemical weathering in the denudation of carbonate bedrock. Catchments showed 2.7 times higher denudation rates than weathering, representing the significant contribution of mechanical erosion. Moreover, this study highlighted the importance of interactions between climate and tectonics on denudation partitioning in carbonate terrains. Carbonates make the low flat topography in humid regions with slow uplift rates, suggesting the importance of chemical weathering as the dominant style of denudation, while they form steep mountains in arid climates

with rapid uplift rates representing the privilege of mechanical erosion (Ott et al., 2023). All these findings provided valuable information on carbonate long-term denudation rates and showed that our knowledge about carbonate denudation and its behavior in different tectonic and climatic settings is still limited.

2.2 Surface Exposure Dating of Prehistoric Rock Slope Failures (RSF)

Surface exposure dating has been used in many studies to evaluate the causes and triggers of failure in prehistoric rock slope failures (RSFs). Ballantyne et al., (1998) dated a landslide using ^{36}Cl cosmogenic nuclide on the Isle of Skye, Scotland. They obtained an average age of 6.5 ± 0.5 cal. Ka BP for the landslide, showing a long lag time (> 7 ka) between deglaciation and RSF occurrence. Therefore, they attributed the cause of failure to the progressive joint extension, although a seismic trigger was not ruled out. Prager et al. (2008) made the first comprehensive compilation of mass movements in the Eastern Alps (Austria) and dated them to evaluate their spatial and temporal distribution. Their results indicated that landslide activities cluster temporarily in two groups: one in the early Holocene at about 10500-9400 cal BP and the other at 4200-3000 cal BP. They found that most Holocene mass movements occurred some thousand years after the ice retreat through fracture propagation and increase of pore pressure. The synchronicity between some of the studied landslides and some large debris flows in the vicinity and with glacier advances in the Central Alps was interpreted as the role of a climate phase with intense water supply on failure. Dortch et al. (2009) examined and dated four landslides using ^{10}Be cosmogenic nuclide in the Himalaya and Trans-Himalaya of northern India, which resulted in an age range of 6.6 – 8.5 ka. The authors interpreted that since deglaciation occurred more than two thousand years ago, glacial debuttressing cannot be the triggering factor for the landslides. They concluded that increased pore water pressure, a seismic event, or a combination of both may triggered these landslides. Dating boulders of the Flims landslide, Switzerland, demonstrated a mean age of 8900 ± 700 years (Ivy-Ochs et al., 2009), which was similar to two other rockslides (Köfels: 9800 yr, Kandertal: 9600 yr) in the region. The timing of all three landslides was synchronous with the transition to warmer and wetter climatic conditions during the early Holocene (Ivy-Ochs et al., 2009). A statistical analysis of radiocarbon ages of 24 landslides in the Dolomites (eastern Alps, Italy) indicated four periods of enhanced landslide activity, which

coincide with cold and humid climate conditions (Borgatti and Soldati, 2010). The boulders of the El Capitan rock avalanche, which occurred in the glacially steepened cliffs of Yosemite Valley, California, have been mapped and dated by Stock and Uhrhammer (2010). Cosmogenic ^{10}Be surface exposure ages of the boulders yielded an average age of 3.6 ± 0.2 Ka. About 13 ka time lag between ice withdrawal and failure on one side and the coincidence with late Holocene rupture of two nearby faults on the other side suggested that a large earthquake and not the glacial debuttressing most probably triggered this rock avalanche (Stock and Uhrhammer, 2010). Ballantyne et al. (2014) dated 31 postglacial RSFs in Scotland and NW Ireland to find the temporal pattern of failure and its relationship with deglaciation, isostatic crustal uplift, and climate events. They found that the ages of RSFs range between 18.2 and 1.7 ka, with catastrophic events happening more frequently before 11.7 ka and low-frequency RSF activity continuing throughout the Holocene. They concluded that the timing of maximum RSF activity coincides with maximum rates of glacio-isostatic crustal uplift, implying that both are related to enhanced seismic activity. Two large post-glacial rock avalanches in the Glarner Alps, Switzerland, were mapped and dated using ^{36}Cl cosmogenic nuclides by Nagelisen et al. (2015). The first rock avalanche, with an estimated volume of 91 million m^3, showed an exposure age of 12.6 ± 1.0 ka, while the second one revealed a mid-Holocene age of 6.1 ± 0.8 ka. Since the first event temporarly correlated with turbidite deposits in Lake Zurich, a seismic trigger was suggested for its formation. Moreover, Grämiger et al. (2016) mapped, dated, and modeled two other rock avalanches in the Bernese Alps, Switzerland. They estimated a limestone debris volume of 4 million m^3 and 37 million m^3 for these rock avalanches with a similar surface exposure age of 9.8 ± 0.5 ka. They interpreted that the long lag time between rock avalanches and deglaciation on one hand and the coinciding of these events with another nearby rock avalanche and paleoseismic records from neighboring lakes suggest seismic triggering. Pánek et al. (2016) mapped and dated six post-glacial RSFs (rock avalanches or rockfalls) in the Tatra Mountains, Carpathians, using cosmogenic ^{10}Be, which resulted in an age range of 20.2 –10.1 ka. Their results showed that the smaller RSFs (mainly rockfalls), located in the steepest parts of the mountain, failed instantly after deglaciation, while the large and complex RSFs (mostly rock avalanches) in the low relief side of the mountain occurred several millennia after deglaciation. Pánek et al. (2016) attributed the cause of failure in delayed RSFs to warmer and more humid periods in the Lateglacial/early Holocene. Geomorphological

mapping and cosmogenic ^{36}Cl surface exposure dating showed that the Maroche di Dro rock avalanches in Italy consist of two events (Ivy-Ochs et al., 2017), while previously, without dating information, mapped as five events. The first event dated to 5300 ± 860 yr ago, coinciding with the shift to a wetter and colder climate in the middle to the late Holocene transition (Ivy-Ochs et al., 2017). The second event occurred 1080 ± 160 yr ago which a nearby historic earthquake was introduced as its trigger (Ivy-Ochs et al., 2017). Five rockfalls in Mont Blanc have been sampled for surface exposure dating with cosmogenic ^{10}Be (Gallach et al., 2018). The age results showed that most rockfalls occurred in the Holocene, except three in the Pleistocene. Comparing the results with climatic data indicated that rockfall ages clustered in two groups and coincided with the warmest periods of the Holocene: one in the Middle Holocene (8.2 – 4.2 ka) and the other one in the Roman Warm Period (about 2 ka) (Gallach et al., 2018). Köpfli et al. (2018) investigated the Oeschinensee rock avalanche, which dammed Lake Oeschinensee, in the Bernese Alps, Switzerland, by a combination of remote mapping, cosmogenic surface exposure dating, and runout numerical modeling methods. Their study revealed that the deposits that dammed the lake consist of one old rock avalanche and the Oeschinensee. Their runout modeling and ^{36}Cl surface exposure dating confirmed a single-event failure with a mean age of 2.3 ± 0.2 ka. This age corresponded with the timing of a historic seismic event, suggesting an earthquake as a trigger. The formation, geomorphology, and age of the Akdağ rock avalanche, SW Türkiye, have been explored using field mapping, morphometric analysis, and surface exposure dating with cosmogenic ^{36}Cl (Bayrakdar et al., 2020b). The mapping result showed that the Akdağ rock avalanche, one of the largest bedrock landslides in Türkiye, developed between carbonates and flysch layers. The age constraints indicated that the main event occurred at 8.3 ± 1.4 ka ago (2σ), followed by secondary failures with the latest one in 1.1 ± 0.2 ka (2σ). The cause of the primary collapse in the early Holocene was attributed to the increased water discharge in the springs along the carbonate-flysch zone (Bayrakdar et al., 2020b). The Bush Stream rock avalanche in the glaciated areas of New Zealand has been mapped and dated using cosmogenic ^{10}Be (McColl, 2012). The dated boulders revealed a pre-Holocene age (>16 ka) for the failure, making it the oldest reported rock avalanche in New Zealand and one of the oldest last-glaciation rock avalanches in the world. This study confirmed that rock avalanches in the Southern Alps have been produced soon after deglaciation (McColl, 2020). Investigation of an inventory of published ages for

49 prehistoric, moderate to large (>10^3 m^3) paraglacial RSFs in western Norway indicated that most of the failures occurred in the Late Pleistocene-Early Holocene transition (~ 13-9 ka), during 2 ka of deglaciation (Curry, 2021 and references therein). Following RSFs during the Holocene had smaller volumes, although their frequency increased at 8-7 ka and 5-4 ka (Curry, 2021). Most failures occurred at least 1000 years after deglaciation, indicating that glacial debuttressing and ice withdrawal preconditioned slope failure without directly triggering them. Previous studies suggested stress redistribution, subcritical fracture propagation, and seismic activity as possible triggers for the RSFs in western Norway (Curry, 2021 and references therein). Zerathe et al. (2022) constrained the chronological age of a large paleolandslide in the hyperarid Central Western Andes. ^{10}Be surface exposure ages showed that the landslide consisted of a single event with a mean age of 80 ± 4 ka. This timing coincided with a wet period in the Atacama Desert, suggesting a primary control of climate on RSF activity in this region (Zerathe et al., 2022). Dating several rock avalanches along the active faults with no surface ruptures has been used to infer the paleo-earthquake timing. Rodríguez-Rodríguez et al. (2023) focused on two rock avalanches in the Gantabrian Mountains, Spain, where previous research reported the activity of Quaternary faulting. ^{36}Cl surface exposure dating of 20 boulders showed that the youngest event occurred 8.5 ± 0.6 ka ago, was documented in the recent lobes of both rock avalanches, and indicates the timing of the latest large earthquake along the fault. The age of boulders in the middle and distal lobes demonstrates four more seismic instability between 22.0 and 10.9 ka (Rodríguez-Rodríguez et al., 2023).

Overall, in recent decades, surface exposure dating of RSFs improved our understanding of their timing and recurrence interval. Moreover, they helped to reconstruct the seismic and climatic phenomena that caused these catastrophic events. In Türkiye, the number of studies on the timing of prehistoric RSFs and their cause and triggers are limited. Therefore, this thesis investigates the chronological age, geomorphology, and preparatory and triggering factors of a paleo rock avalanche in the glaciated terrains of the Central Taurides.

3. STUDY AREA

The study area for quantifying the denudation rates of carbonate rocks is south of the Central Anatolian Plateau (CAP), from the Mediterranean coast to the plateau interior. Moreover, the timing and geomorphology of a paleo-rock avalanche were explored in the Geyikdağ Mountain in the Central Taurides. Therefore, in this chapter, first, the geology, geomorphology, and climate of the CAP will be explained, and later, the regional setting of the Geyikdağ Mountain will be described exclusively.

3.1 Study Area of ^{36}Cl-derived Denudation Rates of Carbonate Outcrops

3.1.1 Geology

The Central Anatolian Plateau (CAP) is part of the Alpine-Himalayan orogenic belt, resulting from the convergence between the African-Arabian and Eurasian plates (Şengör and Yazıcı, 2020). The study area for the denudation of carbonates extends across a latitudinal gradient from 36°N to 38.5°N and a longitudinal gradient from 30°E to 34.5°E in the south of the Central Anatolian Plateau (Figure 3.1a), including three geographic regions, from south to north: the Mediterranean coastal region, the southern margin of the CAP (Central Taurides), and the CAP interior.

The coastal area has been separated from the highlands of the CAP by a prominent escarpment with an elevation of ~1700-2000 meters above sea level (m asl). In the plateau margin, the Central Taurides makes a NW-SE to E-W trending mountain range, with the highest elevations reaching 3500 m asl (Figure 3.1b). Some research focused on determining the incision and uplift history of the plateau margin. An average incision rate of 0.52-0.67 mm/yr for the last 130 ka has been obtained for the southern margin of the plateau based on the surface exposure age of the fluvial terraces (Schildgen et al., 2012). Moreover, Öğretmen et al. (2018) constrained a rapid uplift rate of 3.2 m/ka for the southern margin of the CAP during the last 450 ka, according to biostratigraphic data and considering the modern elevation of middle Pleistocene marine deposits. The morphostratigraphical analysis and modeling of marine terraces revealed a rapid increase in uplift rates between 500 and 200 ka followed by a decrease

in the Late Pleistocene until the present (Racano et al., 2020). To the N-NE, the elevations decrease to ~1000 m asl in the CAP interior. The uplift history of the CAP interior is relatively unclear (Schildgen et al., 2014). However, unlike the southern margin, the plateau interior was exposed subaerially much earlier, by the Late Middle Eocene (~41 Ma), and has undergone little topographic changes since then, with uplift rates less than 0.05 km/Ma (Okay et al., 2020). Furthermore, dating fluvial terraces of the Kızılırmak River using cosmogenic burial dating yielded an average incision rate of ~0.051 mm/yr since 1.9 Ma, suggesting that the CAP interior has uplifted 5–10 times slower than its northern and southern margins (Çiner et al., 2015a).

The study area includes the Central Taurides and the Central Anatolia karst regions. The Karst area in the Central Taurides (Figure 3.1b) forms a large carbonate platform mainly composed of Mesozoic carbonates, particularly the Jurassic-Cretaceous neritic limestone and the Miocene platform carbonates (Nazik et al., 2019) (Figure 3.2a). The Jurassic-Cretaceous neritic limestone (the Cehennemdere Fm.) forms a massive, ~1500 m thick-bedded, continuous sequence of platform carbonates (Monod, 1977; Demirtaşlı et al., 1984). The Miocene platform carbonates mainly consist of ~1000 m medium-to-thick-bedded, fossiliferous neritic limestone of the Middle Miocene Mut Fm. (Gedik et al., 1979; Atabey et al., 2000). In the Central Taurides, the dissolution of massive carbonates resulted in extensive karst structures of all scales, from karren to solution dolines, paleovalleys, poljes, and groundwater flows and cave systems (e.g., Nazik et al., 2019; Şimşek et al., 2019). To the west, the Jurassic-Cretaceous neritic limestone forms a mountainous landscape consisting of flat-summit ranges with extensive development of solution dolines (Öztürk et al., 2018; Nazik et al., 2019). Particularly, egg-box-like topography (Ford and Williams, 2007), which resulted from the extensive development of polygonal solution dolines, can be seen in these mountains (Öztürk et al., 2018; Nazik et al., 2019). To the east, where the Miocene neritic limestone is dominant, the landscape is a typical plateau-karst. The two well-developed karstic plateaus are the Taşeli and the Ermenek (Figure 3.1b), which make the largest and highest karst terrains in the Central Taurides. In these plateaus, the drainage is generally subterranean, and dolines and paleovalleys cover the surface (Öztürk et al., 2018; Şener & Öztürk, 2019; Öztürk, 2020). Therefore, the absence of active drainage provides a suitable condition for doline formation in the karstic plateaus (Öztürk et al., 2018). Further north, in the Central Anatolia karst region,

particularly in the Konya Basin karst area, the solution dolines are replaced with collapse dolines which developed in the Middle Triassic-Jurassic marbles, Jurassic-Cretaceous carbonates, and the overlying Pliocene lacustrine limestones (Nazik and Poyraz, 2017). Moreover, in the Central Anatolia karst region, the Middle Triassic-Jurassic marbles with 250 m thickness developed the dome-shaped hills.

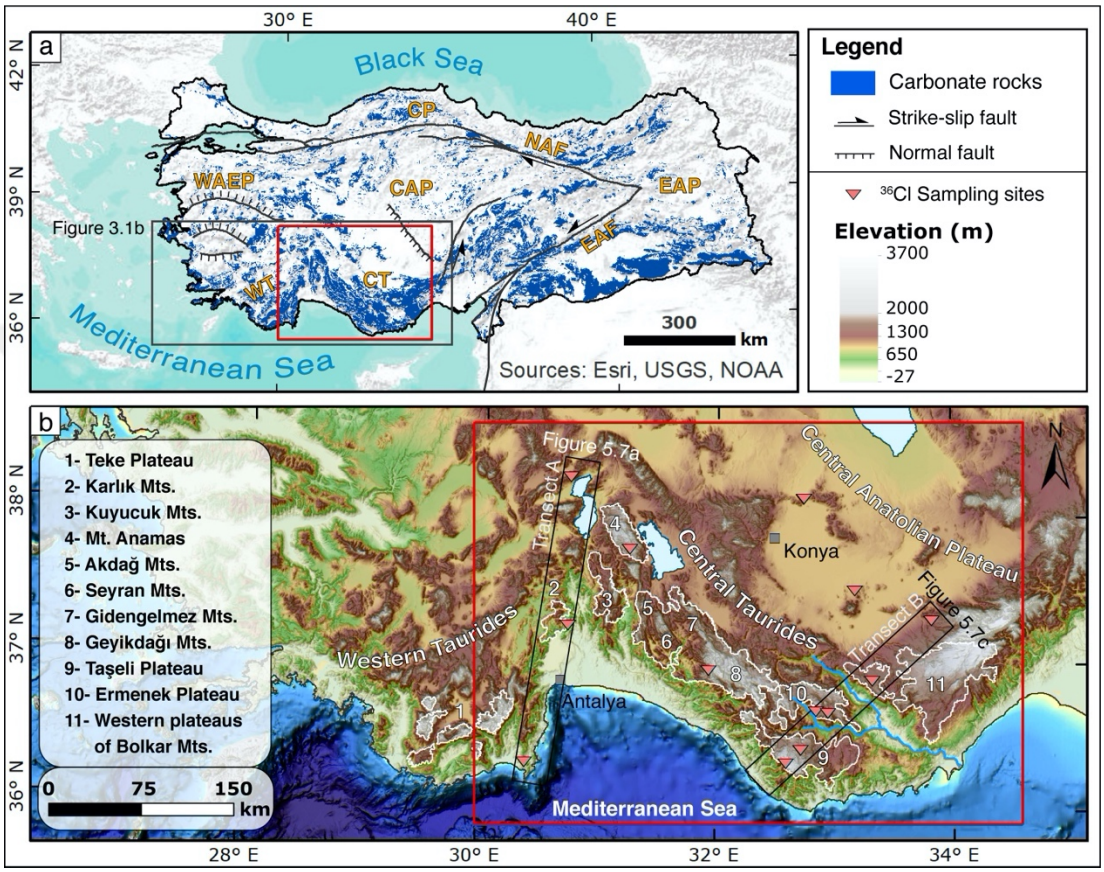

Figure 3. 1 : (a) The carbonate outcrops extracted from a 1/500,000 geological map of the General Directorate of Mineral Research and Exploration of Türkiye (MTA). The simplified tectonic setting of the Anatolia is shown on the map: CAP (Central Anatolian Plateau); CT (Central Taurides); WT (Western Taurides); CP (Central Pontides); EAP (Eastern Anatolian Plateau); WAEP (Western Anatolian Extensional Province); NAF (North Anatolian Fault); EAF (Eastern Anatolian Fault). (b) Shaded relief map of the study area. White lines delineate the karstic doline areas, simplified from the Öztürk et al. (2018). The red box in (a) and (b) shows the study area (Figures 3.2a-d, and 5.1a). Two black boxes outline the location of elevation swath profiles along Transects A and B (Figures 5.7a and 5.7c). This figure was taken from Hashemi et al. (2023).

3.1.2 Climate

The CAP is situated in the subtropical climate zone. It is mainly affected by polar and tropical air masses, and also by the Mediterranean Sea as the primary moisture source (Şensoy, 2004; Sariş et al., 2010). According to the Köppen-Geiger climate

classification (Beck et al., 2018), the study area consists of three different climate zones; (1) Mediterranean climate (Csa), “temperate, dry summer, hot summer”, in the coastal region, (2) continental climate (Dsb), “cold, dry summer, warm summer”, in the Central Taurides and (3) arid climate (BSk), “arid, steppe, cold”, in the CAP interior (Figure 3.2b). In the south of CAP, physiography and local topography exert major control over the precipitation regime and creates a dramatic precipitation gradient (e.g., Türkeş, 1996; Iyigun et al., 2013; Schemmel et al., 2013). The Central Taurides, with a high elevation and normal orientation to the moisture-bearing winds, acts as an orographic barrier blocking the moisture coming from the Mediterranean Sea (Sariş et al., 2010; Şahin et al., 2015). Therefore, on the windward side, the Mediterranean coastal region experiences high precipitation (Sariş et al., 2010) with mean annual precipitation (MAP) of 800–1200 mm for the period 1981–2010 (Şensoy et al., 2016), while on the plateau, the CAP interior, on the leeward side, maintains a low magnitude precipitation regime (Sariş et al., 2010) with a MAP of 300–500 mm for the same period (Şensoy et al., 2016) (Figure 3.2c). Cool, rainy winters and hot, dry summers characterize the Mediterranean coastal region with the mean annual temperature (MAT) of 16–20 °C (Şensoy, 2004) (Figure 3.2d). Cold, snowy winters and hot, dry summers prevail in the CAP interior, with MAT of 8–12 °C (Şensoy, 2004) (Figure 3.2d). Throughout the study area, precipitation shows strong seasonality, with the highest precipitation occurring in December and January. In the south of CAP, the strongest prevailing winds blow in summer, while the weakest blow in autumn (Şahin and Türkeş, 2013).

The present-day distribution of vegetation formations is affected by climatic and topographic gradients (Atalay et al., 2014a). The coastal region, from sea level to 1,200 m asl (Eu-Mediterranean belt), is dominated by *Pinus brutia* forests and maquis vegetation (Atalay et al., 2014a). In the high altitude regions of the Central Taurides with cold-subhumid conditions, Oro-Mediterranean coniferous forests are widespread (Atalay et al., 2014a, 2014b). However, in the eastern Central Taurides, the Taşeli and Ermenek plateaus form a largely treeless barren land with very sparse herbaceous vegetation. Finally, the arid CAP interior is characterized by steppes and anthropogenic steppe vegetation (Atalay et al., 2014b).

The paleoclimatic history of the south of CAP is not fully understood. The topographic rise of the southern margin of CAP and the formation of an orographic barrier highly

affected the climatic gradient across the region. Öğretmen et al. (2018) showed that the southern margin of CAP has gained most of its modern topography (~2 km) just recently, suggesting the lack of a significant orographic barrier along the plateau margin prior to 500 ka. This finding implies that the rain-shadow effect that characterizes the present-day climate of the CAP southern margin has persisted since 500 ka in the region.

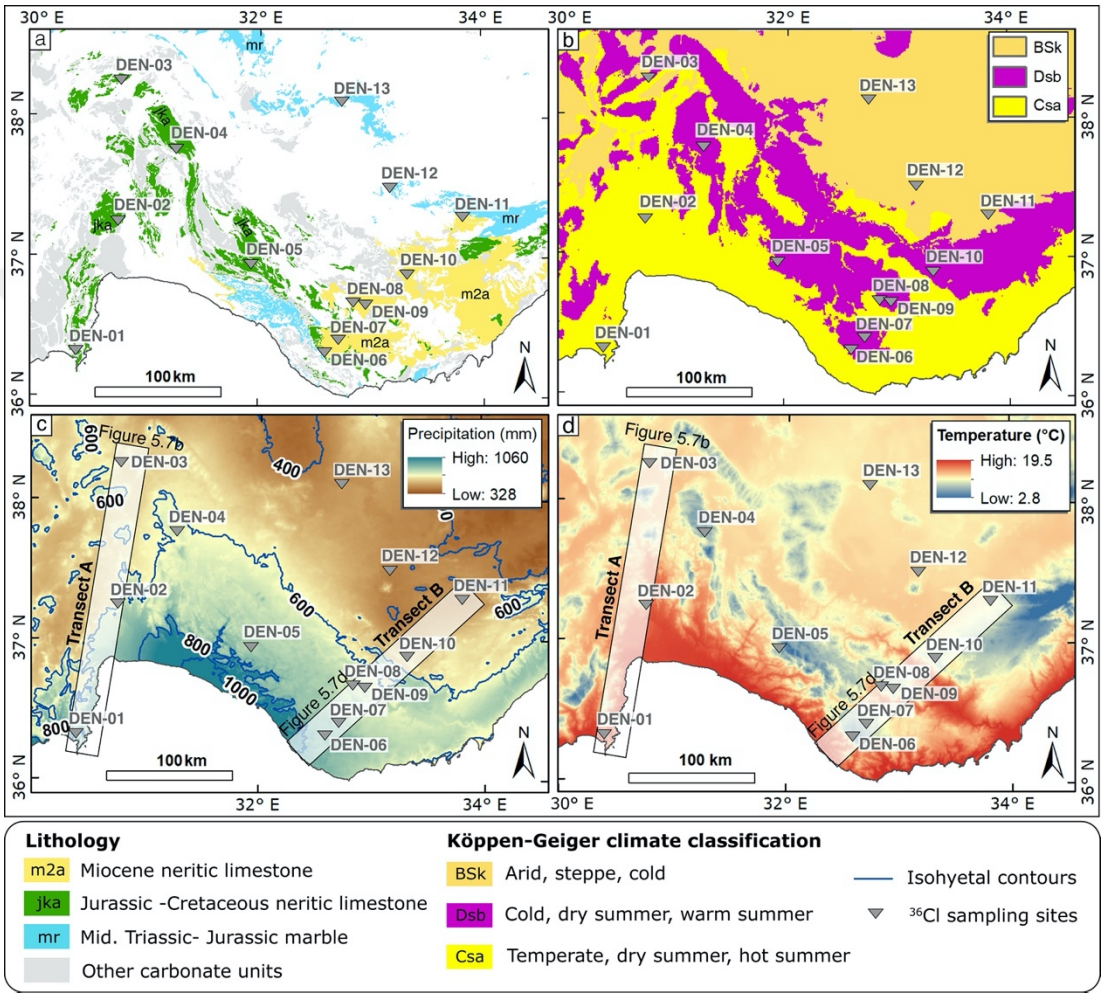

Figure 3. 2 : (a) The map shows three sampled lithostratigraphic units, including two carbonate units and one marble unit. The white area shows an undifferentiated lithology. (b) Climate zones in the study area were derived from the Köppen-Geiger climate classification (Beck et al., 2018). (c) Mean annual precipitation map was derived from WorldClim 2.1 (Fick and Hijmans, 2017). Dark blue solid lines (isohyetal contours) show the distribution of mean annual precipitation (mm). (d) Map of mean annual temperature was derived from WorldClim 2.1 (Fick and Hijmans, 2017). The white shaded boxes in (c) and (d) outline the location of swath profiles (Figures 5.7b and 5.7d). This figure was taken from Hashemi et al. (2023).

Late Quaternary glaciations were widespread in the high-altitudes (>3000 m asl). The oldest glacial activities were dated back to ~35 ka ago on the Western Taurides (Sarıkaya et al., 2014). Most extensive local glaciations were reported to be coincide

with the global Last Glacial Maximum (LGM) period (~21 ka ago). Late Glacial (between 16-11 ka) and possible Younger Dryas (11.7 ka ago) glacial advances were also reported in the Central Taurides. Late Holocene and Little Ice Age advances were much less extensive in the region. In the Central Taurides, the Late Pleistocene glaciation (e.g., Köse et al., 2022; Altınay et al., 2022) was restricted to the high peaks with the estimated last glacial equilibrium line altitude (ELA) of 2600–2700 m asl (Messerli, 1967; Sarıkaya and Çiner, 2017).

3.2 Study Area of the Namaras Rock Avalanche

The studied rock avalanche (hereafter the Namaras rock avalanche, NRA) is located in the Central Taurides, 50 km north of the Mediterranean coast of Türkiye (Figure 3.3a). Moreover, the NRA is on the northern flank of the Geyikdağ Mountain and the southern edge of a vast glaciated valley, the Namaras Valley (Figure 3.3b).

The Geyikdağ Mountain is an NW-SE oriented range with the highest elevations reaching 2877 m asl (Figure 3.3b). This mountain is one of the most extensively glaciated ranges during the late Quaternary in the Taurides (Çiner et al., 1999, 2015b, 2017; Sarıkaya et al., 2017; Bayrakdar et al., 2020a) and also in the Eastern Mediterranean (Çiner et al., 2015b). Several glacial valleys (Namaras, Susam, Çimi, Güneycik, and Çündüre valleys) with elevations ranging between 1600 and 2500 m asl surround the Geyikdağ Mountain. They all contain traces of paleo-glacial activity with well-developed hummocky, lateral, and terminal moraines (Çiner et al., 1999, 2015b, 2017; Sarıkaya et al., 2017) (Figure 3.3b). The west-facing Çimi Valley contains LGM moraines (20.6 ± 0.6 ka) and Late-glacial moraines (14.9 ± 1.4 ka to 13.7 ± 0.8 ka). In contrast, southernmost Güneycik Valley, with Late-glacial (14.5 ± 1.7 ka) and early-to mid-Holocene (9.6 ± 1.4 ka to 5.9 ± 0.5 ka) moraines, do not contain LGM moraines (Sarıkaya et al., 2017) (Figure 3.3b). The Geyikdağ was mostly ice-free towards the end of the Holocene, except for some periglacial features (i.e., rock glaciers) that developed on the north-facing slopes (Arpat and Özgül, 1972.; Çiner et al., 1999; Oliva et al., 2018). The modern ELA in the Central Taurides elevated to ~3400 m asl in the Geyikdağ Mountain, while the LGM ELA was at about 2500 m asl (Sarıkaya et al., 2017).

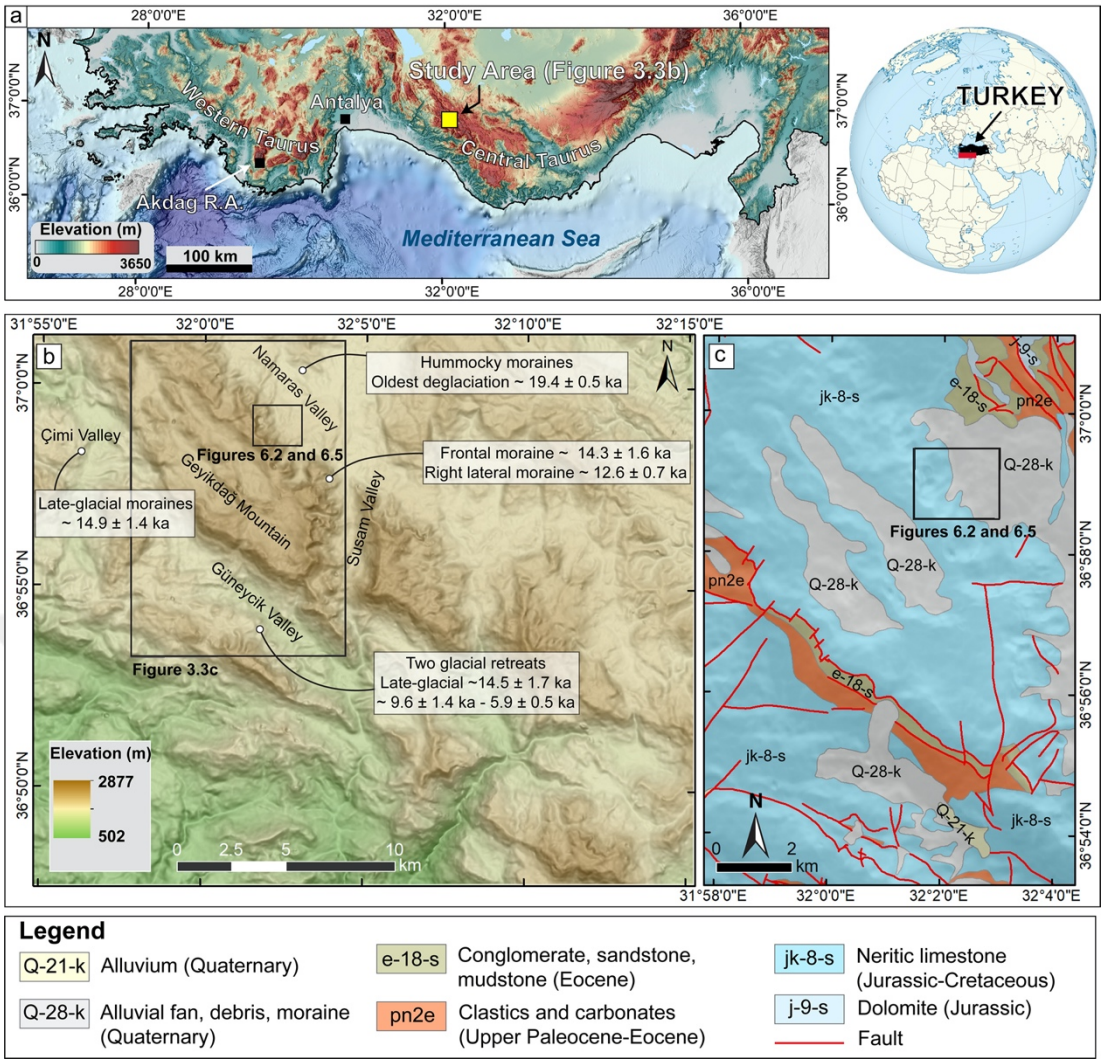

Figure 3. 3 : (a) The red box on the world map shows the extent of the map on the left. The overview map on the left is the Digital Elevation Model of Western and Central Taurides. The yellow box shows the location of the Namaras rock avalanche (Figure 3.3b). The location of Akdağ R.A. (rock avalanche) (Bayrakdar et al., 2020b) in the Western Taurides is marked on the map. (b) Digital Elevation Model (DEM) of the Geyikdağ Mountain. Moraine ages of the previously studied glacial valleys are from Çiner et al. (2015b) and Sarıkaya et al. (2017). The large box indicates the extent of geological map on the right. The black small box indicates the extent of NRA slope map (Figure 6.2) and the NRA geomorphological map (Figure 6.5). (c) The simplified geological map of NW of the Geyikdağ Mountain (data from the 1/25,000 geological map of Alanya, MTA). This figure was taken from Hashemi et al. (2022).

The lithology of the Geyikdağ Mountain is composed mainly of Jurassic-Cretaceous neritic limestones (Monod, 1977) (Figure 3.3c). The geology of the study area is complex and highly influenced by thrust tectonics, which caused multiple allochthonous units composed of several platform carbonate and ophiolite rock formations to align next to each other (Poisson, 1977; Şenel, 1996). The Geyikdağ Mountain shows evidence of extensive karstification. The glacio-karst morphology

has been developed (Sarıkaya et al., 2017), where karstic depressions acted as glacial cirques during past glaciations (Çiner et al., 2015b). Moreover, the polygonal doline karst was formed during the last glaciation in the Geyikdağ Mountain (Nazik et al., 2019; Öztürk et al., 2018; Şimşek et al., 2019).

Most of the paleoclimatic data for the Holocene around the study area is related to the lake records. Pollen and oxygen-isotope studies from the three nearest lakes to the Geyikdağ Mountain, respectively Lake Gölhisar (Eastwood et al., 2007), Lake Eski Acıgöl (Roberts et al., 2001, 2011), and Lake Van (Wick et al., 2003), show a trend from wet early Holocene to dry late Holocene. In the Köppen-Geiger climate classification (Beck et al., 2018), the Dsb type shows the climate of the Taurides, which stands for a semi-arid continental climate with cold, dry summer and warm summer. WorldClim v.2.1 (Fick and Hijmans, 2017) and weather stations in the study region give information on the current climate. The total annual precipitation in the nearest Akseki weather station (~28 km northwest of the study area) at 1065 m asl is 786 mm. The summer and winter average temperatures are 21 °C and 3 °C, respectively (Sarıkaya et al., 2017). The WorldClim v.2.1 (Fick and Hijmans, 2017) database indicates a Mean Annual Temperature (MAT) of ~7 °C and a Mean Annual Precipitation (MAP) of ~700 mm/yr for the study site.

4. MATERIALS AND METHODS

4.1 Terrestrial Cosmogenic Nuclide (TCN)

4.1.1 Cosmic ray origins and *in-situ* ^{36}Cl production rates

When the galactic cosmic radiation (also called primary cosmic ray) composed of high energy nucleons, mainly protons, reach the upper atmosphere, it interacts with nuclei of atoms in the atmosphere, producing a cascade of particles dominated by neutrons, which is called "secondary radiation" (Gosse and Phillips, 2001). The secondary cosmic ray goes down through the atmosphere and the upper few meters of the Earth's surface, interacts with target nuclides in the minerals, and produces cosmogenic nuclides (Gosse and Philips, 2001). The number of cosmogenic nuclides constructed from a target element in a specific mineral over time represents the production rate (Gosse and Phillips, 2001; Dunai, 2010). The pathways for the production of cosmogenic nuclides are spallation reactions, epithermal and thermal neutron capture, negative muon capture and stopping of fast muons (Gosse and Phillips, 2001, and references therein).

The primary cosmic rays are affected by the geomagnetic field of the Earth (Gosse and Phillips, 2001). In the geomagnetic equator, just cosmic rays that have enough energies can pass and reach to the Earth surface, while, in the poles, since cosmic ray trejactories are parallel to the geomagnetic field lines, they can easily reach to the ground. Thus, at higher latitudes the production rates are higher. Moreover, when the secondary cosmic ray travels toward the Earth's surface, the abundance of cosmogenic nuclides decreases with increasing atmospheric depth (Dunai, 2010). As a result, at lower altitudes the production rates are lower. Therefore, the changes in the energy spectra of the primary and secondary cosmic rays cause the production rate variations with latitude and altitude. Scaling factors project the cosmic ray flux variability relative to the altitude and latitude of the sampling site (Dunai, 2010). Several scaling factors have been presented to scale the production rate of a cosmogenic nuclide from

Sea-Level-High-Latitude (SLHL) to the sampling location (e.g., Lal, 1991; Stone, 2000; Lifton et al., 2014).

^{36}Cl is the only cosmogenic nuclide which is applicable for dating of carbonate rocks. ^{36}Cl is produced mainly by spallation reactions from K and Ca, and to a limited degree, from Ti and Fe (e.g., Phillips et al., 2001). Moreover, capturing thermal neutrons by ^{35}Cl and ^{39}K can produce significant amounts of ^{36}Cl via ^{35}Cl(n, γ)^{36}Cl and ^{39}K(n, α)^{36}Cl reactions, respectively (Phillips et al., 2001). Negative muons account for 6% and 11% of ^{36}Cl production from K and Ca at SLHL, respectively (e.g., Stone et al., 1998).

4.1.2 Application of ^{36}Cl for quantifying the rate and age of surface processes

4.1.2.1 Surface exposure dating of rock avalanche blocks

All geological surfaces that have been stable and exposed to cosmic rays for a long time can be dated using cosmogenic nuclides. These geological features are either depositional, such as moraines, fluvial deposits, and mass wasting blocks, or erosional surfaces carved by glacial and fluvial processes (Dunai, 2010). Cosmogenic nuclides have also been used to determine the recurrence intervals of mass movements (e.g., Ballantyne et al., 2014; Hermanns et al., 2015). Since geological surfaces could experience erosion to some degree, the results of surface exposure dating are reported both with and without erosion (Dunai, 2010). The concentration of cosmogenic nuclides ($C_{(t)}$) in a surface which exposed to cosmic rays can be described by

$$C_{(t)} = \frac{P_{(0)}}{\lambda + \rho\varepsilon/\Lambda}\left(1 - e^{-(\lambda+\rho\varepsilon/\Lambda)t}\right) + C_{in}e^{-\lambda t} \qquad (4.1)$$

where $P_{(0)}$ (atoms g^{-1} yr^{-1}) is the production rate at the Earth's surface, C_{in} the nuclide concentration before the start of exposure (inherited), t (yr) the exposure age of the surface, ρ (g cm^{-3}) the density of the sample, λ (yr^{-1}) the decay constant, ε (cm yr^{-1}) the erosion rate, and Λ (g cm^{-2}) the attenuation length. For calculating the surface exposure age of a sample assuming no erosion and inheritance, equation (4.1) changes to:

$$C_{(t)} = \frac{P_{(0)}}{\lambda}\left(1 - e^{-\lambda t}\right) \qquad (4.2)$$

The half-life of ^{36}Cl is 301 ka. The useful time range for surface exposure dating is about three to four times the half-life of the radionuclide, after which the concentration of cosmogenic nuclides reach saturation i.e., production rate equals loss due to decay and erosion (Ivy-Ochs and Schaller, 2009). In the case of ^{36}Cl, the useful time range for exposure dating is about 1 Ma.

4.1.2.2 ^{36}Cl-derived denudation rate of carbonate outcrops

Denudation of a landscape brings shielded mineral grains from subsurface to the surface. During this travel, mineral grains will accumulate cosmogenic nuclides proportional to the travel time, i.e., proportional to the denudation rate (Dunai, 2010). The concentration of cosmogenic nuclides ($C_{(t)}$) in a mineral grain that is eroding in a steady state condition (Lal, 1991) can be described by:

$$C_{(t)} = \frac{P_{(0)}}{\lambda + (\rho\varepsilon)/\Lambda} \tag{4.3}$$

where $P_{(0)}$ (atoms g^{-1} yr^{-1}) is the production rate at the Earth's surface, ε (cm yr^{-1}) the erosion rate, ρ (g cm^{-3}) the density of the sample, λ (yr^{-1}) the decay constant (for ^{36}Cl $\lambda = 2.303 \times 10^{-6}$ yr^{-1}), and Λ (g cm^{-2}) the attenuation length.

In this thesis, the cosmogenic nuclide ^{36}Cl was applied to quantify the denudation rate of carbonate outcrops based on the steady-state erosion model (Lal, 1991). This model assumes that sufficient time has passed so that the nuclide concentrations are at steady state, reflecting a balance between the production of ^{36}Cl on the one hand and the removal of ^{36}Cl by decay and erosion on the other. Thus, denudation rates have remained constant over a long period. In a steadily eroding terrain, the ^{36}Cl concentration depends on the time that mineral grains have spent near the surface (i.e., the uppermost few meters) and is inversely related to denudation rates (Lal, 1991; Bierman, 1994). This approach provides the long-term denudation rates integrated over the time required to remove one average attenuation length (~160 cm. g^{-2}) or 60 cm of rock with a density of 2.6 g.cm^{-3} (Lal, 1991; Riebe et al., 2003). The time interval over which cosmogenic ^{36}Cl-derived denudation rates are averaged depends on the denudation rate and ranges between 10^4 and 10^6 years for the rates observed so far.

4.1.3 Field sampling procedures

4.1.3.1 Sampling carbonate bedrocks for denudation studies

Thirteen samples were collected from the carbonate bedrocks (11 limestones and 2 marbles) in the south of the CAP (Figure 3.2a). The sampling sites are distributed over three different climatic and geographic regions: two samples (DEN-01 and 02) are from the coastal region with a temperate Mediterranean climate, eight samples (DEN-03 to DEN-10) from the Central Taurides with a continental climate, and three samples (DEN-11, 12, and 13) from the CAP interior with arid climate (Figure 3.2b). The samples are also from three different lithostratigraphic units with various topographic and physical characteristics; samples DEN-01 to DEN-05 are from hilltop outcrops of Jurassic-Cretaceous neritic limestone, samples DEN-06 to DEN-11 are from the flat plateau surface of the Miocene neritic limestone, and samples DEN-12 and DEN-13 are from the top of Middle Triassic-Jurassic marble domes. To evaluate the role of climate and tectonics on denudation of carbonate terrains, sampling sites were selected mainly along two transects (A and B) extending from SW to NE (Figurs 3.1b and 3.2c and 3.2d), roughly perpendicular to the strike of the Taurides, and parallel to main storm tracks (Şahin and Türkeş, 2013). The first transect (Transect-A) stretches from the Mediterranean coast to the Taurides in the west and includes three sampling sites (DEN-01, 02, and 03). The second transect (Transect-B) to the east runs over the plateau, extending from the plateau edge in the Central Taurides to the CAP interior, including six sampling sites (DEN-06, 07, 08, 09, 10, and 11). Several sampling sites (DEN-04, 05, 12, and 13) are located between these transects. Except for two samples (DEN-01 and 02) from the coastal region, all others are from above the plateau surface. High-elevation flat-lying outcrops preferentially were selected for sampling, which presumably are the most stable parts of the landscape, unaffected by mass wasting and less affected by soil dynamics. About 1 kg samples were collected manually using a chisel and hammer from the uppermost 1.5–3 cm of bedrocks. The samples were collected from elevations <2200 m asl to avoid surfaces that were shaped by glaciations, as these have been limited to higher elevations (Messerli, 1967; Sarıkaya and Çiner, 2017). At the sampling sites, either there is no soil cover on the bedrock, or it is limited to fractures and weathering pits. Topographic shieldings were measured for each sample site at every 45° from the north using a compass and an inclinometer. Further information on sampling sites is given in Table 4.1.

Table 4. 1 : Location, climate, topographic data, and local corrections to production rates for denudation samples.

Sample ID	Site/ Landform/ Lithology	Latitude	Longitude	Elev.	THK	Shield	MAP	MAT	Dist.
		°N (DD)	°E (DD)	(m)	(cm)	unitless	(mm)	(°C)	(km)
DEN-01	Adrasan/Hilltop/Lmst	36.32714	30.39047	770	3	0.99976	676	16.02	6.0
DEN-02	Bucak/Hilltop/Lmst	37.26044	30.73323	675	2	0.98981	611	14.52	42.5
DEN-03	Barla/Hilltop/Lmst	38.26791	30.73365	1630	3	0.99990	586	9.03	159.0
DEN-04	Dedegöl/Hilltop/Lmst	37.78375	31.24911	1935	2	0.99297	630	6.42	109.0
DEN-05	Geyikdağ/Hilltop/Lmst	36.96748	31.92970	2040	1.5	0.99872	693	7.18	44.0
DEN-06	Taşeli-I/Plataeu/Lmst	36.34117	32.58952	2230	1.5	1	769	7.02	27.5
DEN-07	Taşeli-II/Plataeu/Lmst	36.42975	32.71398	1910	2.5	0.99919	730	7.79	42.3
DEN-08	Ermenek-I/Plataeu/Lmst	36.69687	32.83882	1860	3	1	656	8.76	69.6
DEN-09	Ermenek-II/Plataeu/Lmst	36.68194	32.94462	1750	1.5	1	636	9.29	77.0
DEN-10	Sertavul/Plataeu/Lmst	36.89926	33.31964	1715	2	1	548	9.16	119.0
DEN-11	Karaman/Plataeu/Lmst	37.30657	33.81848	1385	3	0.99995	424	10.33	182.0
DEN-12	Konya/Hilltop/marble	37.51569	33.16922	1224	1.5	0.99967	405	10.74	152.0
DEN-13	Cihanbeyli/Hilltop/marble	38.13348	32.73594	1205	2	1	436	10.28	196.0

Lmst (limestone), Elev. (Elevation asl), THK (Thickness of sampled rock), Shield (topographic shielding correction factor), MAP (Mean Annual Precipitation), MAT (Mean Annual Temperature), Dist. (Distance from the coastline)

4.1.3.2 Sampling rock avalanche boulders for surface exposure dating

Eight samples were collected for surface exposure dating; six samples from the rock avalanche boulders and two from a lateral moraine, which was partially buried by the rock avalanche deposit. The samples were collected from the terminal part of the rock avalanche deposit to avoid sampling boulders that may be toppled later from the cliff. The boulders were huge (some >10 m in diameter) and highly intertwined, making the post-depositional movement less likely. There were also lichen assemblages on some sampled boulders showing the boulders were stable for a long time. Moreover, the largest possible blocks were sampled to prevent the risk of sampling overturned boulders. A thin rock veneer with a thickness of ~1.5–3 cm was sampled from the flat top surface of each boulder, away from the edges, using a chisel and a hammer. The field information of all samples such as location, elevation, thickness, size, and topographic shielding correction, were recorded in the field (Table 4.2).

Table 4. 2 : Location, topographic data and local corrections to production rates for rock avalanche samples.

Sample ID	Latitude	Longitude	Elevation	Boulder dimensions (L×W×H)	Thickness	Shielding
	°N (DD)	°E (DD)	(m)	(m)	(cm)	unitless
RF19-01	36.98321	32.04167	2154	4.2 × 5.6 × 3.5	2.5	0.98799
RF19-02	36.98373	32.04186	2156	2.8 × 3.5 × 3.9	2	0.99033
RF19-03	36.98464	32.04216	2139	4.3 × 2.1 × 1.5	3	0.99043
RF19-04	36.98581	32.04270	2125	1.5 × 1.3 × 0.9	2	0.99184
RF19-05	36.98699	32.04346	2120	1.2 × 1 × 0.8	1.8	0.9952
RF19-06	36.98802	32.04308	2114	7 × 3.5 × 6	2	0.9936
RF19-07	36.98740	32.04222	2122	15 × 8 × 10	2	0.99458
RF19-08	36.98722	32.04116	2122	10 × 12 × 5	2	0.98978

4.1.4 Chemical preparation

Chemical preparation of the samples and chlorine extraction were performed according to the procedures of Schimmelpfennig et al. (2009) and Sarıkaya (2009) at İTÜ/KozmoLab (Istanbul Technical University, Türkiye). Samples were crushed, ground and sieved to get a grain size of 0.25–1 mm. The whole-rock samples were leached with deionized water and dilute HNO_3 (10%) to remove any meteoric chlorine and secondary carbonate from the grain boundaries. Approximately 1 g of a mixture of natural NaCl (Merc Emsure) and ^{35}Cl-enriched spike (^{35}Cl purity ~99.7%, Aldrich Co.) was added to all samples and the blank before complete dissolution with 10% HNO_3. Chloride was separated and precipitated from the solution as AgCl by adding 0.1 M silver nitrate. After the first chlorine extraction, to prevent sulfur-36, an isobar of ^{36}Cl, from interfering with the ^{36}Cl measurements in accelerator mass spectrometry (AMS), it was removed from the solution by repeated addition of $Ba(NO_3)_2$ and precipitation as $BaSO_4$. Finally, $^{37}Cl/^{35}Cl$ and $^{36}Cl/Cl$ ratios were measured at the same target with SIRIUS tandem accelerator at the Australian Nuclear Science and Technology Organization (ANSTO), Sydney, Australia (Wilcken et al., 2017, 2019). AMS measurements were normalised to Z93-0005 primary standard from PRIME laboratory with reference value of $^{36}Cl/Cl$ of 1.2×10^{-12}. Blank subtractions were done for the Cl and ^{36}Cl concentrations. Concentrations of major and trace elements (Tables 4.3 and 4.4) were analysed by inductively coupled plasma mass spectrometry (ICP-MS) at Activation Laboratories Inc., Ontario, Canada.

Table 4. 3 : Major and trace element concentrations for denudation samples.

Sample ID	Major elements (wt. %)										Trace elements (ppm)			
	Al_2O_3	CaO	Fe_2O_3	K_2O	MgO	MnO	Na_2O	P_2O_5	SiO_2	TiO_2	CO_2 (LOI)	Sm	Gd	U	Th
DEN-01	0.08	48.02	0.12	0.03	6.79	<0.01	0.01	<0.01	0.27	<0.01	44.50	<0.05	0.08	0.9	<0.2
DEN-02	0.09	55.20	0.08	0.03	0.47	<0.01	0.02	<0.01	0.22	<0.01	43.80	<0.05	<0.05	3.0	<0.2
DEN-03	<0.01	55.87	0.07	<0.01	0.47	<0.01	<0.01	<0.01	0.09	<0.01	43.40	<0.05	<0.05	3.8	<0.2
DEN-04	0.05	55.00	0.06	0.01	0.73	<0.01	0.02	0.02	0.18	<0.01	43.90	0.07	0.17	0.3	<0.2
DEN-05	0.31	54.83	0.11	0.10	0.65	<0.01	0.02	<0.01	0.70	0.01	43.20	0.15	0.20	1.9	0.2
DEN-06	<0.01	55.16	<0.04	<0.01	0.40	<0.01	<0.01	0.03	0.08	<0.01	44.20	<0.05	0.09	1.7	<0.2
DEN-07	0.16	54.55	0.14	0.03	0.45	<0.01	0.01	0.05	0.50	0.01	44.00	0.17	0.26	1.1	<0.2
DEN-08	0.06	55.30	0.10	0.01	0.51	<0.01	<0.01	0.04	0.20	<0.01	43.70	<0.05	0.16	1.2	<0.2
DEN-09	0.06	54.52	0.04	0.01	0.64	<0.01	0.01	0.04	0.23	<0.01	44.40	0.05	0.11	3.7	<0.2
DEN-10	0.08	55.62	0.08	0.02	0.22	<0.01	<0.01	0.02	0.28	<0.01	43.60	0.09	0.24	0.3	<0.2
DEN-11	0.24	54.97	0.09	0.03	0.34	<0.01	<0.01	0.03	0.57	0.02	43.70	0.07	0.12	0.3	<0.2
DEN-12	0.02	56.40	0.05	<0.01	0.29	<0.01	<0.01	<0.01	0.22	<0.01	43.00	<0.05	0.06	0.8	<0.2
DEN-13	<0.01	56.95	<0.04	<0.01	0.10	<0.01	<0.01	<0.01	0.06	<0.01	42.80	<0.05	<0.05	0.2	<0.2

Table 4. 4 : Major and trace element concentrations for rock avalanche samples.

Sample ID	Major elements (wt. %)										Trace elements (ppm)			
	Al_2O_3	CaO	Fe_2O_3	K_2O	MgO	MnO	Na_2O	P_2O_5	SiO_2	TiO_2	CO_2 (LOI)	Sm	Gd	U	Th
RF19-01	0.11	55.28	0.07	0.03	0.51	<0.01	<0.01	0.03	0.24	<0.01	43.7	<0.05	0.06	0.2	<0.2
RF19-02	0.03	55.56	<0.04	0.02	0.46	<0.01	<0.01	<0.01	0.13	<0.01	43.7	<0.05	<0.05	0.1	<0.2
RF19-03	0.08	55.38	0.04	0.02	0.41	<0.01	<0.01	0.02	0.17	0.06	43.8	<0.05	0.06	0.2	<0.2
RF19-04	0.07	55.69	<0.04	0.02	0.43	<0.01	<0.01	0.01	0.14	<0.01	43.6	<0.05	0.06	0.6	<0.2
RF19-05	0.07	55.54	0.05	0.03	0.43	<0.01	<0.01	0.01	0.18	<0.01	43.6	<0.05	0.08	0.2	<0.2
RF19-06	0.24	55.02	0.08	0.06	0.50	<0.01	<0.01	0.01	0.45	0.01	43.6	<0.05	0.09	0.3	0.3
RF19-07	0.04	56.05	0.04	0.01	0.39	<0.01	<0.01	<0.01	0.11	<0.01	43.3	<0.05	0.05	0.3	<0.2
RF19-08	0.41	54.70	0.12	0.10	0.49	<0.01	0.01	0.06	0.71	0.02	43.3	0.08	0.16	0.7	0.4

4.1.5 Calculations

4.1.5.1 Calculation of ^{36}Cl-derived denudation rates

^{36}Cl-derived denudation rate was calculated using CRONUScalc 2.1 MATLAB scripts (Marrero et al., 2016a, 2018), which models nuclide concentrations using an iterative computation method. In this method, the code iteratively changes denudation rates to find the best-fit nuclide concentration that matches the measured nuclide concentration. The denudation rates were calculated assuming steady state erosion (i.e., infinite exposure time in the model output), providing information on the maximum denudation rates (Lal, 1991; Bierman, 1994). The rates are maximum because in reality the steady-state assumption may not be valid for the sampled bedrock surfaces, so that the true denudation rates can be lower than the calculated

rates (e.g., Lal, 1991; Small et al., 1997.; Ivy-Ochs and Schaller, 2009; Marrero et al., 2018). CRONUScalc 2.1 uses the CRONUS-Earth production rates (Borchers et al., 2016; Marrero et al., 2016b; Phillips et al., 2016), with some modified or recalibrated production rates later updated by Marrero et al. (2021). Lal (1991)/ Stone (2000) scaling (ST) scheme was used to calibrate production rates to SLHL. Production rate calibration values for ST scaling include 52.2 ± 3.7 atoms ^{36}Cl (g Ca)$^{-1}$ yr^{-1} for Ca spallation, 150 ± 11 atoms ^{36}Cl (g K) $^{-1}$ yr^{-1} for K spallation, and 649 ± 230 neutrons (g air)$^{-1}$ yr^{-1} for fast neutrons (Marrero et al., 2021). For 10 samples, the measured rock densities in the laboratory were used to calculate denudation rates. For the other 3 samples (DEN-01, 04, and 11) that density could not be measured, a constant value of 2.7 (g/cm^3) was used.

4.1.5.2 Calculation of surface exposure ages

CRONUS Earth Web Calculator v.2.1 (http://cronus.cosmogenicnuclides.rocks/2.1/) (Marrero et al., 2016a) was employed to calculate the exposure age of boulders. Lal (1991)/ Stone (2000) scaling factor (ST) was used as the scaling schema to normalize the production rate to SLHL (Lal, 1991; Stone, 2000). Surface exposure ages were calculated using an SLHL ^{36}Cl production rate of 52.2 ± 5.2 ^{36}Cl atoms (g Ca)$^{-1}$ a^{-1} for Ca spallation, 150 ± 15 ^{36}Cl atoms (g K)$^{-1}$ a^{-1} for K spallation, and 696 ± 185 for fast neutrons (g air)$^{-1}$ a^{-1} (Stone, 2000; Phillips et al., 2016; Marrero et al., 2016b). The topographic shielding for each sampling location was calculated using an online calculator (Balco et al., 2008) to correct the effect of topographic irregularities. For snow-shielding correction, WorldClim v.2.1 (Fick and Hijmans, 2017) was used to estimate probable snow thickness. Since Geyikdağ Mountain is located in a semi-arid climate with low mean annual precipitation, 25 cm snow cover was assumed on top of the boulders, which resulted in a snow-shielding factor of 0.98. However, snow cover had a minor effect on the age results, causing only a ~1.6% increase. Thus, the final age results were reported without snow correction. Boulder ages were calculated with and without erosion using an estimated 10 mm/ka bedrock erosion rate. The erosion-corrected ages were accepted as final age results because the surface of the sampled blocks had some evidence of karstic solutions.

4.2 Compilation of Climatic and Topographic Metrics and Measuring Physical Properties of denudation samples

4.2.1 Climatic and topographic metrics

The climate proxies were derived from WorldClim 2.1 (Fick and Hijmans, 2017) for each sampling site with a spatial resolution of 1 km for 1970–2000. The mean annual precipitation (MAP, mm) and the mean annual temperature (MAT, °C) were used as climate proxies. MAP and MAT range from 400 to 770 mm and from 6 to 16 °C, respectively, across the sampling sites (Table 4.1, Figures 3.2c and 3.2d). 1:25,000 scale printed topographic maps and the 30 m resolution Shuttle Radar Topography Mission (SRTM) Digital Elevation Model (DEM) were used to derive the topographic metrics. "Elevation" and "distance from the coastline" were considered as topographic metrics. The elevation of the sampling sites was extracted from printed 1:25,000 scale topographic maps, ranging between 675 and 2230 m asl (Table 4.1). The distances from the coastline were derived from the DEM, parallel to transect A for samples DEN-01 to 4 and to transect B for DEN-05 to 13. The closest (DEN-01) and farthest (DEN-13) samples are 6 and 196 km away from the Mediterranean Sea, respectively (Table 4.1).

4.2.2 Schmidt Hammer measurements

The mechanical strength (hardness) of the rock can indicate its resistance to physical weathering (Ryb et al., 2014b). The Schmidt Hammer test is the most common method for evaluating the mechanical strength of the rocks and the degree of weathering in geomorphology (e.g., Matthews et al., 2016; Goudie, 2016). By pressing the Schmidt Hammer against the rock surface, its plunger automatically releases, and the rebound distance is recorded in a range from 10 to 100. The rebound value (R-value) reflects the compressive strength (i.e., hardness) of the rock surface.

The rebound value (R-value) of carbonate bedrocks was measured at all sampling sites using an N-type mechanical Schmidt Hammer (2.207 Nm impact energy) tested on the manufacturer's test anvil and calibrated before and after fieldwork. At each field site, 20 R-values were measured on lichen-free, horizontal, dry bedrock surfaces away from edges and cracks. The R-values for each sampling site were calculated following the Yavuz et al. (2006) procedure, which suggested recording 20 R-values and averaging the top 10 values.

4.2.3 Measuring bulk density, prosity and water absorption by weight

Some physical properties of carbonate rocks, including bulk density, porosity, and water absorption by weight were measured in all samples except three (DEN-01, 04, and 11), since suitable boulders were not available at those sites. To measure these physical properties, a boulder with the same lithology as the bedrock was collected in the vicinity of cosmogenic sampling sites. Cubic samples were prepared from the fracture-free core of each boulder by sawing to 70 mm edge length. The bulk density of the samples was determined using the saturation and buoyancy methods and the porosity using the dry versus wet weighing method, following the procedures recommended by Franklin (1979) and the Turkish Standard Institution (TS EN 1936, 2006; TS 699, 2009). In this approach, the weights of the "oven-dry" and "saturated-surface-dry" samples were measured, as well as measuring their bulk volume using Archimedes' principle. Subsequently, the bulk density, porosity, and water absorption by weight were calculated based on the measured parameters. Density plays a critical role in determining accurate denudation rates. Assuming a constant density value for all samples can lead to under or overestimation of denudation rates (Nakamura et al., 2014; Evans et al., 2021). Porosity is also an important factor in rock weathering rates because it provides pathways for fluid movement and reduces rock strength (Ballesteros et al., 2010; Goudie, 2016).

4.3 Geomorphological Analysis of the Rock Avalanche

The rock avalanche area, especially the accumulation zone, was surveyed with a UAV (Unmanned Aerial Vehicle)-DJI Mavic Air model to record its geomorphological features. Field investigation, highresolution UAV photos, and aerial photos provided by the General Directorate of Mapping of Türkiye were the main sources for assessing the geomorphological characteristics of the rock avalanche. The commercial software Agisoft Metashape (http://www.agisoft.com/) was used to generate the DEM and the orthophoto from aerial photos. The created orthophoto with a resolution of 19 cm was used to create the geomorphological map of the rock avalanche and to map the metrics of the deposited boulders. The block point density [m^{-2}], and the fraction of area covered by blocks within a 100-m radius was computed using a Gaussian kernel density estimator in the ArcGIS program. Topographic interpretation for elevation variation was done based on the produced 1-meter DEM. Moreover, the 1-m DEM

was employed to create a slope map and provide longitudinal profiles. The geomorphological map and longitudinal profiles were used to measure the geometric features of the rock avalanche. The slope map was employed to show slope changes in the rock avalanche area and delineate the rock avalanche's source area.

5. LONG-TERM DENUDATION RATE OF CARBONATE OUTCROPS

This chapter consists of two parts. The first part presents the calculated denudation rates, the results of the physical properties of the sampled rocks, and the correlation results. The second part discusses the controls of different climatic and topographic metrics as well as rock physical properties on the denudation of carbonate outcrops in the geologic setting of southern CAP.

5.1 Results

5.1.1 ^{36}Cl-derived denudation Rates

Measured ^{36}Cl concentrations range from 5.667×10^5 to 1.077×10^7 (atoms/g of rock), and the natural Cl contents vary from ~2 to 34 ppm (Table 5.1). All samples have high CaO content, ranging from 48 to 57 wt. % (Table 4.3). Low Cl and K and high Ca contents dictate that ^{36}Cl production is dominated by ^{40}Ca spallation and muon capture (93%), whereas ^{35}Cl neutron capture and ^{39}K spallation and muon capture are responsible for much less (6.6 and 1%, respectively).

Both the denudation rate (length per time) and the denudation flux (mass per area per time) of bedrock outcrops are presented. Denudation flux can be directly converted to denudation rate using the density of sampled rocks. Outcrop denudation rates range from 1.92 ± 0.31 mm/ka to 45.77 ± 3.91 mm/ka (Table 5.1, Figure 5.1a and 5.1b), which correspond to denudation fluxes between 0.52 ± 0.08 and 12.36 ± 1.06 g/cm^2/ka (Table 5.1). The integration time of denudation rates ranges from 312 to 13 ka. Uncertainties in calculated denudation rates are in one standard deviation (±1σ), which includes all analytical uncertainties in data measurements and errors due to the production rate calculations.

The mean and median denudation rates for all samples (n = 13) are 14.40 ± 0.47 mm/ka and 12.42 ± 1.31 mm/ka, respectively, and exclusively for the Central Taurides (n = 8) are 13.29 ± 0.50 mm/ka and 12.45 ± 0.91 mm/ka, respectively (Figure 5.1c). The higher mean values than the median in both data sets reflect a slightly right-skewed

data distribution (Figure 5.1c), with most samples having relatively low denudation rates. The right-skewed distribution suggests that the median values better represent the central tendency than the mean values for both data sets. For the "all samples" data set, a relatively high mean is the effect of sample DEN-01 (45.77 ± 3.91 mm/ka), which exceeded the upper boundary of the boxplot and seems an outlier. Although this sample can statistically be considered as an outlier, it is within the range of long-term denudation rates for carbonates in temperate Mediterranean climates (e.g., Ryb et al., 2014b; Avni et al., 2019). Indeed, one should expect a large variation in carbonate denudation rates that emerges from the 'geological' noise, which is not accounted for by the analytical uncertainty. Therefore, we did not consider the sample DEN-01 as an outlier. The first and third quartiles for all samples are 7.12 ± 0.56 mm/ka and 18.85 ± 1.31 mm/ka, respectively, and for the Central Taurides are 9.53 ± 0.72 mm/ka and 18.01 ± 1.32 mm/ka, correspondingly. A landscape view of each sampling site is presented in the Figures. 5.2 and 5.3.

Table 5. 1 : AMS analytical data and denudation rate results.

Sample ID	AMS results											
	^{36}Cl (at./g of rock)	^{36}Cl - error (at./g of rock)	Natural Cl (ppm)			Denudation flux (g/cm^2/ka)			Denudation rate (mm/ka)		
DEN-01	5.67E+05	2.75E+04	21.8	±	1.0	12.36	±	1.06	45.77	±	3.91
DEN-02	1.19E+06	7.02E+04	33.9	±	2.4	6.04	±	0.62	22.35	±	2.31
DEN-03	3.60E+06	2.09E+05	12.0	±	0.9	3.18	±	0.32	11.72	±	1.17
DEN-04	4.20E+06	2.40E+05	16.5	±	1.2	3.37	±	0.34	12.49	±	1.25
DEN-05	3.70E+06	2.10E+05	32.8	±	2.2	4.66	±	0.49	17.32	±	1.83
DEN-06	3.72E+06	2.12E+05	10.3	±	0.7	4.56	±	0.43	19.00	±	1.81
DEN-07	3.80E+06	2.31E+05	3.2	±	0.2	3.29	±	0.33	18.70	±	1.89
DEN-08	6.10E+06	3.77E+05	2.1	±	0.2	1.79	±	0.20	7.33	±	0.82
DEN-09	6.00E+06	3.66E+05	3.1	±	0.2	1.67	±	0.19	7.30	±	0.82
DEN-10	4.50E+06	2.74E+05	3.7	±	0.3	2.40	±	0.25	12.42	±	1.31
DEN-11	1.08E+07	6.95E+05	8.7	±	1.0	0.52	±	0.08	1.92	±	0.31
DEN-12	6.94E+06	3.92E+05	24.4	±	1.6	1.05	±	0.14	3.88	±	0.50
DEN-13	4.19E+06	2.43E+05	8.9	±	0.5	1.84	±	0.20	6.93	±	0.75

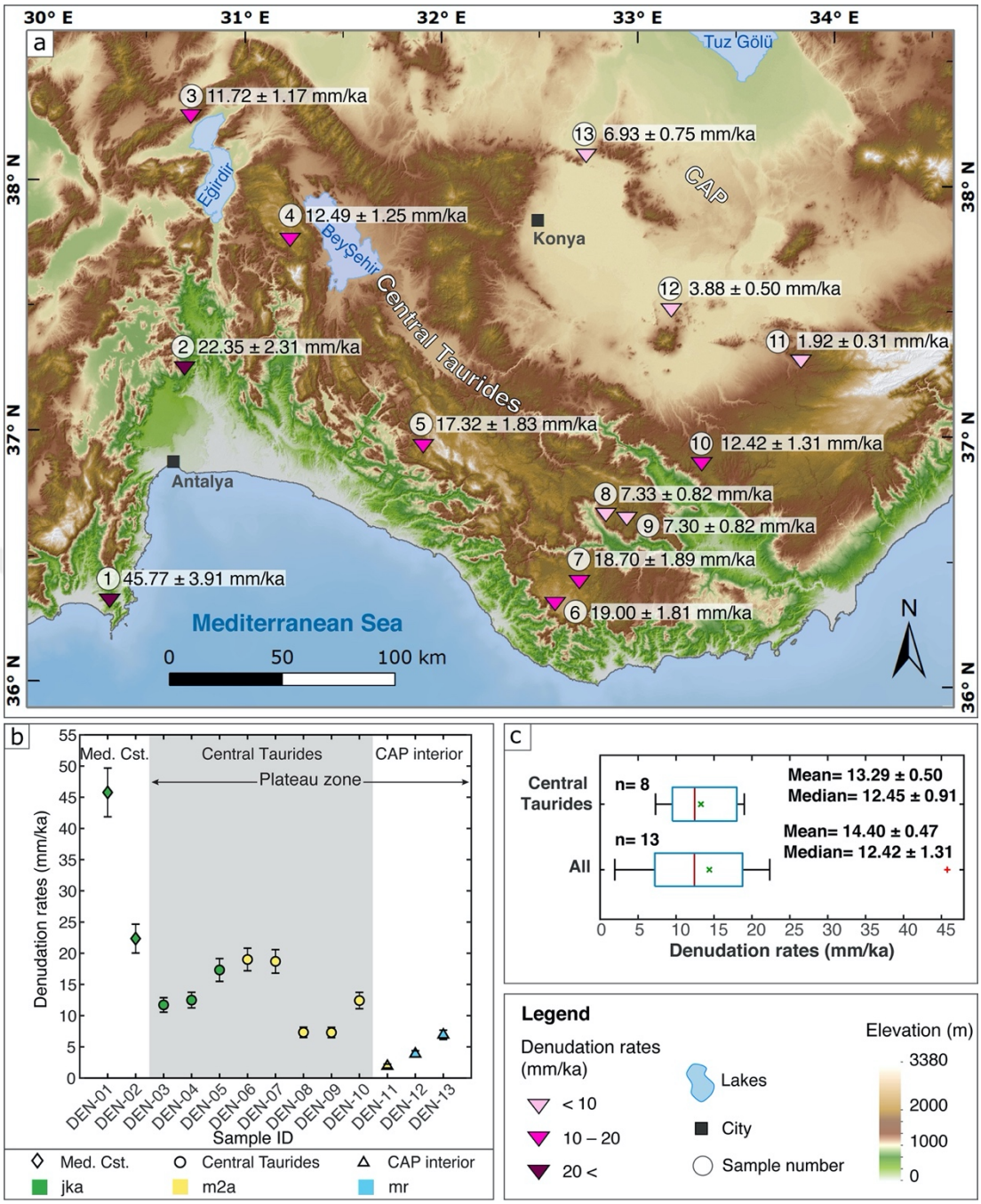

Figure 5. 1 : (a) Shaded relief map of the study area showing sampling sites and ^{36}Cl-derived outcrop denudation rates. Sample names are abbreviated to 1–13 and are shown inside the circle. (b) Scatter plot of ^{36}Cl-derived denudation rates (mm/ka). Diamond, circle, and triangle symbols indicate the Mediterranean coastal region (Med. Cst.), the Central Taurides, and the Central Anatolian Plateau (CAP) interior, respectively. Green, yellow, and blue colors represent Jurassic-Cretaceous limestone (jka), Miocene limestone (m2a), and Middle Triassic-Jurassic marble (mr), respectively, on the geological map (Figure 3.2a). The gray area shows the samples of the Central Taurides. The error of the points without a visible error bar is smaller than the symbol. (c) Boxplots for "All samples" and for "Central Taurides samples". The associated box shows 25th and 75th percentiles, the median (red vertical line), and the mean (green multiplication sign). The whiskers indicate the data range, excluding the statistical outlier (red cross sign). This figure was taken from Hashemi et al. (2023).

Figure 5. 2 : Field photographs of the sampling sites. (a) and (b) sampling sites on the hilltops of Jurassic-Cretaceous neritic limestones. (c) Sampling site on the flat plateau with Miocene neritic limestone. (d) and (e) sampling sites on the hilltops of marble domes. The red arrow indicates the sampling locations. This figure was taken from Hashemi et al. (2023).

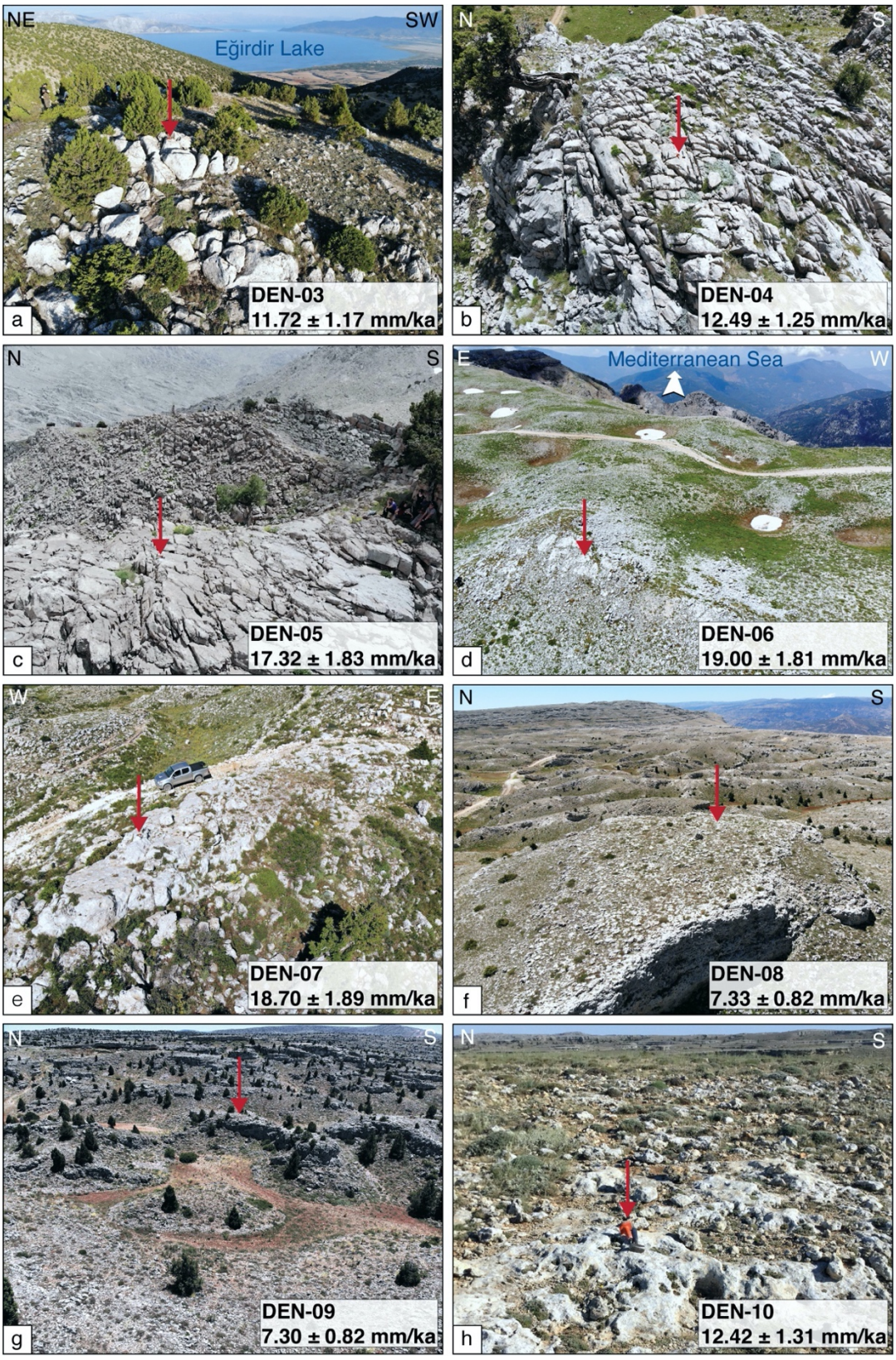

Figure 5. 3 : Field photographs of sampling sites in the Central Taurides. (a), (b), and (c): sampling sites on the hilltops of Jurassic-Cretaceous neritic limestones. (d), (e), (f), (g), and (h): Sampling sites on the flat plateau with Miocene neritic limestone. The red arrow indicates the sampling locations. This figure was taken from Hashemi et al. (2023).

5.1.2 Rock mechanical strength and physical properties

Schmidt Hammer R-values for the sampled bedrocks range from ~31 to 53 (Table 5.2). Mean R-values for Middle Triassic-Jurassic marble, Jurassic-Cretaceous neritic limestone, and Miocene neritic limestone are 50.2, 47.4, and 38.8, respectively. The rocks with R-values between 35 and 40 are weak, while the ones with R-values between 40 and 50 are considered as moderately strong (Goudie, 2006). Bulk densities vary between 1.8 and 2.7 (g/cm^3) (Table 5.2). While the marble and Jurassic-Cretaceous limestone samples have densities of 2.7 (g/cm^3), pure calcite density, the Miocene limestone samples show lower densities, especially samples DEN-07 and DEN-10 with densities of 1.8 and 1.9 (g/cm^3), respectively. Porosities range from 0.2 to 24.4%, while water absorption by weight varies from 0.1 to 13.9% (Table 5.2). The highest porosity and water absorption by weight values belong to the samples of the Miocene limestone. Overall, the measured physical properties showed that the marble and Jurassic-Cretaceous limestone are dense rocks with high mechanical strength and bulk density and low porosity and water absorption capacity, while the Miocene limestone is quite porous with the lowest mechanical strength and density values.

Table 5. 2 : Physical properties of denudation samples.

Sample ID	Saturated wt.	Dry wt.	vol.	Pore vol.	Solid Part vol.	Bulk Density	por.	WAW	R-Value
	(g)	(g)	(cm^3)	(cm^3)	(cm^3)	(g/cm^3)	(%)	(%)	unitless
DEN-01	NA	NA	NA	NA	NA	NA	NA	NA	49.4
DEN-02	991.52	989.91	367.26	1.61	365.65	2.70	0.4	0.2	53.2
DEN-03	1005.75	1004.14	371.19	1.61	369.58	2.71	0.4	0.2	47.4
DEN-04	NA	NA	NA	NA	NA	NA	NA	NA	44.5
DEN-05	1002.44	999.94	371.16	2.5	368.66	2.69	0.7	0.3	42.4
DEN-06	933.8	912.56	379.55	21.24	358.31	2.40	5.6	2.3	39.1
DEN-07	784.53	689.09	391.38	95.44	295.94	1.76	24.4	13.9	31.6
DEN-08	931.72	910.27	372.73	21.45	351.28	2.44	5.8	2.4	43.2
DEN-09	891.51	863.35	377.4	28.16	349.24	2.29	7.5	3.3	36.5
DEN-10	784.56	723.7	374.97	60.86	314.11	1.93	16.2	8.4	35.0
DEN-11	NA	NA	NA	NA	NA	NA	NA	NA	47.5
DEN-12	972.56	971.67	358.27	0.89	357.38	2.71	0.2	0.1	48.7
DEN-13	939.04	934.14	351.7	4.9	346.8	2.66	1.4	0.5	51.7

wt. (weight), vol. (volume), por. (porosity), WAW (water abbsorption by weight), Schmidt Hammer R-Value

5.1.3 Correlation of ^{36}Cl-derived denudation rates with environmental and physical variables

Regression analysis were performed between denudation rates and climatic and topographic variables to investigate potential controls on denudation rates (Figure 5.4), and the physical properties of the carbonate rocks (Figure 5.5). When two samples in the Mediterranean coastal region (DEN-01 and 02) were removed from the regression analysis and regression was restricted to samples above the plateau, the correlation became more significant. Thus, the regression analysis includes 11 samples for all variables, except porosity and water absorption by weight with 9 samples. The correlation results and their coefficient of determination (r^2-value) are summarized below.

The results showed that a strong positive correlation exists between outcrop denudation rate and elevation (r^2 = 0.67) (Figure 5.4a). A moderate negative correlation was found between denudation rate and distance from the coastline (r^2 = 0.55) (Figure 5.4b). In addition, denudation rate showed a strong positive correlation with MAP (r^2 = 0.71), while it indicated a strong negative correlation with MAT (r^2 = 0.69) (Figure 5.4c and 5.4d). Latitude, which may act as a climate proxy, displayed a very weak negative correlation with denudation (r^2 = 0.17) (Figure 5.4e). A weak negative correlation was found between the denudation rate and Schmidt Hammer R-values (r^2 = 0.36) (Figure 5.5a). Furthermore, the denudation rate showed a weak positive correlation with porosity (r^2 = 0.19) and with water absorption by weight (r^2 = 0.20) (Figures 5.5b and 5.5c). Overall, the regression analyses indicated that ^{36}Cl-derived outcrop denudation rates on the plateau are strongly correlated with climate proxies (MAP and MAT) and topographic metrics (elevation and distance from the coastline), while their relationship with the physical properties of the carbonate rocks remains poor.

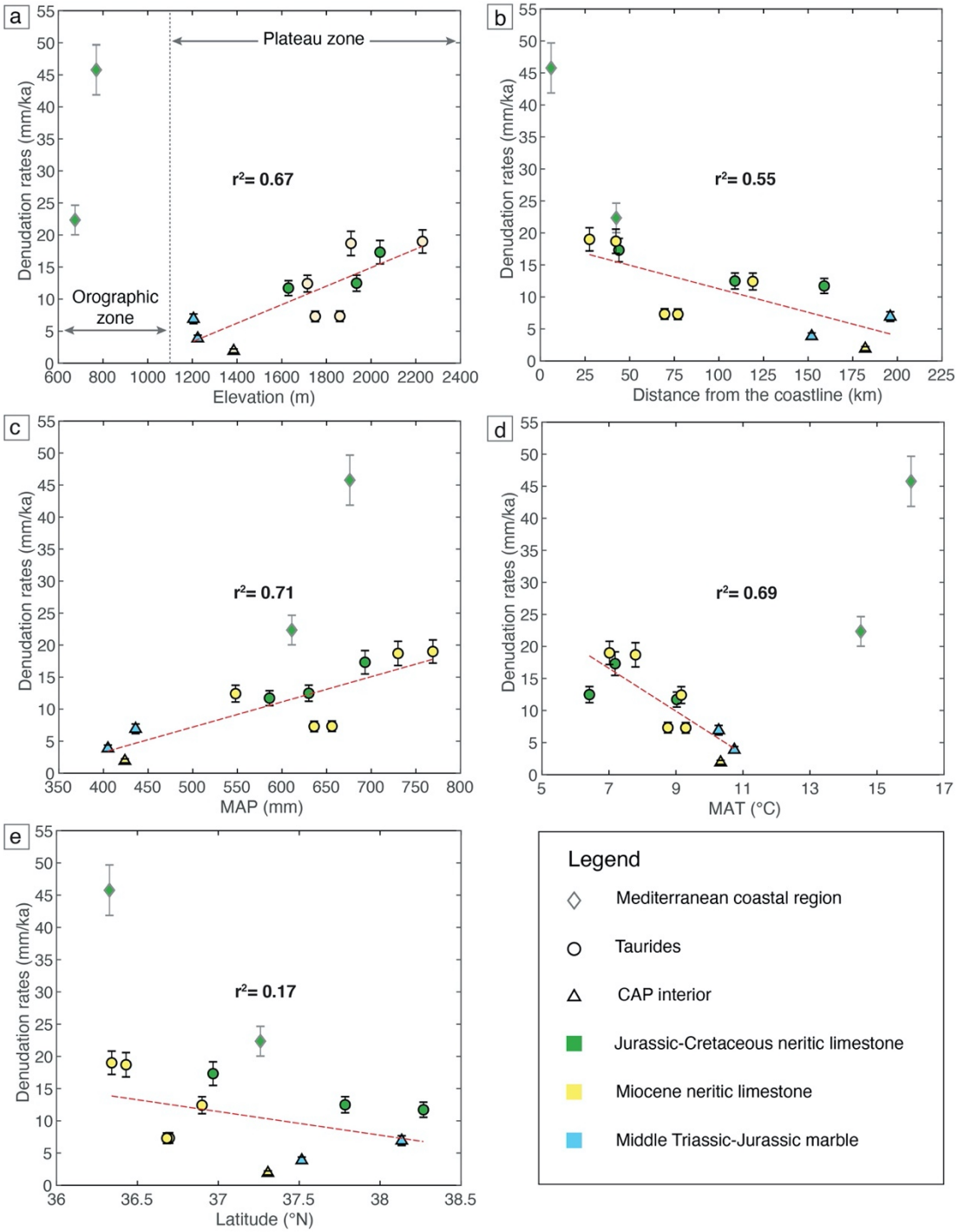

Figure 5. 4 : Scatter plot of ^{36}Cl-derived denudation rates as a function of climatic and topographic variables: (a) elevation (m), (b) distance from the coastline (km), (c) mean annual precipitation (MAP) (mm), (d) mean annual temperature (MAT) (°C), and (e) latitude (°N). For all plots, the regression line belongs to the plateau samples. The two samples (DEN-01 and DEN-02) in the Mediterranean coastal region (diamond symbols with gray error bars) were removed from the regression analysis. The regression lines are shown in red. The error of the points without a visible error bar is smaller than the symbol. This figure was taken from Hashemi et al. (2023).

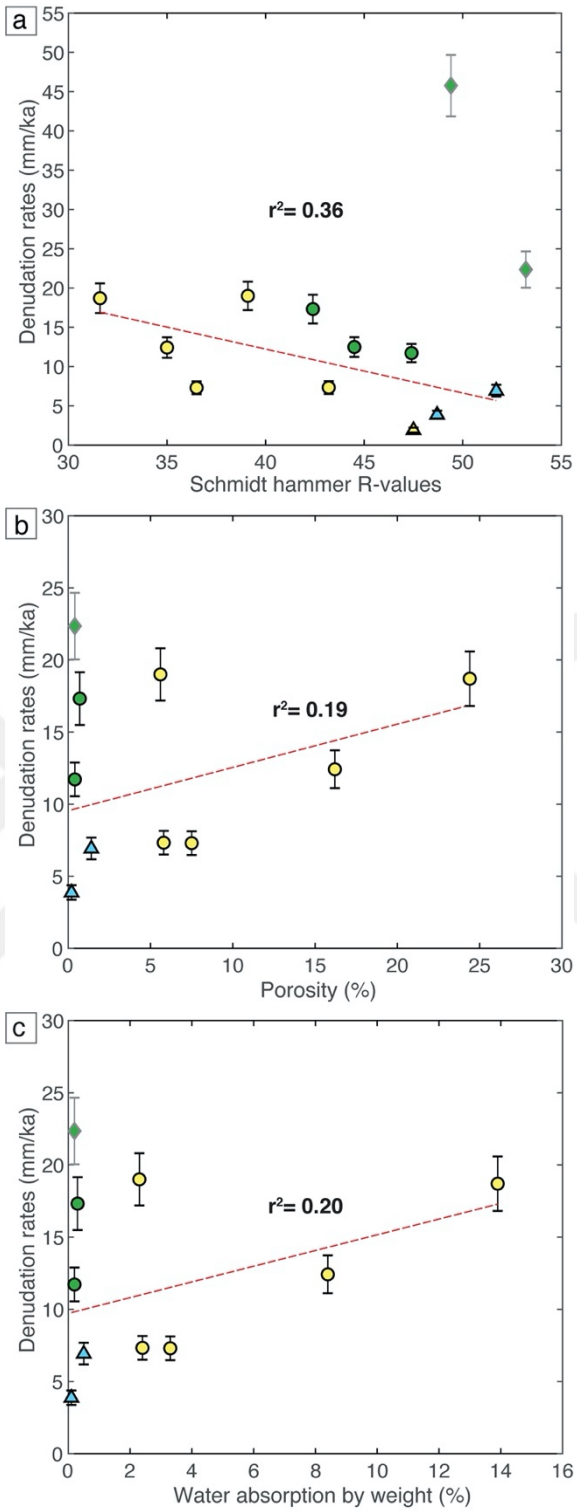

Figure 5. 5 : Scatter plot of ^{36}Cl-derived denudation rates versus physical properties of carbonate rocks. (a) Schmidt Hammer rebound values (R-values), (b) porosity (%), and (c) water absorption by weight (%). The regression line belongs to the samples on the plateau. The two samples (DEN-01 and DEN-02) in the Mediterranean coastal region (diamond symbols with gray error bars) were removed from the regression analysis. For the interpretation of the symbols and colors see Figure 5.4. This figure wass taken from Hashemi et al. (2023).

5.2 Discussion

5.2.1 Sensitivity of denudation rates to bedrock bulk densities

The sensitivity of cosmogenic nuclide-derived denudation rates to density variations has been studied in regolith and soil depth profiles (e.g., Rodés et al., 2011; Nakamura et al., 2014; Evans et al., 2021). However, few studies on the denudation of carbonate bedrock (e.g., Yang et al., 2020; Ben-Asher et al., 2021) have measured the density of the sampled rock. Indeed, carbonate rocks have a wide range of porosities that affect their densities. The density measurements showed that the samples of the Miocene limestone had lower densities (1.8–2.4 g/cm^3), while other samples had densities of 2.7 g/cm^3. To evaluate the sensitivity of the calculated denudation rates to density variations, the denudation rates were recalculated with a constant value of 2.7 g/cm^3. This recalculation showed a 10–35% reduction in denudation rates for the Miocene samples. Particularly, in samples DEN-07 (1.8 g/cm^3) and DEN-10 (1.9 g/cm^3), with the lowest density values, this replacement resulted in a decrease of denudation rates from 18.70 ± 1.89 mm/ka to 12.11 ± 1.23 (35% decrease) and from 12.42 ± 1.31 mm/ka to 8.83 ± 0.93 mm/ka (29% decrease), respectively. Therefore, the generally accepted density value of 2.7 g/cm^3 led to underestimation of denudation rates for the low-density samples. This evaluation highlights the critical role of rock density in determining accurate outcrop denudation rates in carbonate rocks. Particularly, when dealing with high porosity carbonates, direct density measurements must be considered to obtain reliable denudation results.

Moreover, in calculating and reporting denudation rates in carbonate rocks, not only the variation in density should be considered but also whether porosity is part of the denudation process or not. The porosity of the Miocene limestone is partly due to its lithological properties (a marly limestone with a high amount of macro- and microfossils and clay content) and partly due to the erosion processes which started after the emergence of the plateau margin above sea level since the upper Miocene (Öztürk et al., 2017.; Şener and Öztürk, 2019). However, because density (or porosity) was measured on the intact core of the boulders, they are most likely unaffected by erosion processes. Therefore, the measured values were accepted as the primary density and porosity of the rocks. Assuming the current denudation derived the

porosity, the denudation rates calculated with 2.7 g/cm^3 density would be the correct values for the Miocene samples.

5.2.2 Interpretation of denudation rates and controlling factors

5.2.2.1 Climatic control

The evaluated environmental parameters (precipitation, temperature, elevation, and distance from the coastline) are all covarying, associated with adiabatic cooling and orographic precipitation forced by topography. Thus, despite significant correlations with denudation, the covariation between climatic and topographic metrics hinders isolating the respective role of each variable. To capture the influence of climate on denudation, the theoretical maximum dissolution rate equation (White, 1984; White, 1990) was used, which relates three climatic variables; precipitation, temperature, and CO_2 partial pressure. The White equation assumes that water and carbonate rocks reach equilibrium under open-system conditions and follows as

$$D_{max} = \frac{100}{\rho(4)^{1/3}} \left(\frac{K_c K_1 K_{CO_2}}{K_2}\right)^{1/3} {P_{CO_2}}^{1/3} (P - E) \qquad (5.1)$$

where Dmax is the maximum solutional denudation rate (mm ky^{-1}), K_c, K_1, K_2 and K_{CO_2} signify the equilibrium constants for calcite– CO_2– water system (which are dependent on temperature), ρ is the density of bedrock (g/cm^3), P_{CO_2} is CO_2 partial pressure in the atmosphere, P is precipitation (mm yr^{-1}), and E is evapotranspiration (mm yr^{-1}). Calculating the theoretical maximum dissolution rates for the sampling sites, assuming zero evaporation, and comparing them with calculated denudation rates revealed two points. First, all but two of the samples are in the expected range, where the observed denudation rate is less than the predicted maximum dissolution rate (Figure 5.6a). The high denudation rates in the other two samples (DEN-01 and DEN-02) can be related to the mechanical removal of overlying material (rock or soil). It is theoretically impossible for them to be dissolved at the measured rate under the amount of precipitation at those sites. The second point is that the observed denudation rate in the most arid sites (DEN-11, 12, and 13) is considerably slower than expected, which might conceivably be due to more significant evaporation.

Plotting our calculated denudation rates on the theoretical denudation curves from White (1984) showed a general agreement between observed denudation rates and the

predictions (Figure 5.6b). Most of our samples fitted the bare bedrock curves (P_{CO_2} : $10^{-3.5}$) with a temperature range of 5–25°C. This linear trend indicates that precipitation is the main limiting factor of denudation on the plateau. However, two samples with high denudation rates (DEN-02 and DEN-03) did not fit the chemical denudation curve for bare bedrock, indicating the effect of physical erosion.

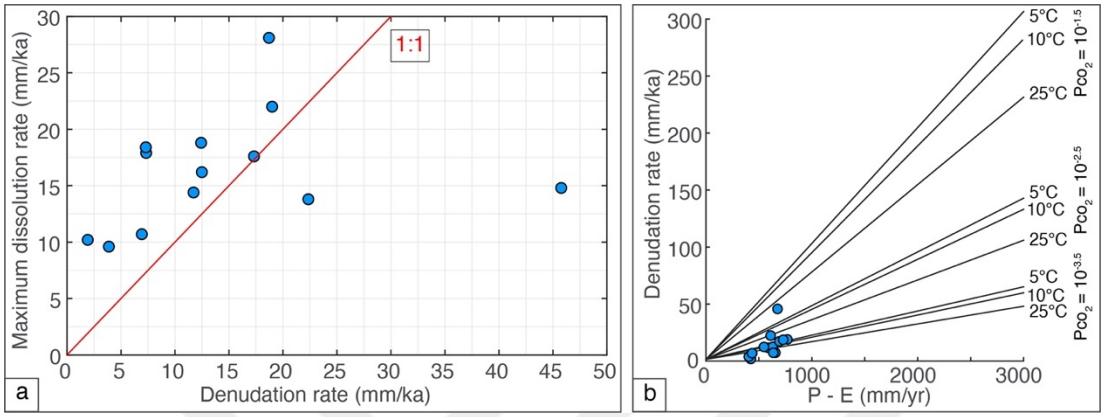

Figure 5. 6 : (a) Calculated denudation rates vs. theoretical maximum dissolution rates of the samples. The red line shows the 1:1 relationship. (b) Theoretical denudation rates for three different temperatures (5, 10, and 25 °C), representative of arctic-alpine, temperate, and tropical climates, and CO_2 pressures of $10^{-3.5}$, $10^{-2.5}$, and $10^{-1.5}$, representative of bare bedrock, normal soils, and organic-rich soils, respectively. We plotted our calculated denudation rates (blue circles) on the theoretical denudation curves. P-E is precipitation minus evapotranspiration. We assumed zero evaporation. This figure was taken from Hashemi et al. (2023), which they adapted from White (1984).

Some studies demonstrated the consistency between carbonate denudation rates and climate zones (Stone et al., 1994; Furlani et al., 2009; Ryb et al., 2014a; Yang et al., 2020), which they attributed to the influence of precipitation or temperature on calcite dissolution (Ford and Williams, 2007; Xu et al., 2013; Ryb et al., 2014a; Gaillardet et al., 2019; Yang et al., 2020). Likewise, we found strong similarities between the magnitude and spatial pattern of denudation rates and climate zones. On the plateau, high-to-moderate denudation rates (10–20 mm/ka) were associated with continental climate (Dsb, cold, dry summer, warm summer) in the Central Taurides, while the lowest denudation rates (<10 mm/ka) corresponded to the arid, steppe, cold climate (BSk) in the CAP interior.

Indeed, denudation rates show a systematic spatial variability with a decreasing trend from SW to NE, which can be traced along two transects, A and B (Figure 5.7a and 5.7c). Climatic and topographic variations are also shown along the transects (Figure 5.7a-d). On the plateau, high denudation rates coincide with high MAP (~700–770

mm) and low MAT (~7–8 °C) at the plateau margin, whereas low denudation rates are associated with low MAP (~400–450 mm) and high MAT (~10–11 °C) in the plateau interior. Precipitation is frequently cited as the main controlling factor on carbonate denudation (Ryb et al., 2014a, 2014b; Yang et al., 2020; Ben-Asher et al., 2021). However, only a 30% increase in denudation rate between 25 and 5 °C interpreted as the least importance of temperature on denudation compared to other climatic variables (White, 1984). Gaillardet et al. (2019) showed that the chemical weathering intensity of carbonates has a boomerang-like relationship with temperature, and in a temperature range from 15 °C to +30 °C maximum dissolution occurs under the temperate condition between 10 and 15 °C. They also pointed out that the misfit between natural data and a temperature-based model for carbonate dissolution indicates that other factors than temperature must have a contribution. In our study, the MAT ranges between 6 and 11 °C on the plateau zone, showing a limited variation (only 2–4° on average). Considering that the correlation with MAP is very strong (r^2 = 0.71) and overall similar (in range and linearity) to the range of values previously observed in carbonate terrains, it seems that precipitation is the main controlling factor of denudation rates.

The low denudation rates in three samples (DEN-11, DEN-12, and DEN-13) in the arid plateau interior show that not only the landscape is slowly evolving, but also the climate has remained stable and arid in this region over a long period. Compared to other arid regions, the low denudation rates in the plateau interior (MAP 300–450 mm) agree to the 0–5 mm/ka and 5–10 mm/ka ^{36}Cl-derived denudation rates in hyperarid (MAP ≤100 mm) and arid (MAP 100–300 mm) regions of Israel, respectively (Ryb et al., 2014a), and to the 4.5 ± 0.7 mm/ka denudation rate of carbonates in the arid region of Australia (Stone et al., 1994). Although the CAP interior has similar denudation rates with other arid regions, it has higher precipitation values. In this study, the regression line (y = 0.039x–12.5) between denudation and MAP does not cross the origin, as predicted by theory, but intersects the y-axis at a negative value (Figure 5.4c), suggesting that the modern MAP is a gross overestimation of the actual MAP over the cosmogenic averaging window. In fact, the effective precipitation has been on average 56% lower than the present-day values over the last ~300 ka, which encompasses the glacial and interglacial periods. This overestimation of paleo-

precipitation is the opposite of the underestimation suggested by Ryb et al. (2014b) for central Israel.

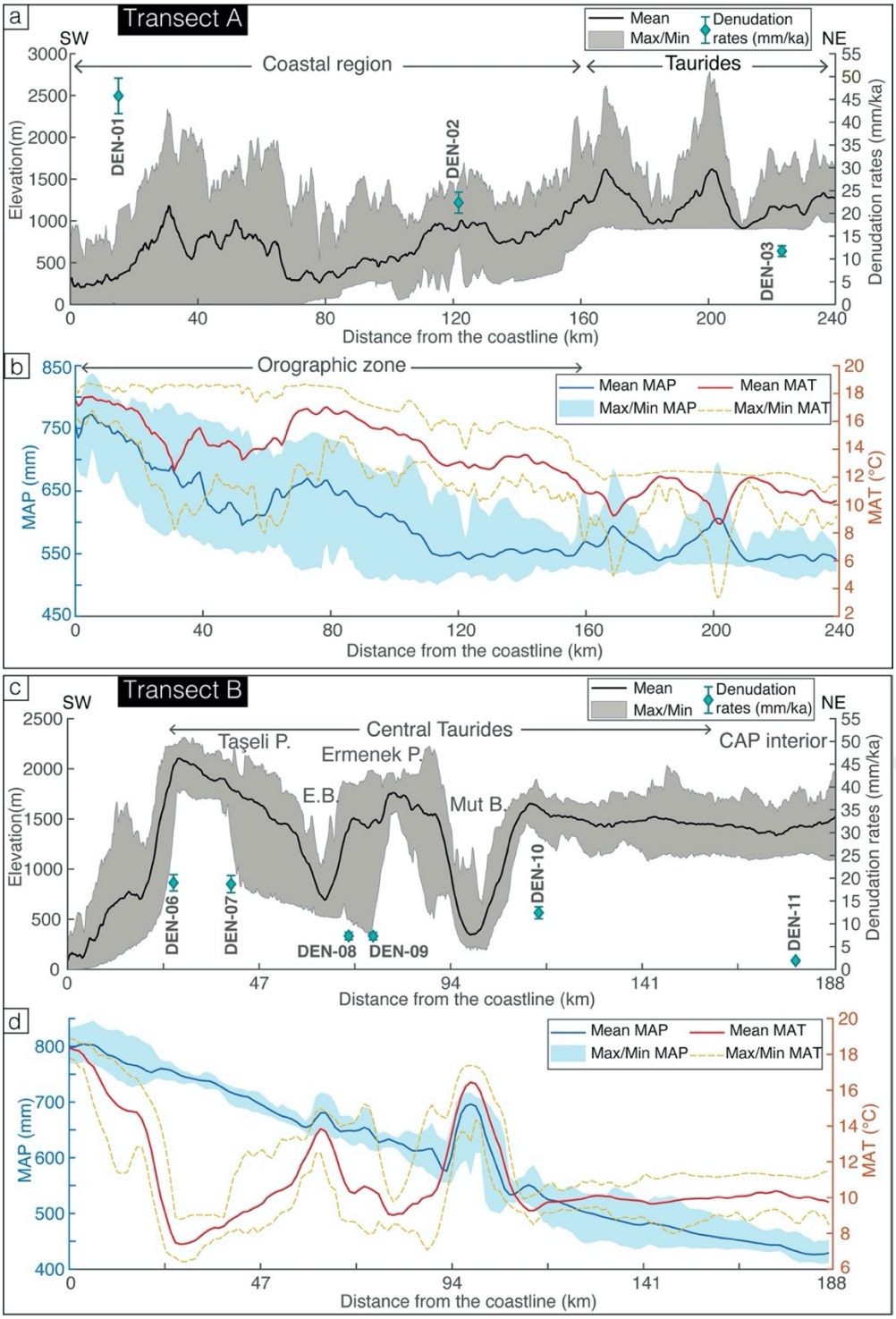

Figure 5. 7 : (a) and (c) Elevation swath profiles, extracted from the 30 m DEM with a vertical exageration of 24, along transects A and B, respectively. (b) and (d) The mean annual precipitation (MAP) and mean annual temperature (MAT) swath profiles, extracted from the WorldClim v.2.1 along transects A and B, respectively. Abbreviations stand for P. (Plateau), B. (Basin), E.B. (Ermenek Basin). The location of transects are shown in Figures 3.1b, 3.2c and 3.2d. The width of the swath profiles is 26 km. This figure wass taken from Hashemi et al. (2023).

Some lines of evidence support the dominance of chemical denudation on the plateau. The strong correlation between denudation rate and MAP, the weak correlation with rock mechanical strength, and the consistency between calculated denudation rates and the theoretical maximum dissolution rates (Figure 5.6a) indicate that chemical denudation has been the dominant mechanism. Previous studies also interpreted the dependence of carbonate denudation on precipitation as an indicator of predominant chemical weathering (Ford and Williams, 2007; Ryb et al., 2014a, 2014b) and decoupling between denudation and rock strength as reflecting insignificant physical erosion (Ryb et al., 2014b).

5.2.2.2 Topographic/tectonic control

In carbonate terrains, the variations in the dominant style of denudation cause strikingly different topographies in response to tectonic uplift and climate (Phillips et al., 2004; Simms, 2004; Ryb et al., 2014a; Ott et al., 2023). In regions with lower chemical weathering than uplift, significant mechanical denudation triggers fluvial incision and steep slopes (Phillips et al., 2004; Ryb et al., 2014a). In contrast, higher chemical weathering than uplift rates result in stable hillslopes, where high dissolution rates prevent debris production (Ryb et al., 2014a). Thus, the shift from mechanical erosion to chemical weathering leads to a transition from fluvial features to karst (Phillips et al., 2004; Ryb et al., 2014a). In tectonically stable or slowly uplifting regions with humid climates, carbonate rocks form low-relief areas with flat topography, indicating the predominance of chemical weathering (Simms, 2004; Ott et al., 2023). Rapidly uplifting regions with arid climates develop high-relief areas with steep mountains and stream incisions, representing the prevalence of mechanical erosion (Ott et al., 2023). However, the Central Taurides does not fit into these patterns, as the rapidly uplifting carbonate plateau forms flat-lying karst terrains instead of fluvial drainage and steep slopes.

Precipitation gradient across the Central Taurides dictates an asymmetric denudation pattern, with fast denudation on the high plateau margin and slow denudation rates towards the plateau interior (Figures 5.7a and 5.7c). This asymmetric denudation pattern mimics the asymmetric uplift pattern across the plateau margin, as suggested by geomorphic analyses of the plateau surface (Cosentino et al., 2012; Schildgen et al., 2014). Considering the morphology of the plateau, Cosentino et al. (2012) showed

that the decrease in the topographic gradients of the northward-tilted Miocene marine sediments covering the plateau margin reflects the asymmetric uplift pattern. Therefore, these similar patterns suggest a strong coupling and feedback between precipitation, denudation, and uplift, which is comparable with coupling processes across other active mountain ranges (Willett, 1999; Whipple, 2009) and is similar to the dynamic coupling observed in carbonate terrains across the Juda Range, Israel (Ryb et al., 2015).

We also compared the outcrop denudation rates with published uplift rates. Since the integration time of ^{36}Cl-derived denudation rates for the Central Taurides spans <80 ka, we compared denudation rates with the Late Pleistocene uplift rates. Racano et al. (2020), based on mapping the remnants of platforms along the southern margin of the plateau and using terrace-evolution modeling of marine terraces, showed a significant increase in uplift rates from 1.9 to 3.5 m/ka between 500 and 200 ka, which decreased to 1.4 m/ka from 200 ka to the present. In addition, surface exposure ages (^{10}Be, ^{26}Al, and ^{21}Ne) of fluvial strath terraces with elevation between 28 and 135 m yielded an incision rate (and an inferred rock-uplift rate) of 0.52–0.67 mm/yr in the Mut Basin in the Central Taurides since ca. 130 ka (Schildgen et al., 2012). Comparing these Late Pleistocene uplift rates with our long-term ^{36}Cl-derived denudation rates indicates that despite similar spatial patterns the uplift rates are significantly higher than the mean denudation rate (13.29 ± 0.50 mm/ka) in the Central Taurides and even higher than the highest denudation rates (DEN-06: 19.00 ± 1.81 mm/ka and DEN-07: 18.70 ± 1.89 mm/ka) at the plateau margin. Therefore, in the rapidly uplifting setting of the CAP southern margin, the considerably higher uplift rates than the denudation rates reveal a transient topography not yet adjusted to the recent rapid uplift. The adjustment of denudation to uplift takes time, and the time lag between the onset of uplift and the final adjustment of summit denudation is likely to be longer for larger uplifted areas (Ahnert, 1970). Furthermore, these slow denudation rates compared to high uplift rates explain why the plateau still preserves its high elevation and probably indicate that denudation during uplift occurred primarily through subsurface karstification.

In the Mediterranean region, the reason why carbonate ranges maintain their high elevations is attributed to the high infiltration of surface water in karst areas and low surface runoff (Ott et al., 2019). In their interpretation, Ott et al. (2019) attributed the high carbonate topography to strong local uplift, where low carbonate dissolution

cannot compensate for the uplift. In the Eastern Alps (Dachstein paleosurface), high-elevation limestone plateaus have been preserved because erosion during uplift was primarily by subsurface karstification through cave formation, where decreasing runoff impeded surface erosion (Frisch et al., 2001). The Central Taurides has a well-developed, multi-store horizontal cave system that conveys groundwater southward (Nazik et al., 2019). In addition, this karst terrain, especially in Aladağlar Mountain, has a particularly efficient subsurface drainage system with a very high absorption capacity of the recharge that even the torrential rainfalls on the snow cover do not produce significant surface runoff (Bayarı et al., 2019). Thus, it appears that the preservation of the high-elevation carbonate plateaus in the Central Taurides has similar reasons as the two studies mentioned above in the Mediterranean and Eastern Alps. On the one hand, extensive subsurface karstification and, on the other hand, significant infiltration of surface water into the karst system and insignificant runoff resulted in low surface denudation and preservation of the high-elevation carbonate plateau. Indeed, the efficient drainage of runoff by karst systems inhibits the topographic response to tectonic uplift and derives the disequilibrium between uplift and denudation rates.

In the lack of efficient fluvial systems, given that the current denudation regime (low surface denudation vs. rapid uplift) remains unchanged, time alone may not be enough to limit the topographic height. Therefore, moving forward in time, it is possible that the glacial erosion known as the glacial buzzsaw (Mitchell and Montgomery, 2006; Egholm et al., 2009) will take control on the elevation of the plateau by eroding the topography near and above the snowline altitude and keeping it at the snowline.

5.2.2.3 Lithologic control

Previous studies in the Mediterranean region found that the mineralogical composition (Levenson et al., 2017) and lithology (Krklec et al., 2022) have no significant influence on the long-term denudation rate of carbonates. Moreover, in the subtropic monsoon zone in China, the ^{36}Cl-derived denudation rate of carbonate bedrocks showed no correlation with rock properties (rock type and density), suggesting limited lithological control on carbonate denudation (Xu et al., 2013). In this study, the weak correlations between carbonate denudation rates and their physical properties (mechanical strength, porosity, and water absorption by weight) suggest that the magnitude and the spatial

distribution of denudation rates are not controlled by the physical properties of bedrock.

5.2.3 Comparison of denudation rates with global records

The previously published ^{36}Cl-derived bedrock denudation rates for carbonates (n = 236) (Stone et al., 1994; Matsushi et al., 2010a; Xu et al., 2013; Ryb et al., 2014a, 2014b; Godard et al., 2016; Thomas et al., 2017, 2018; Marrero et al., 2018; Avni et al., 2019; Yang et al., 2020; Ben-Asher et al., 2021; Krklec et al., 2022) were compiled and the results of this study was compared with global data set. This compilation shows that ^{36}Cl-derived denudation rates for carbonates range from <1 to ~200 mm/ka for various bedrock samples, including flat-lying bedrocks on hilltops or plateaus, bedrocks on hillslopes, and soil-covered bedrocks (Figure 5.8a). However, most denudation rates, especially for flat-lying bedrocks on hilltops or plateaus, are limited to rates of less than 100 mm/ka. In comparison, the outcrop denudation rates in the south of the CAP, with a range of 1.92–45.77 mm/ka (mean: 14.40 ± 0.47 mm/ka, median: 12.42 ± 1.31 mm/ka), are at the lower end of the global record (Figure 5.8a). Furthermore, with the exception of DEN-01 (45.77 ± 3.91 mm/ka), which is very close to the coast, results in this study have a range of 1.92–22.35 mm/ka, which is comparable to denudation rates of flat-lying bedrocks on hilltops or interfluves in the carbonate landscapes of the Eastern (Ryb et al., 2014a, 2014b; Avni et al., 2019) and North-eastern Mediterranean (Krklec et al., 2022) (Figure 5.8a). Comparable bedrock denudation rates reported from the Eastern and North-eastern Mediterranean include (1) denudation rates with an average value of 21 ± 7 mm/ka in the Soreq drainage, Judea Hills, Israel (Ryb et al., 2014b), (2) denudation rates with a range of 1–3 to 20 mm/ka in the hyperarid to Mediterranean zone in the Judea Range, Israel (Ryb et al., 2014a), (3) denudation rates with an average rate of 19 ± 5 mm/ka in the subalpine region of Mount Hermon, Israel (Avni et al., 2019), and (4) denudation rates with a range of 14.7–22.8 mm/ka (originally reported as m/Ma) in the temperate climate of the North Dalmatian Plain, Croatia (Krklec et al., 2022).

Among the various factors that may contribute to the denudation of carbonates, precipitation is the most emphasized factor (Stone et al., 1994; Ryb et al., 2014a, 2014b; Yang et al., 2020; Ben-Asher et al., 2021). Some studies (Ryb et al., 2014a; Levenson et al., 2017; Thomas et al., 2018; Yang et al., 2020) have examined the

relationship between carbonate denudation and precipitation on a global scale. This evaluation revealed that denudation rate of carbonates in arid regions (MAP <700 mm) increases linearly with precipitation, suggesting the role of water supply as a limiting factor on carbonate denudation, while it is independent of precipitation in temperate to humid climates (MAP >700 mm) (Ryb et al., 2014a; Thomas et al., 2018; Yang et al., 2020), which was interpreted as the impact of other factors such as dissolution kinetics of carbonate minerals. The proposal that dissolution kinetics are responsible for this transition has been explored by Levenson et al. (2017) using an analog dissolution experiment, which suggested that the kinetic limit is much higher than ~100 mm/yr. De Waele and Gutiérrez (2022) pointed out that the observed decoupling between denudation and precipitation in humid regions cannot be related to the kinetics of dissolution since the rainfall that reaches the earth's surface is undersaturated regarding carbonate minerals. They suggest it might be related to the fact that previous studies cover a limited precipitation range with most values below 1500 mm, the diverse properties of sampling sites (e.g., lithology and vegetation), the various rates of mechanical erosion, and the assumption of constant denudation.

Following this attempt, more recent studies and the results of this study were added to the previous data set to evaluate the denudation precipitation relationship (Figure 5.8b). The resulted denudation rates in this study, with a precipitation range of ~400–770 mm, fit into the first part of this plot and confirm the increase in denudation rates with increasing precipitation in arid regions. Moreover, putting soil-covered and hillslope samples aside, it seems that the dependency of denudation rates on MAP breaks at MAP of ~1000 mm/ yr (rather than 700 mm/yr). Other variables, such as temperature or the physical properties of carbonates, have been explored in a series of previous studies and this study, in flat-lying, unglaciated carbonate landforms with MAP range of 0–1000 mm/yr, showing that they have secondary effects over denudation, while precipitation appears to be the dominant factor.

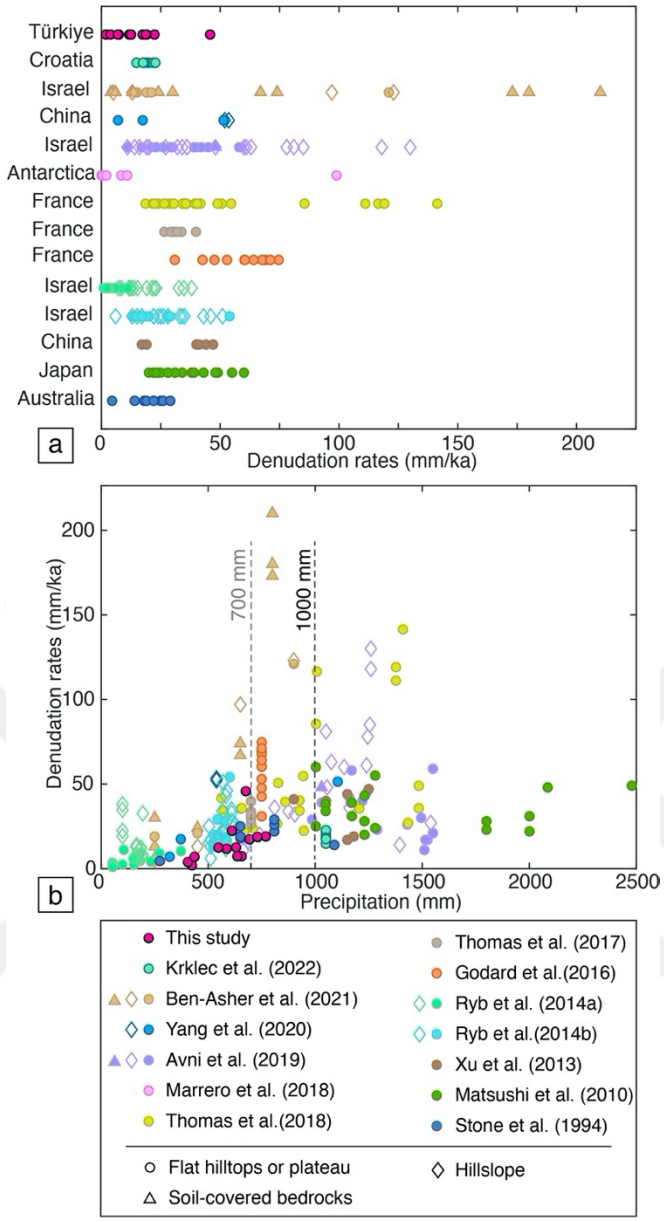

Figure 5. 8 : (a) Denudation rate of carbonate bedrocks for all previous studies. (b) Denudation as a function of mean annual precipitation for all previous studies. The study of Marrero et al. (2018) was excluded from the precipitation graph because of uncertainty in precipitation data in Antarctica, as mentioned by the authors. This figure wass taken from Hashemi et al. (2023).

6. THE NAMARAS RACK AVALANCHE: A MID-TO-LATE HOLOCENE PARAGLACIAL ACTIVITY IN THE CENTRAL TAURIDES

This chapter includes two sections. The first section presents the surface exposure age of the rock avalanche and its geomorphological results. The second section discusses the preconditioning, preparatory, and triggering factors that caused the rock avalanche failure.

6.1 Results

6.1.1 Geomorphology of the Namaras rock avalanche (NRA)

The NRA, with an aspect to the NE and a total area of ~0.430 km^2, is situated in the northern flank of the Geyikdağ Mountain (Figure 6.1a and 6.1b). The rock avalanche has occurred in the Jurassic-Cretaceous bedded neritic limestone, with the bedding plane dipping ~65° to the SW. The bedrock is highly fractured with cross-joints and vertical joints on it (Figure 6.3a). The source area is a glacial cirque headwall with a 75–85° dip towards NE. We produced a slope map (Figure 6.2) for the rock avalanche and the surrounding area to identify the source area boundaries. We assumed the whole cirque area had been the rock avalanche source area with an area around 25.9×10^3 m^2. The crown of the source area on the upper edge of the cliff is at 2700 m asl, and the boulders which have been released from there travelled ~200 m vertical distance before hitting the ground at the base of the cliff (Figures 6.1a and 6.1b). The average slope of the travel path is 25–30°, and its length to the beginning of the rock avalanche deposit is ~600 m.

The NRA has a fan-shaped deposit that overlies a lateral moraine and the hummocky moraine field down in the Namaras Valley (Figures 6.1b and 6.3b). The position of the lateral moraine has forced the rock avalanche to be divided into right and left lobes (Figure 6.3b). The rock avalanche deposit terminus on both lobes has a distinct and sharp boundary with moraine sediments that could be easily distinguished on the ortho (Figure 6.4a) and aerial photos. Additionally, the rock avalanche deposit terminus

makes an abrupt topographic height on top of the hummocky moraine in the field. The rock avalanche deposit runs up on the opposite slope of the lateral moraine with an approximate run-up height of ~30 m (Figure 6.3c).

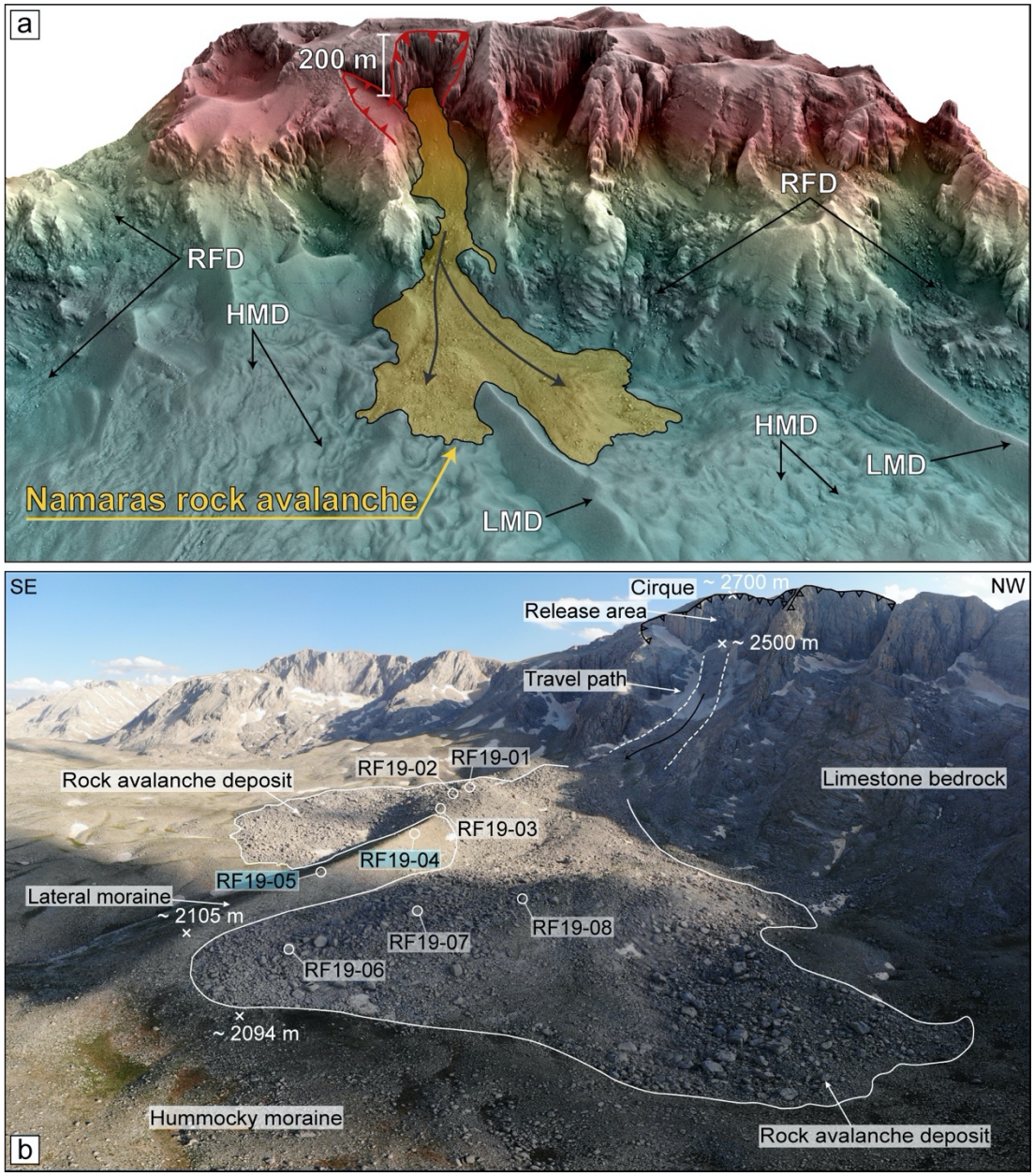

Figure 6. 1 : (a) 3D view of the Namaras rock avalanche. RFD: rock fall debris, HMD: hummocky moraine debris, LMD: lateral moraine debris (b) Overall view of the Namaras rock avalanche indicating release area, travel path and deposit area. Sampling sites are marked on the photo: The blue and white colors indicate the location of the sampled boulders of the lateral moraine and the rock avalanche deposit, respectively. This figure was taken from Hashemi et al. (2022).

The rock avalanche deposit mainly comprises large boulders in fragmented rock sediment, devoid of vegetation and soil development (Figure 6.3c). The size of the boulders varies from less than 1 m to >15 m in diameter (Figures 6.4a and 6.4b). The

blocks are generally equant in shape with an average diameter of ~4 m, with some house-sized huge blocks reaching up to 22 m in diameter. In situ investigation of rock avalanche blocks indicates that fragmentation occurred in the first impact of the boulders with cliff base and on their travel path before their final settlement in the accumulation zone.

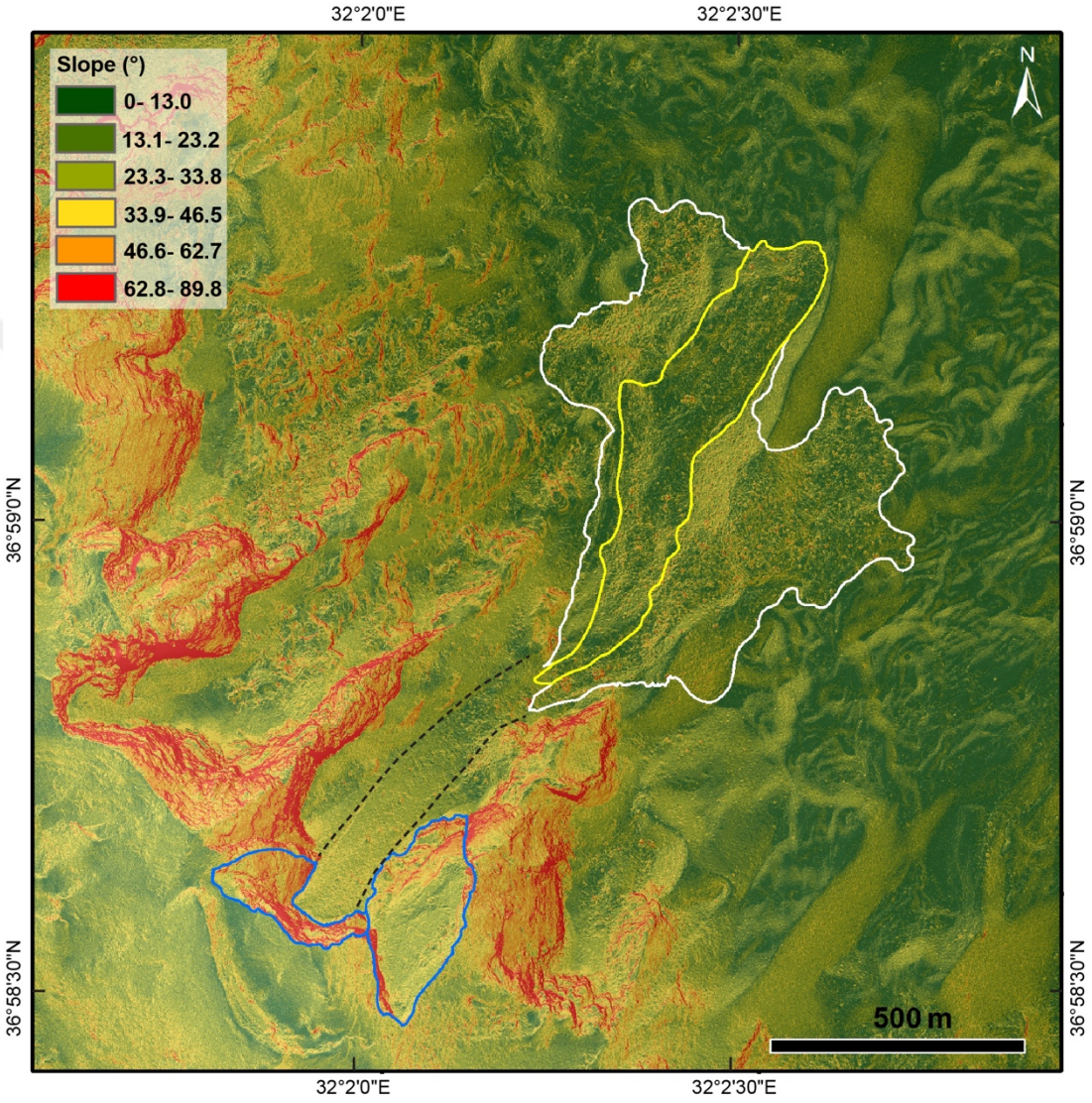

Figure 6. 2 : Slope map of the Namaras rock avalanche and the surrounding area. Blue, white and yellow colors delineate the source area of the rock avalanche, older event deposit and younger event deposit, respectively. The black dashed line shows the travel path of the rock avalanche. This figure was taken from Hashemi et al. (2022).

Fieldwork and aerial photo interpretation are usually the primary sources for the geomorphological assessment of rock avalanche runouts (Hungr et al., 2005). The field and aerial photo investigation show that the NRA consisted of more than one rock avalanche event (Figure 6.5). The color differences on the orthophoto (Figure 6.4a), the block sizes and distributions (Figures 6.4b, 6.4c and 6.4d) and the deposit thickness

variation were considered to separate possible events. It appears that flow-like debris with a narrow width overlies the left lobe of the previously settled deposit and extends parallel to the lateral moraine (Figure 6.5). Since this deposit covers the underlying units, it assumed that it is a younger event. This younger deposit is recognizable by its different and lighter color on the orthophoto (Figure 6.4a). The distribution of block sizes and numbers for the two events is different. The provided “block density” map (Figure 6.4c) shows the number of blocks per unit area regardless of their size, while the “block area density” map (Figure 6.4d) indicates the distribution of boulder sizes per unit area. For the older deposit, the right lobe has a greater thickness (Figure 6.6a, S2) with densely distributed blocks (Figure 6.4c), and the left lobe has a lesser thickness (Figure 6.6a, S2) with a sparse block distribution. The superimposed flow-like younger debris has a lesser thickness (Figure 6.6a, S2) with a sparse spread of the blocks in the middle part (Figure 6.4b and 6.4c), and a greater thickness (Figure 6.6a, S1) with a dense spread of blocks in the distal part of the accumulation zone (Figure 6.4b and 6.4c). In addition, the older deposit has numerous massive blocks distributed over the whole accumulation zone, especially on the right lobe (Figure 6.4d). In comparison, the younger debris consists mainly of smaller blocks in the upper part of the accumulation zone, while the large boulders mostly stopped within the middle and lower part of the accumulation zone (Figure 6.4d). The boulders of the younger event are semiburied in a muddy-looking matrix of washed and hardened limestone. This evidence led to hypothesize that at least two rock avalanche events have occurred; (1) the first high-magnitude main rock avalanche consisting of two lobes, (2) followed by a lower magnitude event that partially covered the left lobe of the earlier event, laying parallel to the lateral moraine (Figure 6.5).

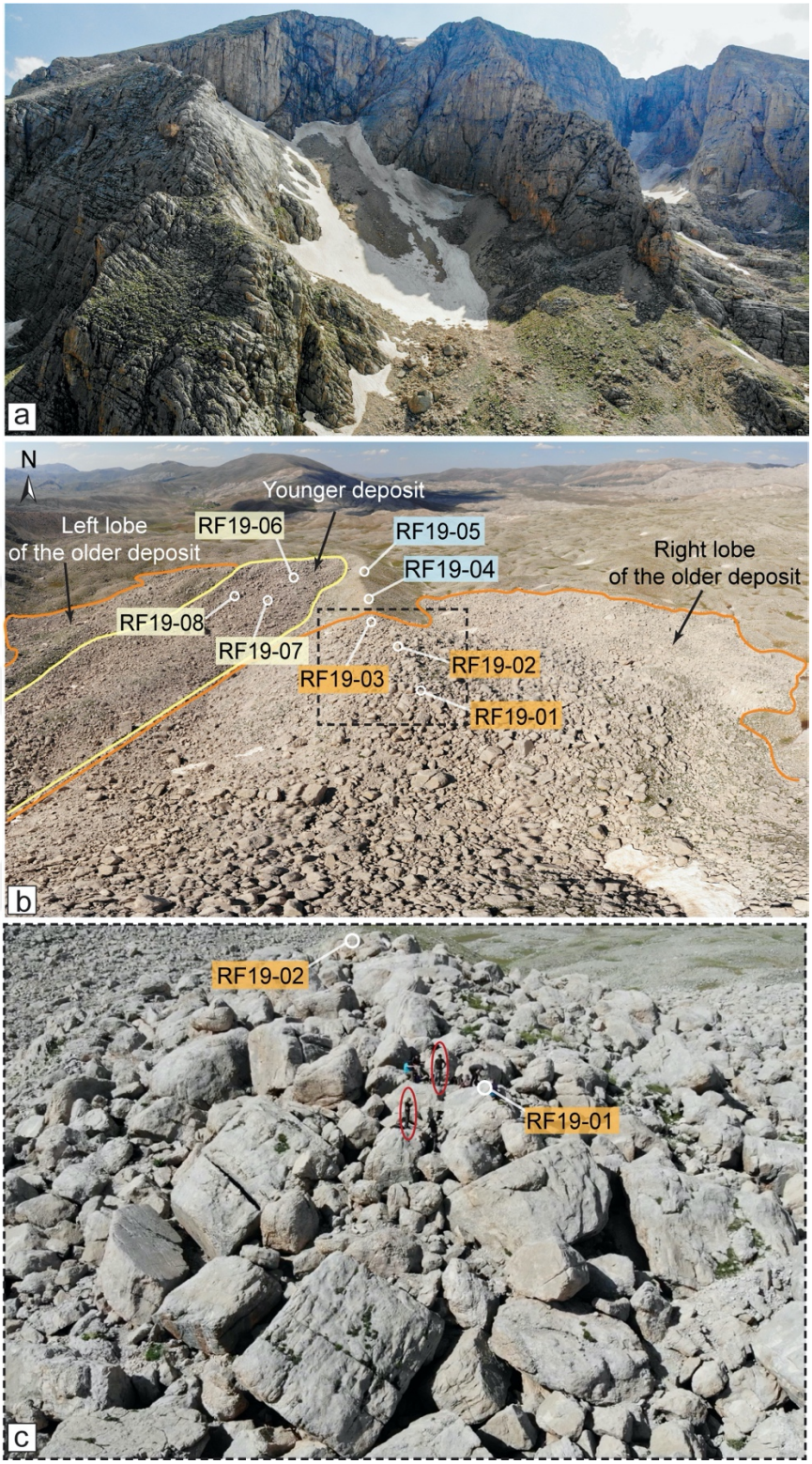

Figure 6. 3 : (a) A close view of the source area with the bedded limestone and joints on it. (b) A view towards the north from the NRA deposit. The orange and yellow lines delineate the boundary of the older and younger rock avalanche deposits, respectively. Sampling sites with blue, orange and yellow colors belong to moraine, older, and younger deposit boulders, respectively. (c) A close view of the black dashed box in (b). The red ovals show two people for scale. This photo shows huge boulders of the rock avalanche with 30-m run-up over the lateral moraine on the opposite side. This figure was taken from Hashemi et al. (2022).

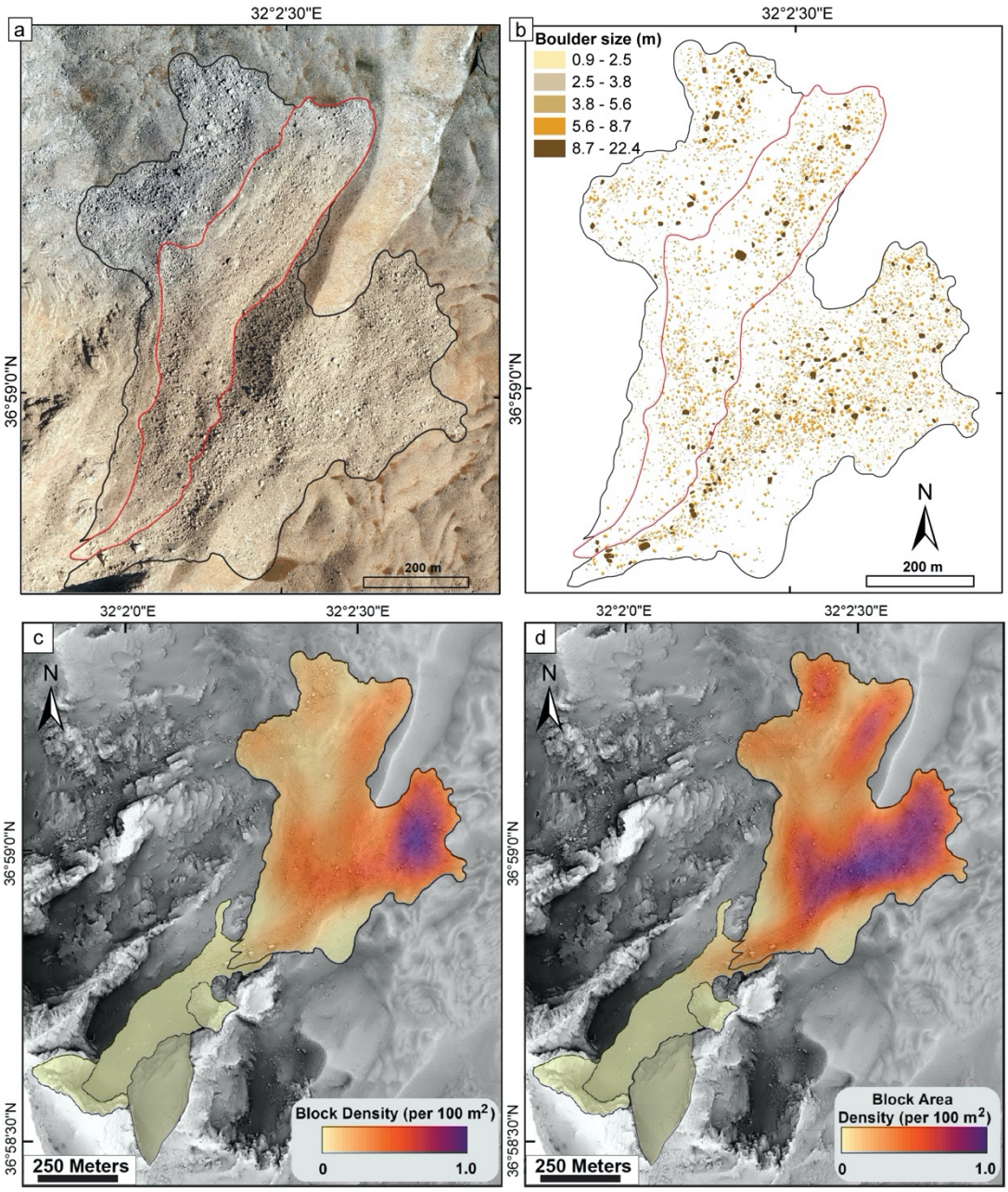

Figure 6. 4 : (a) Orthophoto with a resolution of 19-cm produced from high resolution aerial photos. The red color delineates the younger deposit. (b) The boulder size map of the rock avalanche deposit extracted from 19-cm resolution orthophoto. Darker and lighter colors indicate longer and shorter boulder lengths, respectively. (c) The rock avalanche block density distribution per 100 m^2. (d) This figure shows the block area density per 100 m^2. This figure was taken from Hashemi et al. (2022).

The geomorphological map (Figure 6.5) and longitudinal profiles (Figure 6.6b) were used to determine the geometric parameters of each event. The first rock avalanche event with an area of 0.415 km^2 has the maximum horizontal runout distance of 1550 m. The measured 600 m elevation loss for 1550 m horizontal runout distance yielded a travel angle of 21° (A–B profile, Figure 6.6b). In comparison, the second rock

avalanche event has a small area of ~0.127 km^2, with a maximum 1720 m runout distance. The measured runout distance and 640 m vertical elevation loss resulted in the 20° travel angle for the younger event (C–D profile, Figure 6.6b). The travel angle (Cruden and Varnes, 1996; Copons et al., 2009) is the angle of a line connecting the highest point of the landslide crown to the toe of the deposited mass. It is suggested that the travel angle is the equivalent coefficient of friction (Shreve, 1968), and there is an inverse relationship between this angle and the volume of deposit, with lower travel angles resulting in higher deposit volume and vice versa (Scheidegger, 1973). For both events of the NRA, the calculated travel angles agree with travel angles achieved in other recently investigated carbonate rock avalanches in the Bernese (Grämiger et al., 2016) and the Glarner Alps in Switzerland (Nagelisen et al., 2015).

Field investigation shows that the right lobe of the older deposit has a greater thickness than the left lobe (also recognizable in the across deposit topographic sections, Figure 6.6a). Based on the elevation difference between slope surfaces of the lateral moraine crest (with 4° dip) and rock avalanche deposit, the thickness of the right lobe of the older deposit, which blankets the lateral moraine, was estimated to be ~20 m (Profile E–F, Figure 6.6b). It appears that this 20 m thickness is the maximum thickness of the rock avalanche deposit. The field observation shows that the older debris thickness decreases to ~5 m towards the toe of the deposit. The deposit of the younger event is sparse in the upper part of the accumulation zone, while its thickness increases towards the toe. Thus, a 5 m thickness for the upper part of the younger deposit has been estimated which increases to ~10 m towards deposit terminus. However, the exact values of deposit thicknesses are unknown, and the estimations in this study are based on the field observation, the longitudinal profile (E–F), and variations in the topographic contour lines.

An empirical method (area times the average thickness) was used to estimate the total volume of the NRA. By assuming an average thickness of 10 m, a total volume of 4.3 million m^3 for the NRA was obtained. Because of the overlapping of the two events, it is difficult to assess each rock avalanche's volume. Based on Hungr et al. (2014) definition, we classified this RSF as a rock avalanche because of its relatively large volume, and massive blocks in a fragmented matrix towards the depth of the deposit.

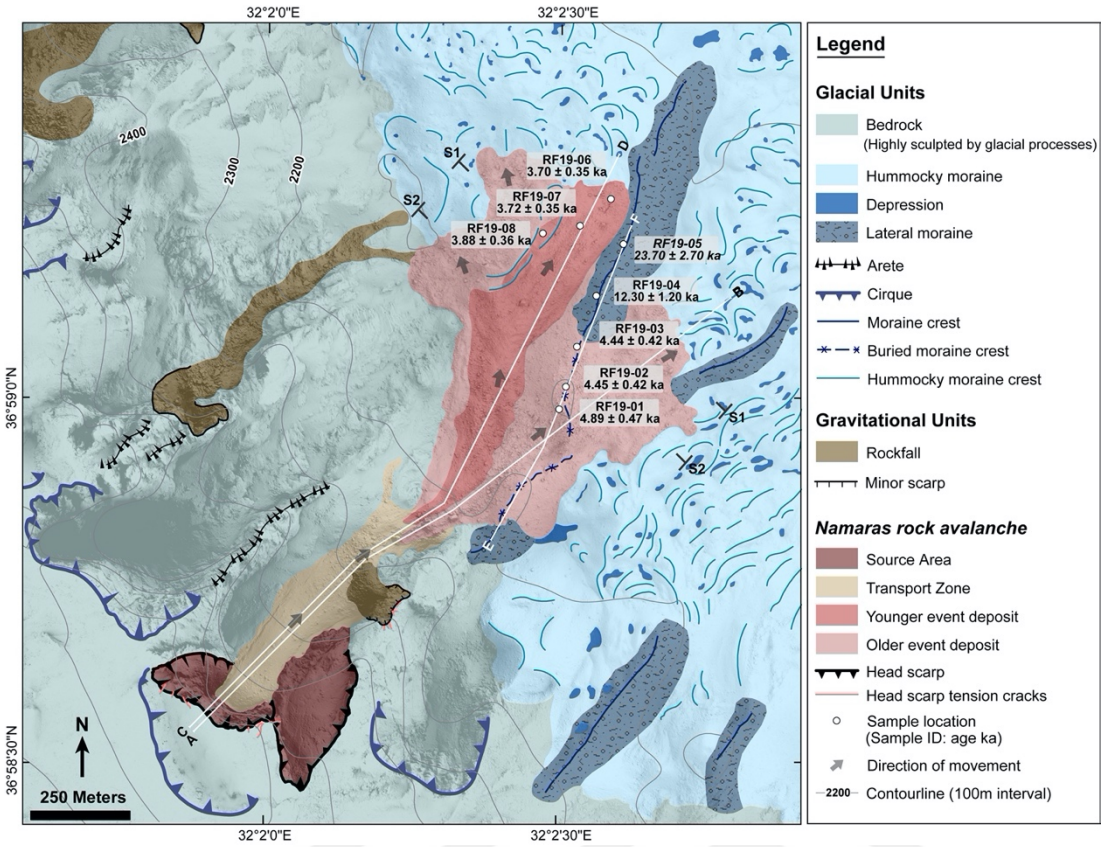

Figure 6. 5 : Geomorphological map of the Namaras rock avalanche. S1 and S2 indicate traces of two across deposit topographic sections (Figure 6.6a). White lines (A–B, C–D, E–F) show traces of longitudinal profiles presented in Figure 6.6b. The outlier moraine sample is indicated in italic font. This figure was taken from Hashemi et al. (2022).

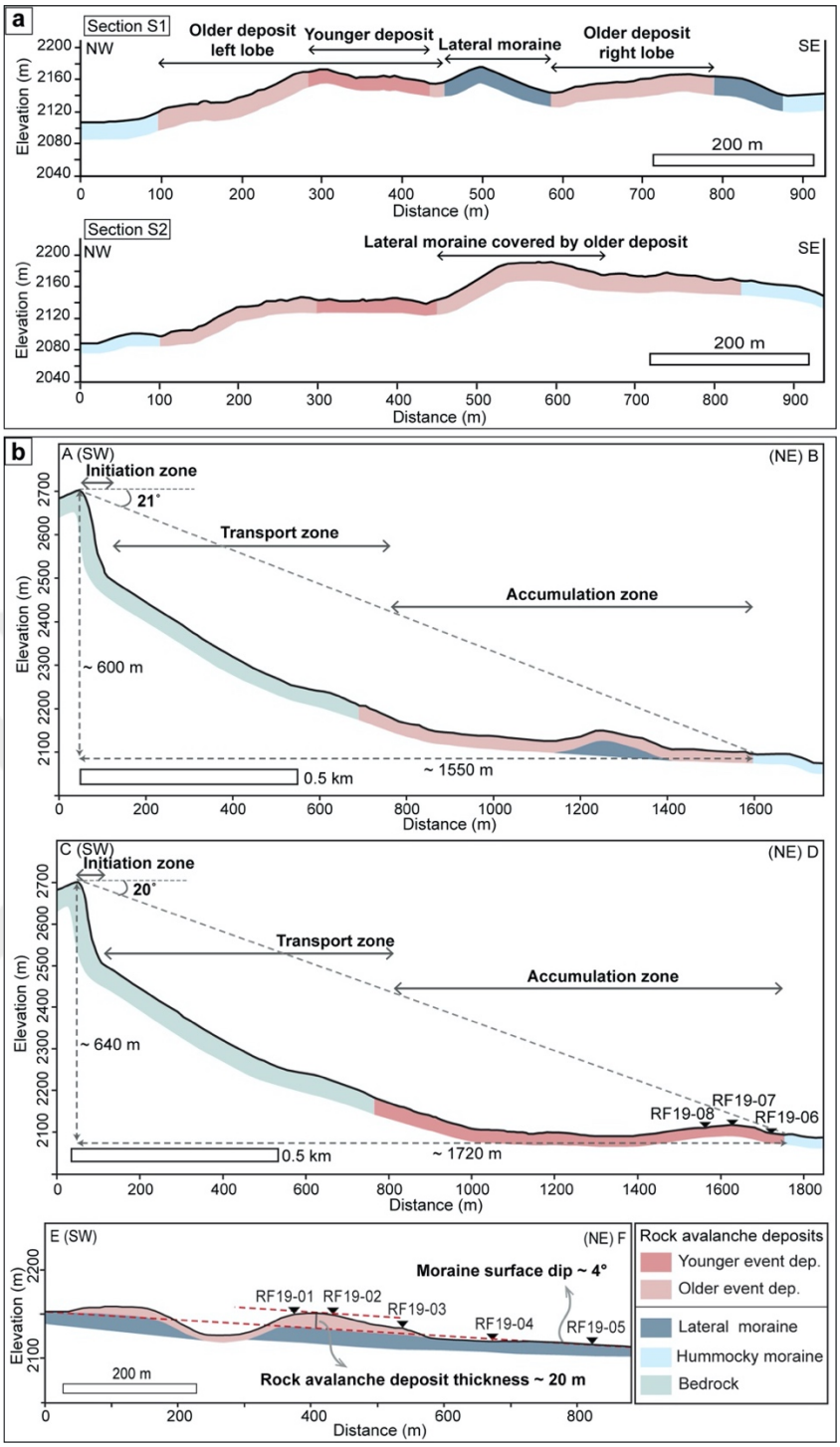

Figure 6. 6 : (a) Two across deposit topographic sections (S1 and S2). (b) Three longitudinal profiles along the runout path. The location of sections and the longitudinal profiles are shown on the geomorphological map (Figure 6.5). A–B, C–D and E–F are longitudinal profiles along the older rock avalanche deposit, the younger rock avalanche deposit and the older deposit and lateral moraine, respectively. Sampling sites are projected on the profiles C–D and E–F. Profile E-F shows deposit run-up over the lateral moraine. Different colors taken from the geomorphological map represent the bedrock outcrop, surface extension of each deposit, and moraines. The color thicknesses are not representative of the deposit thicknesses. Vertical and horizontal scales are equal (V = H). This figure was taken from Hashemi et al. (2022).

6.1.2 Cosmogenic ^{36}Cl exposure dating results

Eight ^{36}Cl samples were collected from the rock avalanche and the lateral moraine. The boulder ages were calculated with and without erosion (Table 6.1). 10 mm/ka erosion increases the rock avalanche boulder ages ~1–3%, while the age of moraine boulders shows ~11–14% increase with erosion. Although erosion correction has a minor impact on the rock avalanche boulder ages (1–3% increase), erosion corrected ages were preferred. The age results are reported in one standard deviation uncertainty, which includes both analytical and production rate errors.

Table 6. 1 : Surface exposure ages of rock avalanche and moraine boulders.

Sample ID	Landform	Cl	^{36}Cl × 10^5	σ ^{36}Cl × 10^4	Surface Exposure Ages		Event/Landfom Age
					No erosion	Erosion corrected	
		ppm	(atoms g^{-1} rock)		(ka)	(ka)	(ka)
RF19-01	Older RA.D.	12.7 ± 1.5	4.569	2.888	4.74 ± 0.44	4.89 ± 0.47	
RF19-02	Older RA.D.	11.7 ± 0.9	4.206	2.558	4.30 ± 0.40	4.45 ± 0.42	4.59 ± 0.25
RF19-03	Older RA.D.	14.0 ± 1.0	4.134	2.499	4.31 ± 0.39	4.44 ± 0.42	
RF19-06	Younger RA. D.	16.5 ± 1.0	3.45	2.181	3.62 ± 0.34	3.70 ± 0.35	
RF19-07	Younger RA. D.	8.8 ± 0.5	3.476	2.124	3.63 ± 0.33	3.72 ± 0.35	3.77 ± 0.20
RF19-08	Younger RA. D.	21.1 ± 1.4	3.660	2.159	3.81 ± 0.34	3.88 ± 0.36	
RF19-04	Lateral Moraine	12.1 ± 0.9	1.077	6.169	11.00 ± 1.00	12.30 ± 1.20	18.00 ± 1.48
RF19-05	Lateral Moraine	23.3 ± 1.9	1.983	11.650	20.70 ± 1.90	23.70 ± 2.70	Outlier

RA.D. (rock avalanche deposit), Erosion correction (10 mm ka^{-1})

The resulted rock avalanche boulder ages range from 4.89 ± 0.47 ka to 3.70 ± 0.35 ka (Figures 6.5 and 6.7). The percentages of production pathways are dominated by Ca spallation (%95–97) while contributions of K spallation and thermal neutron capture by ^{35}Cl pathways are respectively less than 1% and between 4.5 and 1.8% for all samples. Moraine samples, RF19-04 and RF19-05, yielded much older ages than rock avalanche boulders; 12.30 ± 1.20 ka and 23.70 ± 2.70 ka, respectively (Figures 6.5 and 6.8). The distribution of rock avalanche boulder ages suggests that there is negligible inheritance on the samples. This could be due to the deep pre-failure boulder depth in the source area unaffected by pre-failure exposure (Hilger et al., 2019). It appears that the boulders from the shallow pre-failure surface in the source area settled at the bottom of the rock avalanche deposit and superimposed by the boulders from the depth of the source area, which were not affected by pre-failure exposure. The probability density distribution function (Camel plot approach, Balco, 2011) of ages showed that rock avalanche boulders resulting in two age clusters (Figure 6.9); one with a weighted

average age of 4.59 ± 0.25 ka (1σ) and the other one with a weighted average age of 3.77 ± 0.20 ka (1σ). In the case of moraine sample ages, the sample RF19–05 (23.70 ± 2.70 ka) was considered as an outlier due to inheritance. A previous study conducted by (Çiner et al., 2015b) dated three lateral moraines parallel to dated lateral moraine in this study in the Namaras Valley with weighted ages of 13.6 ± 2.7 ka (~1.2 km west), 14.0 ± 2.7 ka (~2 km west) and 13.4 ± 1.5 (~3.7 km east), respectively. Since the younger moraine age in this study is consistent with the moraine ages in the area, it was assumed the age of the lateral moraine is approximately 12.30 ± 1.20 ka based on the sample RF19–04. Although a reliable timing for the moraine could not be established due to the inheritance impact on one of moraine samples, consistency of the younger moraine age with other previously dated moraines close to the dated moraine in this study shows this moraine is significantly older than the rock avalanche, demonstrating the latency in the RSF occurrence. Collectively, according to the geomorphic assessment and provided camel plot of six boulder surface exposure ages, we defined two events for the NRA. These age results confirmed two successive paraglacial rock avalanche events with weighted average ages of 4.59 ± 0.25 ka and 3.77 ± 0.20 ka during mid-to-late Holocene. The age results indicate that the older and younger events occurred roughly ~7.7 ka and 8.5 ka after deglaciation.

Furthermore, the cosmogenic samples were not collected from the left lobe of the rock avalanche, which is partially covered by the younger rock avalanche. This part could belong to the first event and have the same age as the right lobe or could be independent. In the absence of quantitative age data from this part, and based solely on the geomorphologic evidence, it was assumed that this part belongs to the first event.

Figure 6. 7 : Photo plate of sampled rock avalanche boulders. Three photos in the top row belong to the older deposit. Three photos in the bottom row are from the younger rock avalanche deposit. The location of sampling sites is shown on the field photos (Figures 6.1b and 6.3b) and the geomorphological map (Figure 6.5). This figure was taken from Hashemi et al. (2022).

Figure 6. 8 : The two sampled moraine boulders which are located on the lateral moraine crest. This figure was taken from Hashemi et al. (2022).

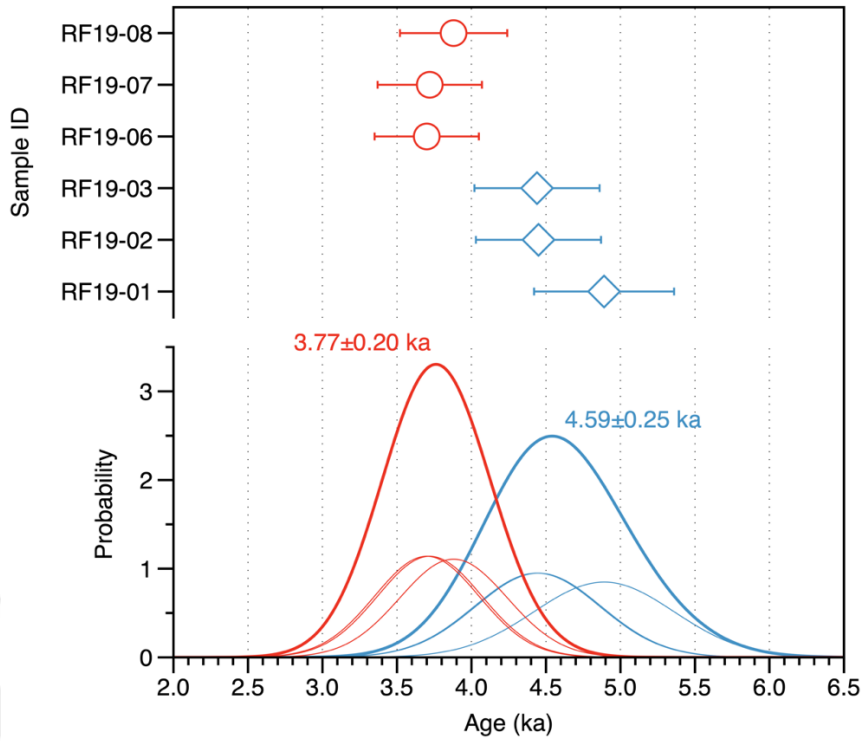

Figure 6. 9 : The probability density function of rock avalanche boulders showing two age clusters. The ages are reported in one sigma uncertainty. This figure was taken from Hashemi et al. (2022).

6.2 Discussion

6.2.1 Preconditioning, preparatory and triggering factors

The parameters that contribute to slope failure are classified into three groups based on their nature; preconditioning, preparatory, and triggering factors (Gunzburger et al., 2005; McColl, 2012; Grämiger et al., 2018). Preconditioning factors are internal factors (Curry, 2021), inherent (McColl, 2012), and independent of time (e.g., lithology, structure, discontinuities, and topography). Preparatory and triggering factors are both external parameters (Curry, 2021) dependent on time (McColl, 2012; Grämiger et al., 2018). Preparatory factors such as glacial and fluvial erosion, chemical and physical weathering, and longterm seismic damage decrease the slope stability in the long time. Triggering factors, on the other hand, act in the short-term and cause the final slope failure. Earthquakes and extreme climatic events such as high precipitation and high temperatures are well-known triggers (McColl, 2012). However, RSF can also occur in the absence of triggers due to progressive destruction of rock mass to the point of loss of coherence (Eberhardt et al., 2004). Hence, in any RSF study, it is essential to assess the role of each of these components in the failure mechanism.

The bedrock in the Geyikdağ Mountain is a medium to thick-bedded limestone with the bedding plane dipping ~65° towards the SW in the opposite direction of the source rock wall slope face. Although the bedding planes dipping in the opposite direction of the slope face are known to be more resistant to failure than the layers with the identical dip direction with the slope face, they can still make the roof for the potential falling blocks (Dorren et al., 2004), making the bedrock susceptible to failure. Moreover, cross-joints and evidence of solution on the limestone bedrock were observed (Figure 6.3a). Thus, the combination of bedding plane, cross-joints, fractures, and solution grooves in limestone which may have facilitated the separation of the rock blocks in the source area can be evaluated as the preconditioning factors for the NRA.

The glacial erosion and karstification appear to be the two significant preparatory factors that contributed to the occurrence of the NRA. The steep slopes of previously glaciated mountains can be the source of successive rock slope failures (Hungr et al., 2005), as it occurred in the Geyikdağ Mountain. The two dated mid-to-late Holocene consecutive events in the NRA have a long lag-time, nearly about 7.7 ka and 8.5 ka after deglaciation. In paraglacial contexts, such a long lag-time between deglaciation and the RSF implies that glacial processes acted as a preparatory factor (Ballantyne, 2002; McColl, 2012). Indeed, the glacial erosion conditioned the slopes for failing by steepening the slopes and undercutting the rock walls without immediately triggering the failure. This pronounced time lag also suggests that debuttressing acted as a preparatory factor because in order to accept debuttressing as a trigger, glacial withdrawal and the rock slope failure should be coeval or at least should have a close temporal correlation (McColl, 2012; Nagelisen et al., 2015). Previous studies reported similar long lag-times from the Holocene paraglacial RSFs of the European Alps (Nagelisen et al., 2015; Grämiger et al., 2016; Köpfli et al., 2018), considering glacial erosion as a preparatory factor. Moreover, cryogenic processes such as cryogenic rock fracturing as well as paraglacial processes are other factors that have weakened the slope stability in the long term. Another plausible preparatory factor for the NRA is karstification and carbonate dissolution. Dissolution of carbonate rocks through chemical weathering could increase water infiltration and pore water pressure (Krautblatter et al., 2012). In addition to these factors, freezing and thawing could be considered as a preparatory factor that weakened the bedrock strength by expanding fractures and opening joints in a prolonged time frame.

The two successive events in the NRA have likely been triggered by climatic forcing. It has been shown that climatic parameters such as total precipitation, rainfall intensity, air temperature, and wind speed and duration can primarily control slope stability conditions (Crozier, 2010; Gariano and Guzzetti, 2016). Paleoclimatic records show a three millennia transition period (6–3 ka BP) between the wetter early Holocene and the drier late Holocene in the Eastern Mediterranean (Roberts et al., 2011; Dean et al., 2015) (Figure 6.10). This mid-to-late Holocene transition consists of wet-to-dry oscillations, with three phases of highest aridity at 5.3–5.0 ka BP, 4.5–3.9 ka BP, and 3.1–2.8 ka BP (Roberts et al., 2011). Furthermore, a paleoclimatic study from the Lake Gölhisar (Western Taurides, ~217 km west of the NRA) demonstrates increased values of magnetic susceptibility (and hence probable erosion) and increased sediment accumulation rates at 6.0–3.3 ka BP, implying some sort of landscape disturbance (Eastwood et al., 1999). It has been indicated that the high sedimentation rates in a time period could be in accordance with significant landslide activity in that region (Borgatti and Soldati, 2010). Therefore, the synchronicity between the high sedimentation rate in the Western Taurides and the occurrence of NRA could be related to one identical climatic factor in the study area. The $\delta^{18}O$ values from the Lake Gölhisar (Figure 6.10) show several sharp peaks of high isotope values and pollen reductions at 5.2–3.7 ka BP (Eastwood et al., 2007), implying drier climatic conditions. The severe drought period known as the "4.2 ka BP event" is reported from different locations in the Eastern Mediterranean with a duration between 4.2 and 3.9 ka BP (Weiss et al., 1993; Eastwood et al., 1999; Staubwasser and Weiss, 2006; Eastwood et al., 2007; Roberts et al., 2011; Dean et al., 2015; Ön et al., 2021). This aridity and low humidity period in the mid- Holocene were associated with torrential rainfall events and concurrently enhanced flood peaks, which is recorded in the geomorphodynamics from the Eastern Taurides (Nykamp et al., 2020) and in other regions in Anatolia (Kuzucuoğlu et al., 2004; Finné et al., 2019). This heavy rainfall pattern is in good agreement with increased sediment dynamics due to rainfall in other regions in the Eastern Mediterranean (Dusar et al., 2011). Later, in the early-late Holocene, the climate has been unstable, characterized by fluctuations of dry and wet climate between 3.9 and 3.0 ka BP for the Central Anatolia (Kuzucuoğlu et al., 2011) and between 3.6 and 2.8 cal. ka BP for other places in the Eastern Mediterranean (Avnaim-Katav et al., 2019). The number of records of mid-Holocene temperature reconstructions in the vicinity of the study area is limited. Finné et al. (2011) noted

that it is difficult to draw general conclusions about the spatial pattern of temperature variations in the eastern Mediterranean due to the lack of consistency among the various paleoclimatic records. However, some evidence of warm conditions has been reported from the Aegean Sea, which is in close proximity to our study area. An analysis of sediment cores (~350 km west of the NRA) revealed evidence of a distinct warm phase (maximum up to ~25 °C) in the south-eastern Aegean Sea between 5.4 and 4.3 ka BP (Triantaphyllou et al., 2009). In addition, a major perturbation in the sedimentation and geochemistry records of a Mediterranean temporary pond in the south-eastern Aegean Sea (~700 km west of the NRA) characterized the driest and warmest climatic conditions in the mid-Holocene (~4.7 ka BP) (Styllas et al., 2018). Usually, long-term dry and warm periods are accompanied by intense rainfall events, a well-known trigger of rock slope failures (McColl, 2012; Gariano and Guzzetti, 2016). Generally, warm temperatures act as a trigger when they are associated with other climatic parameters, and their direct role as a trigger of a RSF is not completely confirmed. In a study in the Swiss Alps, Allen and Huggel (2013) found out that although the occurrence of rock falls increases during extremely extended warm temperatures, it is, in fact, the combination of warm days and other climatic factors such as snow and ice, which leads to the slope instability. Overall, according to the paleoclimatic records of mid-to-late Holocene in the Taurides and Anatolia, it can be suggested that the two events of the NRA have had climatic triggers. The first event (4.59 ± 0.25 ka) which is synchronous with severe drought period of mid-Holocene, has been triggered under the influence of both warm temperatures and torrential rainfalls, while the second event (3.77 ± 0.20 ka) could more likely be triggered by the extended period of high precipitation at 3.7 ka BP, recorded by low $\delta^{18}O$ values at the Lake Gölhisar (Eastwood et al., 2007) (Figure 6.10). Borgatti and Soldati (2010) point out that variations in the temporal distribution of temperature and rainfall will lead to changes in the hydrological balance of slopes that affect the type and magnitude of RSFs. In addition, it has been suggested that prolonged periods of wetness could trigger reactivation of RSFs (Borgatti and Soldati, 2010), as was the case in the NRA second event. Intense rainfall could trigger the rock avalanche by increasing pore-water pressure in the rock wall and reducing effective normal stresses and shear strength (McColl, 2012; Gariano and Guzzetti, 2016). However, because of the limited available paleoclimatic data and age uncertainties, the inferred relationship between

each rock avalanche event and a certain paleoclimatic event should be regarded cautiously.

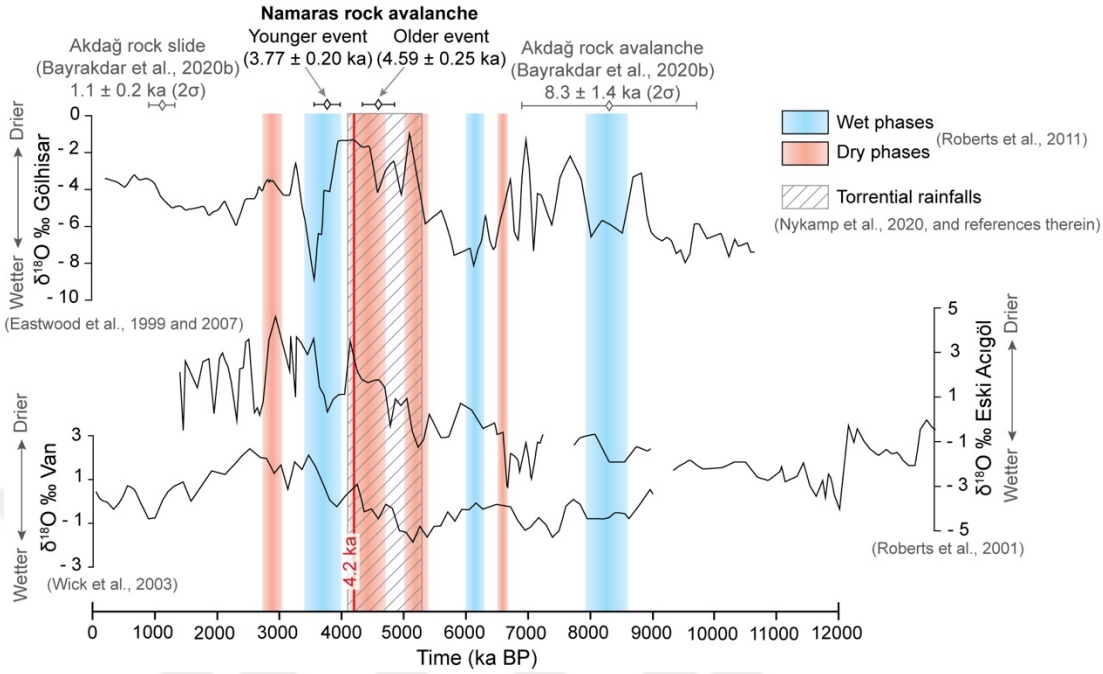

Figure 6. 10 : Timing of the Namaras rock avalanche concerning the paleoclimatic variations recorded in central and south Türkiye. This figure was modified from Fig. 5 of Dean et al. (2015) and Fig. 2 of Roberts et al. (2011), with some data added from other sources mentioned on the figure. This figure was taken from Hashemi et al. (2022).

Freeze thaw effectiveness in an area depends on the availability of two climatic conditions. The first one is significant moisture availability, and the second one frequent fluctuations of temperature to sub-zero temperatures (Gunzburger et al., 2005; McColl, 2012). It seems that the arid climate of mid-Holocene in the Taurides could not fulfil the two aforementioned criteria, the high moisture and sub-zero temperature, which are necessary for freeze-thaw phenomena to act as a trigger.

Furthermore, the possibility of a seismic activity as a triggering factor was considered. The Central Taurides could be considered as a region with low seismicity. Based on the active faults map of Türkiye (Emre et al., 2018), there is no distinguished active fault in the vicinity of the NRA. The historical earthquake catalogue of Türkiye (Tan et al., 2008), from 2100 B.C. to 1963 A.D., indicates four recorded earthquakes in the surrounding area (two ~30 km to the NE, and another two respectively ~16 km and ~25 km away to the SE). However, the modern earthquake catalogue for 1900–2012 (Kadirioğlu et al., 2018) shows no earthquake of medium to high magnitude in the vicinity of the NRA. Only a few earthquakes with moderate to low magnitude (M 4.0–

4.9) were reported several kilometres away from the NRA. However, even though the modern seismicity is low, due to the lack of paleoseismic studies on the nearby faults or from the neighboring lacustrine records, the possibility of a seismic trigger cannot be completely excluded. Last but not least, NRA may have occurred without a specific trigger, because of progressive strength loss and long-term static fatigue.

6.2.2 The comparison of the NRA with other mid-Holocene RSFs

Several previous studies have reported the temporal clustering of mid-Holocene RSFs in the Alps (Soldati et al., 2004; Prager et al., 2008; Borgatti and Soldati, 2010; Zerathe et al., 2014; Ivy-Ochs et al., 2017) and the outer-Alpine regions in Europe (e.g., Curry, 2021). While early Holocene RSFs were primarily associated with glacial debuttressing, mid-to-late Holocene events were generally attributed to climate variability or seismic events. Although the reconstruction of RSF inventories in different mountain ranges has been studied, less attention has been paid to the comparison and cross-correlation of these inventories with other mountain ranges. Such a comparison will help identify the geographic pattern of RSF spatial distribution in the mid-Holocene and understand what may have caused prehistoric RSFs at larger geographic scales.

The NRA was cross-correlated with the climatically driven paraglacial RSFs of the mid-Holocene in the Alps (between 5 and 3 ka). Although geographically distant, the NRA appears to share two common features with some temporally synchronous RSFs in the Alps: a long delay after the glacial retreat and a climatic trigger. The main NRA event (4.59 ± 0.25) with its long lag time (~7.7 ka) is temporarily comparable to the Molveno rock avalanche (4.8 ± 0.5 ka age, Italy, von Wartburg et al., 2020) with ~12 ka lag time, the Platten rock avalanche (6.1 ± 0.8 ka age, Switzerland, Nagelisen et al., 2015) with ~10 ka lag time, and Eibsee and Fernpass rock slides (4.1 ± 0.6 ka and 4.1 ± 0.1 ka ages, respectively, Austria, Prager et al., 2008) with significant lag times (likely ~8 ka). Furthermore, most major Holocene landslides in the Alps occurred at least 6000 years after glacial retreat, with some in the recent past (Ivy-Ochs et al., 2017; von Wartburg et al., 2020). Ballantyne (2002) noted that these long lag times imply that it takes too long for deglaciated terrains to totally adapt to non-glacial conditions.

Another similar aspect to consider is the influence of climatic variabilities on slope instability. The prevailing climatic conditions in the mid-Holocene were considered favorable for large RSFs (Le Roux et al., 2009). In the Alps, the cold and wet period of the mid-Holocene between 5.8 and 4.5 ka BP, which led to changes in the hydrological conditions of the slopes, was introduced as a trigger of RSFs in the Dolomites in Italy (Borgatti and Soldati, 2010; Ivy-Ochs et al., 2017). In non-glaciated areas of the southwestern Alps, Zerathe et al. (2014) showed that a series of landslides between 4.7 and 3.7 ka BP were triggered by heavy rainfalls associated with the "4.2 ka" climatic event. However, the influence of climate changes on the instability of slopes during the mid-Holocene is not limited to the Alpine RSFs; the outer-Alpine mountains in Europe were also affected by these climatic variabilities. For example, a group of 3–6 paraglacial RSFs with a mean age of 4.9 ± 0.6 ka in western Norway was attributed to warmer and wetter climatic conditions (Hilger et al., 2018). This evidence may suggest that climatic deteriorations in the mid-Holocene affected slope stability on a larger geographic scale, a topic that requires further investigation.

7. CONCLUSIONS AND RECOMMENDATIONS

7.1 Conclusions

This thesis investigated the rate and style of erosional processes using in-situ ^{36}Cl cosmogenic nuclide in the southern Central Anatolian Plateau (CAP). The first section focused on quantifying the ^{36}Cl-derived denudation rates of carbonate outcrops across the temperate Mediterranean to continental and arid climate gradient over the late Pleistocene timescale. The obtained denudation rates were used to explore the interactions between climate, uplift, lithology, and denudation and to identify their role in the evolution of the carbonate landscape. The second section presents the conclusions on the timing of a paleo-rock avalanche (namely the Namaras rock avalanche) in the glaciated Geyikdağ mountain, its morphometric analysis, and its precondition, preparatory, and triggering factors. The following paragraphs will explain the conclusions of these two sections in detail.

7.1.1 Conclusions concerning the ^{36}Cl-derived denudation rate of carbonate outcrops and their controlling factors

^{36}Cl-derived outcrop denudation rates range from 1.92 ± 0.31 mm/ka to 45.77 ± 3.91 mm/ka (mean: 14.40 ± 0.47 mm/ka), varying by a factor of 23 among sampling sites. The distribution of denudation rates shows systematic spatial variability with a decreasing trend from SW to NE. On the plateau, the calculated denudation rates are lower than the predicted theoretical maximum dissolution rates, which along with a strong correlation between denudation and precipitation, indicate the significant control of climate on carbonate denudation. The climate control resulted in a close agreement between denudation pattern and climate zones, where the high-to-moderate denudation rates correspond to the continental climate in the Central Taurides and the low denudation rates to the arid in the CAP interior. Moreover, the strong correlation between denudation and precipitation and the weak correlation with rock mechanical strength indicate the dominance of chemical weathering. The denudation rates for samples in the Mediterranean coastal region are higher than the theoretical maximum

dissolution rates, suggesting the role of physical erosion. In the CAP interior, low denudation rates imply a slowly evolving landscape with prolonged aridity. Among the evaluated parameters, the control of rock mechanical strength, porosity, and water absorption by weight on carbonate denudation remained insignificant.

Precipitation gradient imposes an asymmetric denudation pattern across the plateau margin. This pattern agrees with the asymmetric uplift pattern, which implies the coupling of denudation, precipitation, and tectonic uplift. The uplift rate suggested for the plateau margin is several times higher than the calculated denudation rates, implying a transient landscape in which rapid uplift rates are not counterbalanced by denudation. In the Central Taurides, infiltration of surface runoff by intense karstification delayed the topographic response to tectonic uplift, leading to disequilibrium between uplift and denudation rates. Therefore, low surface denudation and strong subsurface karstification prolonged the landscape adjustment to rapid uplift rates and led to the preservation of the high-elevation topography.

Overall, the calculated denudation rates are consistent with previously reported carbonate outcrop denudation rates in the Eastern Mediterranean and are at the lower end of the global records. Like previous studies, this study highlights the primary control of climate, particularly precipitation, on carbonate denudation. In addition, this data underlines the control of uplift and tectonic forcing on carbonate denudation and indicates that the effect of tectonic uplift over denudation rate is not independent of precipitation but mediated by it.

7.1.2 Conclusions concerning the age and geomorphology of the paraglacial Namaras rock avalanche

Based on geomorphology and ^{36}Cl surface exposure dating, the Namaras rock avalanche (NRA) in the Central Taurides, with an estimated total volume of 4.3 million m^3, consists of two mid-to-late Holocene successive rock avalanche events. The rock avalanche occurred in the Jurassic-Cretaceous bedded neritic limestone in a formerly glaciated terrain. The source area is a glacial cirque, and the rock avalanche deposit with a 0.430 km^2 area covers the lateral and hummocky moraines down in the valley. Dating the rock avalanche using the ^{36}Cl cosmogenic nuclides on six boulders yielded two very close but distinct ages: one event with a weighted average age of 4.59 ± 0.25 ka and the other with 3.77 ± 0.20 ka. ^{36}Cl exposure dating of the lateral moraine,

superimposed by the rock avalanche deposit, revealed approximately an age of 12.30 ± 1.20 ka, consistent with the previously obtained ages from the lateral moraines in the same valley.

The geomorphologic and geometric features were assessed for rock avalanche events by field investigation and remote mapping from a 19-cm resolution orthophoto. The NRA main, older event (4.59 ± 0.25 ka) has two lobes covering 0.415 km^2. The maximum runout distance of 1550 m and 600 m elevation loss yielded a travel angle of 21° for the older event. The right lobe of the older deposit, which runs ~30 m up over the lateral moraine, has a denser boulder distribution with greater thickness than the left lobe. The thickness of the rock avalanche deposit on the right lobe of the older event is estimated to be 20 m, which was considered the maximum thickness of the whole rock avalanche. The younger low magnitude event (3.77 ± 0.20 ka) with 0.127 km^2 area covers the older event. A maximum runout distance of 1720 m and 640 m vertical displacement resulted in a travel angle of 20° for the younger event.

Several factors have conditioned and contributed to the NRA's failure. Preconditioning factors that conditioned the slope failure are the bedding plane of limestone bedrock and cross-joints. The timing of the two events allows an analysis of potential preparatory and triggering factors. The significant lag times (roughly ~7.7 ka and ~8.5 ka) between the Geyikdağ Mountain deglaciation and the NRA failures suggest that glacial erosion and debuttressing have played the role of preparatory factors. Moreover, karstification and carbonate dissolution might likewise acted as preparatory factors. The mid-to-late Holocene climate variabilities may have triggered the NRA. Indeed, the NRA can be considered the result of paraglacial adjustments following deglaciation, accelerated by climatic shifts or deteriorations. Warm temperatures associated with intense rainfalls in the mid-Holocene could have triggered the older rock avalanche event. The younger event may have been triggered by the influence of the long, wet period of the late Holocene. Meanwhile, the coincidence of the NRA timing with the recognized period of enhanced RSFs in the Alps during the mid-to-late Holocene transition (5–3 ka BP) provides an essential contribution to the spatial and temporal distribution of paraglacial RSFs of Holocene and the ongoing discussion around their plausible triggers.

7.2 Recommendations

As summarized in the conclusion section (7.1.1), this thesis improved our understanding of the denudation of flat-lying carbonate bedrocks in the karstic terrains of the southern Central Anatolian Plateau. However, some questions remain concerning the quantitative amount of physical erosion vs chemical weathering, the denudation rate of different landform features, and basin-wide denudation rates. Sampling spring waters near the sampled carbonate outcrops can provide valuable information on chemical weathering. Moreover, sampling carbonate hillslopes and comparing them with hilltop denudation rates will further improve our knowledge of the denudation dynamics in this karstic landscape. Moreover, determining the basin-wide denudation rate of carbonates in comparison with outcrop denudation will answer the questions regarding relief growth in the tectonically active setting of southern CAP.

Furthermore, as mentioned above (7.1.2), this study provided valuable information on the timing of a paraglacial rock slope failure in the glaciated mountain ranges of the Central Taurides and unraveled its relation with glacial activity. However, due to the lack of similar studies, questions concerning the spatial and temporal pattern of prehistoric rock slope failures and their interaction with climatic and seismic events remain unanswered. Therefore, to answer these questions, more studies on the timing of paraglacial landforms, particularly rock slope failures, are required in the Central Taurides.

REFERENCES

Ahnert, F. (1970). Functional relationships between denudation, relief, and uplift in large, mid-latitude drainage basins. *American Journal of Science*, *268*(3), 243-263. https://doi.org/10.2475/ajs.268.3.243

Allen, S., and Huggel, C. (2013). Extremely warm temperatures as a potential cause of recent high mountain rockfall. *Global and Planetary Change*, *107*, 59–69. https://doi.org/10.1016/j.gloplacha.2013.04.007

Altınay, O., Sarıkaya, M. A., Çiner, A., Žebre, M., Stepišnik, U., Yıldırım, C., Yetemen, Ö., and Wilcken, K. M. (2022). Cosmogenic ^{36}Cl surface exposure dating of glacial landforms on Mt. Barla (SW Turkey). *Geomorphology*, *416*, 108424. https://doi.org/10.1016/j.geomorph.2022.108424

Arpat, E., and Özgül, N. (1972). Rock Glaciers in Geyik Dağı Area, Central Taurus (In Turkish). *Bull. Miner. Res. Explor. 78*, 30–35.

Atabey, E., Atabey, N., Hakyemez, A., İslamoğlu, Y., Sözeri, Ş., Özçelik, N. N., Saraç, G., and Ünay, E. (2000). Mut-Karaman arası Miyosen havzasının litostratigrafisi ve sedimantolojisi (Orta Toroslar). *Maden Tetkik ve Arama Dergisi*, *122*, 53–72.

Atalay, I., Efe, R., and Öztürk, M. (2014a). Effects of Topography and Climate on the Ecology of Taurus Mountains in the Mediterranean Region of Turkey. *Procedia - Social and Behavioral Sciences*, *120*, 142–156. https://doi.org/10.1016/j.sbspro.2014.02.091

Atalay, I., Efe, R., and Öztürk, M. (2014b). Ecology and Classification of Forests in Turkey. *Procedia - Social and Behavioral Sciences*, *120*, 788–805. https://doi.org/10.1016/j.sbspro.2014.02.163

Avnaim-Katav, S., Almogi-Labin, A., Schneider-Mor, A., Crouvi, O., Burke, A. A., Kremenetski, K. V., and MacDonald, G. M. (2019). A multi-proxy shallow marine record for Mid-to-Late Holocene climate variability, Thera eruptions and cultural change in the Eastern Mediterranean. *Quaternary Science Reviews*, *204*, 133–148. https://doi.org/10.1016/j.quascirev.2018.12.001

Avni, S., Joseph-Hai, N., Haviv, I., Matmon, A., Benedetti, L., and Team, A. (2019). Patterns and rates of 10^3–10^5 yr denudation in carbonate terrains under subhumid to subalpine climatic gradient, Mount Hermon, Israel. *GSA Bulletin*, *131*(5–6), 899–912. https://doi.org/10.1130/B31973.1

Balco, G. (2011). Contributions and unrealized potential contributions of cosmogenic-nuclide exposure dating to glacier chronology, 1990–2010. *Quaternary Science Reviews*, *30*(1–2), 3–27. https://doi.org/10.1016/j.quascirev.2010.11.003

Balco, G., Stone, J. O., Lifton, N. A., and Dunai, T. J. (2008). A complete and easily accessible means of calculating surface exposure ages or erosion rates from ^{10}Be and ^{26}Al measurements. *Quaternary Geochronology*, *3*(3), 174–195. https://doi.org/10.1016/j.quageo.2007.12.001

Ballantyne, C. K. (2002). Paraglacial geomorphology. *Quaternary Science Reviews*, *21*, 1935–2017.

Ballantyne, C. K., Sandeman, G. F., Stone, J. O., and Wilson, P. (2014). Rock-slope failure following Late Pleistocene deglaciation on tectonically stable mountainous terrain. *Quaternary Science Reviews*, *86*, 144–157. https://doi.org/10.1016/j.quascirev.2013.12.021

Ballantyne, C. K., Stone, J. O., and Fifield, L. K. (1998). Cosmogenic Cl-36 dating of postglacial landsliding at The Storr, Isle of Skye, Scotland. *The Holocene*, *8*(3), 347–351. https://doi.org/10.1191/095968398666797200

Ballesteros, E. M., Martín, C. M., and Talegón, G.J. (2010). Role of porosity in rock weathering processes: a theoretical approach. *Cad. Lab. Xeol. Laxe*, *35*, pp. 147-162.

Bayarı, C. S., Klimchouk, A., Sarıkaya, M. A., and Nazik, L. (2019). Aladağlar Mountain range: a landscape-shaped by the interplay of glacial, karstic, and fluvial erosion. In C. Kuzucuoğlu, A. Çiner, and N. Kazancı (Eds.), *Landscapes and Landforms of Turkey* (pp. 423–435). Cham: Springer International Publishing. https://doi.org/10.1007/978-3-030-03515-0_22

Bayrakdar, C., Çılğın, Z., and Keserci, F. (2020a). Traces of late quaternary glaciations and paleoclimatic interpretation of Mount Akdağ (Alanya, 2451 m), Southwest Turkey. *Mediterranean Geoscience Reviews*, *2*(1), 135–151. https://doi.org/10.1007/s42990-020-00026-5

Bayrakdar, C., Gorum, T., Çılğın, Z., Vockenhuber, C., Ivy-Ochs, S., and Akçar, N. (2020b). Chronology and Geomorphological Activity of the Akdag Rock Avalanche (SW Turkey). *Frontiers in Earth Science*, *8*, 295. https://doi.org/10.3389/feart.2020.00295

Beck, H. E., Zimmermann, N. E., McVicar, T. R., Vergopolan, N., Berg, A., and Wood, E. F. (2018). Present and future Köppen-Geiger climate classification maps at 1-km resolution. *Scientific Data*, *5*(1), 180214. https://doi.org/10.1038/sdata.2018.214

Ben-Asher, M., Haviv, I., Crouvi, O., Roering, J. J., and Matmon, A. (2021). The convexity of carbonate hilltops: ^{36}Cl constraints on denudation and chemical weathering rates and implications for hillslope curvature. *GSA Bulletin*, *133*(9–10), 1930–1946. https://doi.org/10.1130/B35658.1

Bierman, P. R. (1994). Using in situ produced cosmogenic isotopes to estimate rates of landscape evolution: A review from the geomorphic perspective. *Journal of Geophysical Research: Solid Earth*, *99*(B7), 13885–13896. https://doi.org/10.1029/94JB00459

Borchers, B., Marrero, S., Balco, G., Caffee, M., Goehring, B., Lifton, N., Nishiizumi, K., Phillips, F., Schaefer, J., and Stone, J. (2016). Geological calibration of spallation production rates in the CRONUS-Earth project. *Quaternary Geochronology*, *31*, 188–198. https://doi.org/10.1016/j.quageo.2015.01.009

Borgatti, L., and Soldati, M. (2010). Landslides as a geomorphological proxy for climate change: A record from the Dolomites (northern Italy). *Geomorphology*, *120*(1–2), 56–64. https://doi.org/10.1016/j.geomorph.2009.09.015

Çiner, A., Deynoux, M., and Çörekcioğlu, E. (1999). Hummocky moraines in the Namaras and Susam Valleys, Central Taurids, SW Turkey. *Quaternary Science Reviews*, *18*(4–5), 659–669. https://doi.org/10.1016/S0277-3791(98)00103-6

Çiner, A., Doğan, U., Yıldırım, C., Akçar, N., Ivy-Ochs, S., Alfimov, V., Kubik, P.W., and Schlüchter, C. (2015a). Quaternary uplift rates of the Central Anatolian Plateau, Turkey: Insights from cosmogenic isochron-burial nuclide dating of the Kızılırmak River terraces. *Quaternary Science Reviews*, *107*, 81–97. https://doi.org/10.1016/j.quascirev.2014.10.007

Çiner, A., Sarıkaya, M. A., and Yıldırım, C. (2015b). Late Pleistocene piedmont glaciations in the Eastern Mediterranean; insights from cosmogenic ^{36}Cl dating of hummocky moraines in southern Turkey. *Quaternary Science Reviews*, *116*, 44–56. https://doi.org/10.1016/j.quascirev.2015.03.017

Çiner, A., Sarıkaya, M. A., and Yıldırım, C. (2017). Misleading old age on a young landform? The dilemma of cosmogenic inheritance in surface exposure dating: Moraines vs. rock glaciers. *Quaternary Geochronology*, *42*, 76–88. https://doi.org/10.1016/j.quageo.2017.07.003

Cockburn, H. A. P., and Summerfield, M. A. (2004). Geomorphological applications of cosmogenic isotope analysis. *Progress in Physical Geography: Earth and Environment*, *28*(1), 1–42. https://doi.org/10.1191/0309133304pp395oa

Copons, R., Vilaplana, J. M., and Linares, R. (2009). Rockfall travel distance analysis by using empirical models (Solà d'Andorra la Vella, Central Pyrenees). *Natural Hazards and Earth System Sciences*, *9*(6), 2107–2118. https://doi.org/10.5194/nhess-9-2107-2009

Cosentino, D., Schildgen, T. F., Cipollari, P., Faranda, C., Gliozzi, E., Hudackova, N., Lucifora, S., and Strecker, M. R. (2012). Late Miocene surface uplift of the southern margin of the Central Anatolian Plateau, Central Taurides, Turkey. *Geological Society of America Bulletin*, *124*(1–2), 133–145. https://doi.org/10.1130/B30466.1

Crozier, M. J. (2010). Deciphering the effect of climate change on landslide activity: A review. *Geomorphology*, *124*(3–4), 260–267. https://doi.org/10.1016/j.geomorph.2010.04.009

Cruden, D.M., and Varnes, D.J. (1996). Landslide Types and Processes, Special Report. *Transportation Research Board, National Academy of Sciences*, *247*, 36–75.

Cucchi, F., Forti, F., and Furlani, S. (2006). Lowering rates of limestone along the western Istrian shoreline and the Gulf of Trieste. *Geografia Fisica e Dinamica Quaternaria*, *29*(1), 61-69.

Curry, A. M. (2021). Paraglacial Rock-Slope Failure Following Deglaciation in Western Norway. In A. A. Beylich (Ed.), *Landscapes and Landforms of Norway* (pp. 97–130). Cham: Springer International Publishing. https://doi.org/10.1007/978-3-030-52563-7_5

De Waele, J., and Gutiérrez, F. (2022). *Karst Hydrogeology, Geomorphology and Caves* (1st ed.). John Wiley & Sons. https://doi.org/10.1002/9781119605379

Dean, J. R., Jones, M. D., Leng, M. J., Noble, S. R., Metcalfe, S. E., Sloane, H. J., Sahy, D., Eastwood, W.J., and Roberts, C. N. (2015). Eastern Mediterranean hydroclimate over the late glacial and Holocene, reconstructed from the sediments of Nar lake, central Turkey, using stable isotopes and carbonate mineralogy. *Quaternary Science Reviews*, *124*, 162–174. https://doi.org/10.1016/j.quascirev.2015.07.023

Demirtaşlı, E., Turhan, N., Bilgin, A., and Selim, M. (1984). Geology of the Bolkar mountains. In *geology of the Taurus belt. International symposium* (pp. 125-141).

Dockhorn, B., Neumaier, S., Hartmann, F. J., Petitjean, C., Faestermann, H., Korschinek, G., Morinaga, H., and Nolte, E. (1991). Determination of erosion rates with cosmic ray produced ^{36}Cl. *Zeitschrift für Physik A Hadrons and Nuclei*, *341*, 117-119

Dorren, L. K. A., Maier, B., Putters, U. S., and Seijmonsbergen, A. C. (2004). Combining field and modelling techniques to assess rockfall dynamics on a protection forest hillslope in the European Alps. *Geomorphology*, *57*(3–4), 151–167. https://doi.org/10.1016/S0169-555X(03)00100-4

Dortch, J. M., Owen, L. A., Haneberg, W. C., Caffee, M. W., Dietsch, C., and Kamp, U. (2009). Nature and timing of large landslides in the Himalaya and Transhimalaya of northern India. *Quaternary Science Reviews*, *28*(11–12), 1037–1054. https://doi.org/10.1016/j.quascirev.2008.05.002

Dunai, T. (2010). *Cosmogenic Nuclides: Principles, Concepts and Applications in the Earth Surface Sciences.* Cambridge University Press.

Dusar, B., Verstraeten, G., Notebaert, B., and Bakker, J. (2011). Holocene environmental change and its impact on sediment dynamics in the Eastern Mediterranean. *Earth-Science Reviews*, *108*(3–4), 137–157. https://doi.org/10.1016/j.earscirev.2011.06.006

Eastwood, Warren J., Leng, M. J., Roberts, N., and Davis, B. (2007). Holocene climate change in the eastern Mediterranean region: A comparison of stable isotope and pollen data from Lake Gölhisar, southwest Turkey. *Journal of Quaternary Science*, *22*(4), 327–341. https://doi.org/10.1002/jqs.1062

Eastwood, W.J., Roberts, N., Lamb, H. F., and Tibby, J. C. (1999). Holocene environmental change in southwest Turkey: A palaeoecological record of lake and catchment-related changes. *Quaternary Science Reviews*, *18*(4–5), 671–695. https://doi.org/10.1016/S0277-3791(98)00104-8

Eberhardt, E., Stead, D., and Coggan, J. S. (2004). Numerical analysis of initiation and progressive failure in natural rock slopes—The 1991 Randa rockslide. *International Journal of Rock Mechanics and Mining Sciences*, *41*(1), 69–87. https://doi.org/10.1016/S1365-1609(03)00076-5

Egholm, D. L., Nielsen, S. B., Pedersen, V. K., and Lesemann, J.-E. (2009). Glacial effects limiting mountain height. *Nature*, *460*(7257), 884–887. https://doi.org/10.1038/nature08263

Emre, Ö., Duman, T. Y., Özalp, S., Şaroğlu, F., Olgun, Ş., Elmacı, H., and Çan, T. (2018). Active fault database of Turkey. *Bulletin of Earthquake Engineering*, *16*(8), 3229–3275. https://doi.org/10.1007/s10518-016-0041-2

Evans, D., Rodés, Á., and Tye, A. (2021). The sensitivity of cosmogenic radionuclide analysis to soil bulk density: Implications for soil formation rates. *European Journal of Soil Science*, *72*(1), 174–182. https://doi.org/10.1111/ejss.12982

Fick, S. E., and Hijmans, R. J. (2017). WorldClim 2: New 1-km spatial resolution climate surfaces for global land areas. *International Journal of Climatology*, *37*(12), 4302–4315. https://doi.org/10.1002/joc.5086

Finné, M., Holmgren, K., Sundqvist, H. S., Weiberg, E., and Lindblom, M. (2011). Climate in the eastern Mediterranean, and adjacent regions, during the past 6000 years – A review. *Journal of Archaeological Science*, *38*(12), 3153–3173. https://doi.org/10.1016/j.jas.2011.05.007

Finné, M., Woodbridge, J., Labuhn, I., and Roberts, C. N. (2019). Holocene hydro-climatic variability in the Mediterranean: A synthetic multi-proxy reconstruction. *The Holocene*, *29*(5), 847–863. https://doi.org/10.1177/0959683619826634

Ford, D., and Williams, P. (2007). *Karst Hydrogeology and Geomorphology*. John Wiley & Sons.

Franklin, J. A. (1979). Suggested methods for determining water content, porosity, density, absorption and related properties and swelling and slake-durability index properties. *International Journal of Rock Mechanics and Mining Sciences*, *16*(2), 143-151.

Frisch, W., Kuhlemann, J., Dunkl, I., and Székely, B. (2001). The Dachstein paleosurface and the Augenstein Formation in the Northern Calcareous Alps – a mosaic stone in the geomorphological evolution of the Eastern Alps. *International Journal of Earth Sciences*, *90*(3), 500–518. https://doi.org/10.1007/s005310000189

Furlani, S., Cucchi, F., Forti, F., and Rossi, A. (2009). Comparison between coastal and inland Karst limestone lowering rates in the northeastern Adriatic Region (Italy and Croatia). *Geomorphology*, *104*(1–2), 73–81. https://doi.org/10.1016/j.geomorph.2008.05.015

Gaillardet, J., Calmels, D., Romero-Mujalli, G., Zakharova, E., and Hartmann, J. (2019). Global climate control on carbonate weathering intensity. *Chemical Geology*, *527*, 118762. https://doi.org/10.1016/j.chemgeo.2018.05.009

Gallach, X., Ravanel, L., Egli, M., Brandova, D., Schaepman, M., Christl, M., Gruber, S., Deline, P., Carcaillet, J., and Pallandre, F. (2018). Timing of rockfalls in the Mont Blanc massif (Western Alps): Evidence from surface exposure dating with cosmogenic ^{10}Be. *Landslides*, *15*(10), 1991–2000. https://doi.org/10.1007/s10346-018-0999-8

Gariano, S. L., and Guzzetti, F. (2016). Landslides in a changing climate. *Earth-Science Reviews*, *162*, 227–252. https://doi.org/10.1016/j.earscirev.2016.08.011

Gedik, A., Bîrgîlî, Ş., Yilmaz, H., and Yoldaş, R. (1979). Mut-Ermenek-Silifke yöresinin jeolojisi ve petrol olanakları. *Bull. Geol. Soc. Turk. 22*, 7–26.

Godard, V., Ollivier, V., Bellier, O., Miramont, C., Shabanian, E., Fleury, J., Benedetti, L., Guillou, V., and ASTER Team (2016). Weathering-limited hillslope evolution in carbonate landscapes. *Earth and Planetary Science Letters*, *446*, 10–20. https://doi.org/10.1016/j.epsl.2016.04.017

Gosse, J. C., and Phillips, F. M. (2001). Terrestrial in situ cosmogenic nuclides: theory and application. *Quaternary Science Review*s, *20*(14), 1475–1560. https://doi.org/10.1016/S0277-3791(00)00171-2

Goudie, A. S. (2006). The Schmidt Hammer in geomorphological research. *Progress in Physical Geography*, *30*(6), 703-718.

Goudie, A. S. (2016). Quantification of rock control in geomorphology. *Earth-Science Reviews*, *159*, 374–387. https://doi.org/10.1016/j.earscirev.2016.06.012

Grämiger, L. M., Moore, J. R., Gischig, V. S., and Loew, S. (2018). Thermomechanical stresses drive damage of Alpine valley rock walls during repeat glacial cycles. *Journal of Geophysical Research: Earth Surface*, *123*(10), 2620–2646. https://doi.org/10.1029/2018JF004626

Grämiger, L. M., Moore, J. R., Vockenhuber, C., Aaron, J., Hajdas, I., and Ivy-Ochs, S. (2016). Two early Holocene rock avalanches in the Bernese Alps (Rinderhorn, Switzerland). *Geomorphology*, *268*, 207–221. https://doi.org/10.1016/j.geomorph.2016.06.008

Granger, D. E., and Riebe, C. S. (2014). Cosmogenic nuclides in weathering and erosion. In *Treatise on Geochemistry* (pp. 401–436). Elsevier. https://doi.org/10.1016/B978-0-08-095975-7.00514-3

Gunzburger, Y., Merrien-Soukatchoff, V., and Guglielmi, Y. (2005). Influence of daily surface temperature fluctuations on rock slope stability: Case study of the Rochers de Valabres slope (France). *International Journal of Rock Mechanics and Mining Sciences*, *42*(3), 331–349. https://doi.org/10.1016/j.ijrmms.2004.11.003

Hashemi, A., Sarıkaya, M. A., Görüm, T., Wilcken, K. M., Ciner, A., Žebre, M., ... and Yıldırım, C. (2022). The Namaras rock avalanche: Evidence of mid-to-late Holocene paraglacial activity in the Central Taurus Mountains, SW Turkey. *Geomorphology*, *408*, 108261. https://doi.org/j.geomorph.2022.108261

Hashemi, A., Sarıkaya, M. A., Wilcken, K. M., and Öztürk, M. Z. (2023). Controls on long-term denudation rate of carbonate terrains in the Eastern Mediterranean. *Quaternary Science Reviews*, *321*, 108351. https://doi.org/10.1016/j.quascirev.2023.108351

Heim, A. (1932). *Bergsturz und Menschenleben*. Naurforsch. Ges., 20, 1–218, Naurforschenden Gesellshaft in Zurich, Zurich, Switzerland.

Hermanns, R. L., Fauqué, L., and Wilson, C. G. J. (2015). ^{36} Cl terrestrial cosmogenic nuclide dating suggests Late Pleistocene to Early Holocene mass movements on the south face of Aconcagua mountain and in the Las Cuevas–Horcones valleys, Central Andes, Argentina. In Sepulveda, S. A., Giambiagi, L. B., Moreiras, S. M., Pinto, L., Tunik, M., Hoke, G.D. and Faries, M., (eds) *Geodynamic Processes in the Andes of Central Chile and Argentina.* Geological Society, London, Special Publications, *399*(1), 345–368. https://doi.org/10.1144/SP399.19

Hilger, P., Gosse, J. C., and Hermanns, R. L. (2019). How significant is inheritance when dating rockslide boulders with terrestrial cosmogenic nuclide dating?—A case study of an historic event. *Landslides*, *16*(4), 729–738. https://doi.org/10.1007/s10346-018-01132-0

Hilger, P., Hermanns, R. L., Gosse, J. C., Jacobs, B., Etzelmüller, B., and Krautblatter, M. (2018). Multiple rock-slope failures from Mannen in Romsdal Valley, western Norway, revealed from Quaternary geological mapping and ^{10}Be exposure dating. *The Holocene*, *28*(12), 1841–1854. https://doi.org/10.1177/0959683618798165

Hungr, O., Corominas, J., and Eberhardt, E. (2005). Estimating landslide motion mechanism, travel distance and velocity. In Hungr O, Fell R, Couture R, Eberhardt E, eds. *Landslide Risk Management*. London: CRC Press. 99–128 https://doi.org/10.1201/9781439833711-7

Hungr, O., Leroueil, S., and Picarelli, L. (2014). The Varnes classification of landslide types, an update. *Landslides*, *11*(2), 167–194. https://doi.org/10.1007/s10346-013-0436-y

Ivy-Ochs, S., Martin, S., Campedel, P., Hippe, K., Alfimov, V., Vockenhuber, C., … Viganò, A. (2017). Geomorphology and age of the Marocche di Dro rock avalanches (Trentino, Italy). *Quaternary Science Reviews*, *169*, 188–205. https://doi.org/10.1016/j.quascirev.2017.05.014

Ivy-Ochs, S., Poschinger, A. v., Synal, H. A., and Maisch, M. (2009). Surface exposure dating of the Flims landslide, Graubünden, Switzerland. *Geomorphology*, *103*(1), 104–112. https://doi.org/10.1016/j.geomorph.2007.10.024

Ivy-Ochs, Susan, and Schaller, M. (2009). Examining Processes and Rates of Landscape Change with Cosmogenic Radionuclides. In *Radioactivity in the Environment*, *16*, 231–294. https://doi.org/10.1016/S1569-4860(09)01606-4

Iyigun, C., Türkeş, M., Batmaz, İ., Yozgatligil, C., Purutçuoğlu, V., Koç, E. K., and Öztürk, M. Z. (2013). Clustering current climate regions of Turkey by using a multivariate statistical method. *Theoretical and Applied Climatology, 114*(1–2), 95–106. https://doi.org/10.1007/s00704-012-0823-7

Kadirioğlu, F. T., Kartal, R. F., Kılıç, T., Kalafat, D., Duman, T. Y., Eroğlu Azak, T., Özalp, S., and Emre, Ö. (2018). An improved earthquake catalogue (M ≥ 4.0) for Turkey and its near vicinity (1900–2012). *Bulletin of Earthquake Engineering*, *16*(8), 3317–3338. https://doi.org/10.1007/s10518-016-0064-8

Köpfli, P., Grämiger, L. M., Moore, J. R., Vockenhuber, C., and Ivy-Ochs, S. (2018). The Oeschinensee rock avalanche, Bernese Alps, Switzerland: A co-seismic failure 2300 years ago? *Swiss Journal of Geosciences*, *111*(1–2), 205–219. https://doi.org/10.1007/s00015-017-0293-0

Köse, O., Sarıkaya, M. A., Çiner, A., Candaş, A., Yıldırım, C., and Wilcken, K. M. (2022). Reconstruction of Last Glacial Maximum glaciers and palaeoclimate in the central Taurus Range, Mt. Karanfil, of the Eastern Mediterranean. *Quaternary Science Reviews*, *291*, 107656. https://doi.org/10.1016/j.quascirev.2022.107656

Krautblatter, M., Moser, M., Schrott, L., Wolf, J., and Morche, D. (2012). Significance of rockfall magnitude and carbonate dissolution for rock slope erosion and geomorphic work on Alpine limestone cliffs (Reintal, German Alps). *Geomorphology*, *167*, 21–34. https://doi.org/10.1016/j.geomorph.2012.04.007

Krklec, K., Braucher, R., Perica, D., and Domínguez-Villar, D. (2022). Long-term denudation rate of karstic North Dalmatian Plain (Croatia) calculated from ^{36}Cl cosmogenic nuclides. *Geomorphology*, *413*, 108358. https://doi.org/10.1016/j.geomorph.2022.108358

Krklec, K., Domínguez-Villar, D., Carrasco, R. M., and Pedraza, J. (2016). Current denudation rates in dolostone karst from central Spain: Implications for the formation of unroofed caves. *Geomorphology*, *264*, 1–11. https://doi.org/10.1016/j.geomorph.2016.04.007

Krklec, K., Domínguez-Villar, D., and Perica, D. (2021). Use of rock tablet method to measure rock weathering and landscape denudation. *Earth-Science Reviews*, *212*, 103449. https://doi.org/10.1016/j.earscirev.2020.103449

Kuzucuoğlu, C., Dörfler, W., Kunesch, S., and Goupille, F. (2011). Mid- to late-Holocene climate change in central Turkey: The Tecer Lake record. *The Holocene*, *21*(1), 173–188. https://doi.org/10.1177/0959683610384163

Kuzucuoglu, C., Fontugne, M., and Mouralis, D. (2004). Holocene terraces in the Middle Euphrates Valley, between Halfeti and Karkemish (Gaziantep, Turkey) [Terrasses holocènes dans la moyenne vallée de l'Euphrate entre Halfeti et Karkemish (Gaziantep, Turquie).]. *Quaternaire*, *15*(1), 195–206. https://doi.org/10.3406/quate.2004.1767

Lal, D. (1991). Cosmic ray labeling of erosion surfaces: In situ nuclide production rates and erosion models. *Earth and Planetary Science Letters, 104*(2–4), 424–439. https://doi.org/10.1016/0012-821X(91)90220-C

Lauritzen, S.E. (1990). Autogenic and allogenic denudation in carbonate karst by the multiple basin method: An example from Svartisen, North Norway. *Earth Surface Processes and Landforms*, *15*(2), 157–167. https://doi.org/10.1002/esp.3290150206

Le Roux, O., Schwartz, S., Gamond, J. F., Jongmans, D., Bourles, D., Braucher, R., …and Leanni, L. (2009). CRE dating on the head scarp of a major landslide (Séchilienne, French Alps), age constraints on Holocene kinematics. *Earth and Planetary Science Letters*, *280*(1–4), 236–245. https://doi.org/10.1016/j.epsl.2009.01.034

Levenson, Y., Ryb, U., and Emmanuel, S. (2017). Comparison of field and laboratory weathering rates in carbonate rocks from an Eastern Mediterranean drainage basin. *Earth and Planetary Science Letters*, *465*, 176–183. https://doi.org/10.1016/j.epsl.2017.02.031

Lifton, N., Sato, T., and Dunai, T. J. (2014). Scaling in situ cosmogenic nuclide production rates using analytical approximations to atmospheric cosmic-ray fluxes. *Earth and Planetary Science Letters*, *386*, 149–160. https://doi.org/10.1016/j.epsl.2013.10.052

Marrero, S. M., Hein, A. S., Naylor, M., Attal, M., Shanks, R., Winter, K., … and Sugden, D. (2018). Controls on subaerial erosion rates in Antarctica. *Earth and Planetary Science Letters*, *501*, 56–66. https://doi.org/10.1016/j.epsl.2018.08.018

Marrero, S. M., Phillips, F. M., Borchers, B., Lifton, N., Aumer, R., & Balco, G. (2016a). Cosmogenic nuclide systematics and the CRONUScalc program. *Quaternary Geochronology*, *31*, 160–187. https://doi.org/10.1016/j.quageo.2015.09.005

Marrero, S. M., Phillips, F. M., Caffee, M., and Gosse, J. (2021). Corrigendum to "CRONUS-Earth cosmogenic ^{36}Cl calibration"[Quat. Geochronol. 31 (2016) 199–219]. *Quaternary Geochronology*, *61*, 101130. https://doi.org/10.1016/j.quageo.2020.101130

Marrero, S. M., Phillips, F. M., Caffee, M. W., and Gosse, J. C. (2016b). CRONUS-Earth cosmogenic ^{36}Cl calibration. *Quaternary Geochronology*, *31*, 199–219. https://doi.org/10.1016/j.quageo.2015.10.002

Matsushi, Y., Hattanji, T., Akiyama, S., Sasa, K., Takahashi, T., Sueki, K., and Matsukura, Y. (2010b). Evolution of solution dolines inferred from cosmogenic ^{36}Cl in calcite. *Geology*, *38*(11), 1039–1042. https://doi.org/10.1130/G31302.1

Matsushi, Y., Sasa, K., Takahashi, T., Sueki, K., Nagashima, Y., and Matsukura, Y. (2010a). Denudation rates of carbonate pinnacles in Japanese karst areas: Estimates from cosmogenic ^{36}Cl in calcite. *Nuclear Instruments and Methods in Physics Research Section B: Beam Interactions with Materials and Atoms*, *268*(7–8), 1205–1208. https://doi.org/10.1016/j.nimb.2009.10.134

Matthews, J. A., Owen, G., Winkler, S., Vater, A. E., Wilson, P., Mourne, R. W., and Hill, J. L. (2016). A rock-surface microweathering index from Schmidt hammer R-values and its preliminary application to some common rock types in southern Norway. *Catena*, *143*, 35–44. https://doi.org/10.1016/j.catena.2016.03.018

McColl, S. T. (2012). Paraglacial rock-slope stability. *Geomorphology*, *153*, 1–16. https://doi.org/10.1016/j.geomorph.2012.02.015

Messerli, B. (1967). Die eiszeitliche und die gegenwärtige Vergletscherung im Mittelmeerraum, *Geogr. Helv., 22*, 105–228. https://doi.org/10.5194/gh-22-105-1967, 1967

Mitchell, S., and Montgomery, D. (2006). Influence of a glacial buzzsaw on the height and morphology of the Cascade Range in central Washington State, USA. *Quaternary Research*, *65*(1), 96-107. Doi:10.1016/j.yqres.2005.08.018. (2006). https://doi.org/10.1016/j.yqres.2005.08.018

Monod, O. (1977). *Recherches géologiques dans le Taurus occidental au sud de Beysehir (Turquie)* (Doctoral dissertation, Université de Paris-Sud Centre d'Orsay).

Nagelisen, J., Moore, J. R., Vockenhuber, C., and Ivy-Ochs, S. (2015). Post-glacial rock avalanches in the Obersee Valley, Glarner Alps, Switzerland. *Geomorphology*, *238*, 94–111. https://doi.org/10.1016/j.geomorph.2015.02.031

Nakamura, A., Yokoyama, Y., Shiroya, K., Miyairi, Y., and Matsuzaki, H. (2014). Direct comparison of site-specific and basin-scale denudation rate estimation by in situ cosmogenic nuclides: An example from the Abukuma Mountains, Japan. *Progress in Earth and Planetary Science*, *1*(1), 9. https://doi.org/10.1186/2197-4284-1-9

Nazik, L., and Poyraz, M. (2017). Türkiye karst jeomorfolojisi genelini karakterize eden bir bölge: Orta Anadolu Platoları karst kuşağı. *Türk Coğrafya Dergisi*, *68*, 43-56. https://doi.org/10.17211/tcd.300414

Nazik, L., Poyraz, M., and Karabıyıkoğlu, M. (2019). Karstic Landscapes and Landforms in Turkey. In C. Kuzucuoğlu, A. Çiner, & N. Kazancı (Eds.), *Landscapes and Landforms of Turkey*, 181–196. Cham: Springer International Publishing. https://doi.org/10.1007/978-3-030-03515-0_5

Nykamp, M., Knitter, D., and Schütt, B. (2020). Late Holocene geomorphodynamics in the vicinity of Göbekli Tepe, SE Turkey. *Catena*, *195*, 104759. https://doi.org/10.1016/j.catena.2020.104759

Öğretmen, N., Cipollari, P., Frezza, V., Faranda, C., Karanika, K., Gliozzi, E., … and Cosentino, D. (2018). Evidence for 1.5 km of Uplift of the Central Anatolian Plateau's Southern Margin in the Last 450 kyr and Implications for Its Multiphased Uplift History. *Tectonics*, *37*(1), 359–390. https://doi.org/10.1002/2017TC004805

Okay, A. I., Zattin, M., Özcan, E., and Sunal, G. (2020). Uplift of Anatolia. *Turkish Journal of Earth Sciences*, *29*(5), 696–713. https://doi.org/10.3906/yer-2003-10

Oliva, M., Žebre, M., Guglielmin, M., Hughes, P. D., Çiner, A., Vieira, G., … and Yıldırım, C. (2018). Permafrost conditions in the Mediterranean region since the Last Glaciation. *Earth-Science Reviews*, *185*, 397–436. https://doi.org/10.1016/j.earscirev.2018.06.018

Ön, Z. B., Greaves, A. M., Akçer-Ön, S., and Özeren, M. S. (2021). A Bayesian test for the 4.2 ka BP abrupt climatic change event in southeast Europe and southwest Asia using structural time series analysis of paleoclimate data. *Climatic Change*, *165*(1–2), 7. https://doi.org/10.1007/s10584-021-03010-6

Ott, R. F., Gallen, S. F., Caves Rugenstein, J. K., Ivy-Ochs, S., Helman, D., Fassoulas, C., … and Willett, S. D. (2019). Chemical versus mechanical denudation in meta-clastic and carbonate bedrock catchments on Crete, Greece, and mechanisms for steep and high carbonate topography. *Journal of Geophysical Research: Earth Surface*, *124*(12), 2943–2961. https://doi.org/10.1029/2019JF005142

Ott, R., Gallen, S. F., and Helman, D. (2023). Erosion and weathering in carbonate regions reveal climatic and tectonic drivers of carbonate landscape evolution. *Earth Surface Dynamics*, *11*(2), 247–257. https://doi.org/10.5194/esurf-11-247-2023

Öztürk, M. Z. (2020). Fluvio-karstic evolution of the Taşeli Plateau (Central Taurus, Turkey). *Turkish Journal of Earth Sciences*, *29*(5), 733–746. https://doi.org/10.3906/yer-1908-1

Öztürk, M. Z., Şimşek, M., Şener, M. F., and Utlu, M. (2018). GIS based analysis of doline density on Taurus Mountains, Turkey. *Environmental Earth Sciences*, *77*(14), 536. https://doi.org/10.1007/s12665-018-7717-7

Öztürk, M. Z., Şimşek, M., Utlu, M., and Şener, M. F. (2017). Karstic depressions on Bolkar Mountain plateau, Central Taurus (Turkey): Distribution characteristics and tectonic effect on orientation. *Turkish Journal of Earth Sciences*, *26* (4), 302–313.

Pánek, T., Engel, Z., Mentlík, P., Braucher, R., Břežný, M., Škarpich, V., and Zondervan, A. (2016). Cosmogenic age constraints on post-LGM catastrophic rock slope failures in the Tatra Mountains (Western Carpathians). *Catena*, *138*, 52–67. https://doi.org/10.1016/j.catena.2015.11.005

Phillips, F. M., Argento, D. C., Balco, G., Caffee, M. W., Clem, J., Dunai, T. J., … and Zreda, M. G. (2016). The CRONUS-Earth Project: A synthesis. *Quaternary Geochronology*, *31*, 119–154. https://doi.org/10.1016/j.quageo.2015.09.006

Phillips, F. M., Stone, W. D., and Fabryka-Martin, J. T. (2001). An improved approach to calculating low-energy cosmic-ray neutron fluxes near the landratmosphere interface. *Chemical Geology, 175*(3-4), 689-701.

Phillips, J. D., Martin, L. L., Nordberg, V. G., and Andrews, W. A. (2004). Divergent evolution in fluviokarst landscapes of central Kentucky. *Earth Surface Processes and Landforms*, *29*(7), 799–819. https://doi.org/10.1002/esp.1070

Plan, L. (2005). Factors controlling carbonate dissolution rates quantified in a field test in the Austrian alps. *Geomorphology*, *68*(3–4), 201–212. https://doi.org/10.1016/j.geomorph.2004.11.014

Poisson, A. (1977). *Recherches géologiques dans les Taurides occidentales (Turquie)* (Doctoral dissertation, Universite de Paris-Sud (Centre D'orsay)).

Prager, C., Zangerl, C., Patzelt, G., and Brandner, R. (2008). Age distribution of fossil landslides in the Tyrol (Austria) and its surrounding areas. *Natural Hazards and Earth System Sciences*, *8*(2), 377–407. https://doi.org/10.5194/nhess-8-377-2008

Racano, S., Jara-Muñoz, J., Cosentino, D., and Melnick, D. (2020). Variable Quaternary Uplift Along the Southern Margin of the Central Anatolian Plateau Inferred From Modeling Marine Terrace Sequences. *Tectonics*, *39*(12). https://doi.org/10.1029/2019TC005921

Riebe, C. S., Kirchner, J. W., and Finkel, R. C. (2003). Long-term rates of chemical weathering and physical erosion from cosmogenic nuclides and geochemical mass balance. *Geochimica et Cosmochimica Acta*, *67*(22), 4411–4427. https://doi.org/10.1016/S0016-7037(03)00382-X

Roberts, N., Reed, J. M., Leng, M. J., Kuzucuoğlu, C., Fontugne, M., Bertaux, J., … and Karabiyikoğlu, M. (2001). The tempo of Holocene climatic change in the eastern Mediterranean region: New high-resolution crater-lake sediment data from central Turkey. *The Holocene*, *11*(6), 721–736. https://doi.org/10.1191/09596830195744

Roberts, Neil, Eastwood, W. J., Kuzucuoğlu, C., Fiorentino, G., and Caracuta, V. (2011). Climatic, vegetation and cultural change in the eastern Mediterranean during the mid-Holocene environmental transition. *The Holocene*, *21*(1), 147–162. https://doi.org/10.1177/0959683610386819

Rodés, Á., Pallàs, R., Braucher, R., Moreno, X., Masana, E., and Bourlés, D. L. (2011). Effect of density uncertainties in cosmogenic ^{10}Be depth-profiles: Dating a cemented Pleistocene alluvial fan (Carboneras Fault, SE Iberia). *Quaternary Geochronology*, *6*(2), 186–194. https://doi.org/10.1016/j.quageo.2010.10.004

Rodríguez-Rodríguez, L., José Fernández, F., Menéndez-Duarte, R., Guillou, V., Puente-Berdasco, B., Rinterknecht, V., and ASTER Team (2023). Age and recurrence of coseismic rock avalanches in Sierra de la Sobia (Cantabrian Mountains, Spain). *Catena*, *223*, 106931. https://doi.org/10.1016/j.catena.2023.106931

Ryb, U., Matmon, A., Erel, Y., Haviv, I., Benedetti, L., and Hidy, A. J. (2014a). Styles and rates of long-term denudation in carbonate terrains under a Mediterranean to hyper-arid climatic gradient. *Earth and Planetary Science Letters*, *406*, 142–152. https://doi.org/10.1016/j.epsl.2014.09.008

Ryb, U., Matmon, A., Erel, Y., Haviv, I., Katz, A., Starinsky, A., Angert, A., and ASTER Team (2014b). Controls on denudation rates in tectonically stable Mediterranean carbonate terrain. *Geological Society of America Bulletin*, *126*(3–4), 553–568. https://doi.org/10.1130/B30886.1

Ryb, U., Matmon, A., Haviv, I., and Benedetti, L. (2015). Exhumation and uplift coupled with precipitation along the western Dead Sea Rift margin. *Geology*, *43*(6), 483–486. https://doi.org/10.1130/G36331.1

Şahin, S., and Türkeş, M. (2013). Contemporary surface wind climatology of Turkey. *Theoretical and Applied Climatology*, *113*(1–2), 337–349. https://doi.org/10.1007/s00704-012-0789-5

Şahin, S., Türkeş, M., Wang, S.-H., Hannah, D., and Eastwood, W. (2015). Large scale moisture flux characteristics of the mediterranean basin and their relationships with drier and wetter climate conditions. *Climate Dynamics*, *45*(11–12), 3381–3401. https://doi.org/10.1007/s00382-015-2545-x

Sariş, F., Hannah, D. M., and Eastwood, W. J. (2010). Spatial variability of precipitation regimes over Turkey. *Hydrological Sciences Journal*, *55*(2), 234–249. https://doi.org/10.1080/02626660903546142

Sarıkaya, M. A. (2009). *Late Quaternary Glaciation and Paleoclimate of Turkey Inferred from Cosmogenic ^{36}Cl Dating of Moraines and Glacier Modelling.* Hydrology and Water Resorces. Unpublished PhD thesis. University of Arizona, Tucson, AZ, p. 303.

Sarıkaya, M. A., and Çiner, A. (2017). Late Quaternary glaciations in the eastern Mediterranean. In: Hughes, P.D., Woodward, J.C. (Eds.), *Quaternary Glaciation in the Mediterranean Mountains*. Geological Society, London, Special Publications, *433*(1), 289–305. https://doi.org/10.1144/SP433.4

Sarıkaya, M. A., Çiner, A., Haybat, H., and Zreda, M. (2014). An early advance of glaciers on Mount Akdağ, SW Turkey, before the global Last Glacial Maximum; insights from cosmogenic nuclides and glacier modeling. *Quaternary Science Reviews*, *88*, 96–109. https://doi.org/10.1016/j.quascirev.2014.01.016

Sarıkaya, M. A., Çiner, A., and Yıldırım, C. (2017). Cosmogenic ^{36}Cl glacial chronologies of the Late Quaternary glaciers on Mount Geyikdağ in the Eastern Mediterranean. *Quaternary Geochronology*, *39*, 189–204. https://doi.org/10.1016/j.quageo.2017.03.003

Scheidegger, A. E. (1973). On the Prediction of the reach and velocity of catastrophic landslides. *Rock Mechanics and Rock Engineering*, *5*, 231–236. http://dx.doi.org/10.1007/bf01301796

Schemmel, F., Mikes, T., Rojay, B., and Mulch, A. (2013). The impact of topography on isotopes in precipitation across the Central Anatolian Plateau (Turkey). *American Journal of Science*, *313*(2), 61–80. https://doi.org/10.2475/02.2013.01

Schildgen, T. F., Cosentino, D., Bookhagen, B., Niedermann, S., Yıldırım, C., Echtler, H., Wittmann, H., and Strecker, M. R. (2012). Multi-phased uplift of the southern margin of the Central Anatolian plateau, Turkey: A record of tectonic and upper mantle processes. *Earth and Planetary Science Letters*, *317*, 85–95. https://doi.org/10.1016/j.epsl.2011.12.003

Schildgen, T. F., Yıldırım, C., Cosentino, D., and Strecker, M. R. (2014). Linking slab break-off, Hellenic trench retreat, and uplift of the Central and Eastern Anatolian plateaus. *Earth-Science Reviews*, *128*, 147–168. https://doi.org/10.1016/j.earscirev.2013.11.006

Schimmelpfennig, I., Benedetti, L., Finkel, R., Pik, R., Blard, P.-H., Bourles, D., Burnard, P., and Williams, A. (2009). Sources of in-situ ^{36}Cl in basaltic rocks. Implications for calibration of production rates. *Quaternary Geochronology*, *4* (6), 441–461.

Şenel M. (1996). Stratigraphic properties and paleogeographic evaluation of Pirnos Block represents the south margin of the Anamas—Akseki autochthonous; Central Taurus, Turkey (in Turkish). *Geol. Bull. Turk. 39*, 19–29.

Şener, M. F., and Öztürk, M. Z. (2019). Relict drainage effects on distribution and morphometry of karst depressions: A casestudy from central Taurus (Turkey). *Journal of Cave and Karst Studies*, *81*(1), 33–43. https://doi.org/10.4311/2018ES0111

Şengör, A. M. C., and Yazıcı, M. (2020). The aetiology of the neotectonic evolution of Turkey. *Mediterranean Geoscience Reviews*, *2*(3), 327–339. https://doi.org/10.1007/s42990-020-00039-0

Şensoy, S. (2004). The mountains influence on Turkey climate. In: *Balwois Conference on Water Observation and Information System for Decision Support.* Ohrid, Macedonia, pp. 25–29.

Şensoy, S., Demircan, M., and Ulupınar, Y. (2016). Climate of Turkey. Turkish State Meteorological Service, Ankara, Turkey.

Shreve, R. L. (1968). The Blackhawk landslide (Vol. 108). *Geological Society of America.*

Simms, M. J. (2004). Tortoises and hares: Dissolution, erosion and isostasy in landscape evolution. *Earth Surface Processes and Landforms*, *29*(4), 477–494. https://doi.org/10.1002/esp.1047

Şimşek, M., Öztürk, M. Z., and Turoğlu, H. (2019). Geyik Dağı üzerindeki dolin ve uvalaların morfotektonik önemi. *Türk Coğrafya Dergisi, 72*, 13–20. https://doi.org/10.17211/ tcd.501724.

Singeisen, C., Ivy-Ochs, S., Wolter, A., Steinemann, O., Akçar, N., Yesilyurt, S., and Vockenhuber, C. (2020). The Kandersteg rock avalanche (Switzerland): Integrated analysis of a late Holocene catastrophic event. *Landslides*, *17*(6), 1297–1317. https://doi.org/10.1007/s10346-020-01365-y

Small, E. E., Anderson, R. S., Repka. J. L., and Finkel, R. (1997). Erosion rates of alpine bedrock summit surfaces deduced from in situ ^{10}Be and ^{26}Al. *Earth and Planetary Science Letters*, *150*(3-4), 413-425. https://doi.org/10.1016/S0012-821X(97)00092-7

Soldati, M., Corsini, A., and Pasuto, A. (2004). Landslides and climate change in the Italian Dolomites since the Late glacial. *Catena*, *55*(2), 141–161. https://doi.org/10.1016/S0341-8162(03)00113-9

Staubwasser, M., and Weiss, H. (2006). Holocene climate and cultural evolution in Late Prehistoric–Early Historic West Asia. *Quaternary Research*, *66*(3), 372–387. https://doi.org/10.1016/j.yqres.2006.09.001

Stock, G. M., and Uhrhammer, R. A. (2010). Catastrophic rock avalanche 3600 years BP from El Capitan, Yosemite Valley, California. *Earth Surface Processes and Landforms*, *35*(8), 941–951. https://doi.org/10.1002/esp.1982

Stone, J. O. (2000). Air pressure and cosmogenic isotope production. *Journal of Geophysical Research: Solid Earth*, *105*(B10), 23753–23759. https://doi.org/10.1029/2000JB900181

Stone, J. O. H., Allan, G. L., Fifield, L. K., Evans, J. M., and Chivas, A. R. (1994). Limestone erosion measurements with cosmogenic chlorine-36 in calcite - preliminary results from Australia. *Nucl. Instrum. Methods Phys. Res., Sect. B, Beam Interact. Mater. Atoms 92*, 311–316. https://doi.org/10.1016/0168-583X(94)96025-9

Stone, J. O. H., Evans, J. M., Fifield, L. K., Allan, G. L., and Cresswell, R. G. (1998). Cosmogenic Chlorine-36 Production in Calcite by Muons. *Geochimica et Cosmochimica Acta*, *62*(3), 433–454. https://doi.org/10.1016/S0016-7037(97)00369-4

Styllas, M., Dimitriou, E., Gritzalis, K., Koutsodimou, M., Karaouzas, I., Skoulikidis, N., and Gogou, A. (2018). Mid-Holocene changes in the geochemical and biotic conditions of an aquatic ecosystem, in Eastern Mediterranean. In *Annales de Limnologie - International Journal of Limnology*, *54*, 21. https://doi.org/10.1051/limn/2018013

Tan, O., Ceng, M., Tapirdamaz, Z., and Yörük, A. (2008). The earthquake catalogues for Turkey. *Turkish Journal of Earth Sciences*, *17*(2), 405-418

Thomas, F., Godard, V., Bellier, O., Benedetti, L., Ollivier, V., Rizza, M., … and Keddadouche, K. (2018). Limited influence of climatic gradients on the denudation of a Mediterranean carbonate landscape. *Geomorphology*, *316*, 44–58. https://doi.org/10.1016/j.geomorph.2018.04.014

Thomas, F., Godard, V., Bellier, O., Shabanian, E., Ollivier, V., Benedetti, L., … and ASTER Team. (2017). Morphological controls on the dynamics of carbonate landscapes under a mediterranean climate. *Terra Nova*, *29*(3), 173–182. https://doi.org/10.1111/ter.12260

Triantaphyllou, M. V., Ziveri, P., Gogou, A., Marino, G., Lykousis, V., Bouloubassi, I., … and Nunez, N. (2009). Late Glacial–Holocene climate variability at the south-eastern margin of the Aegean Sea. *Marine Geology*, *266*(1–4), 182–197. https://doi.org/10.1016/j.margeo.2009.08.005

TS 699. (2009). *Natural Building Stones - Methods of Inspection and Laboratory Testing.* Institute of Turkish Standards, Türk Standartları Enstitüsü (TSE).

TS EN 1936. (2006). *Natural Stone Test Methods - Determination of Real Density and Apparent Density, and of Total and Open Porosity*. Institute of Turkish Standards, Türk Standartları Enstitüsü (TSE).

Türkeş, M. (1996). Spatial and temporal analysis of annual rainfall variations in Turkey. *International Journal of Climatology: A Journal of the Royal Meteorological Society*, *16*(9), 1057-1076. https://doi.org/10.1002/(SICI)1097-0088(199609)16:9<1057::AID-JOC75>3.0.CO;2-D

von Wartburg, J., Ivy-Ochs, S., Aaron, J., Martin, S., Leith, K., Rigo, M., … and Viganò, A. (2020). Constraining the Age and Source Area of the Molveno landslide Deposits in the Brenta Group, Trentino Dolomites (Italy). *Frontiers in Earth Science*, *8*, 164. https://doi.org/10.3389/feart.2020.00164

Weiss, H., Courty, M.-A., Wetterstrom, W., Guichard, F., Senior, L., Meadow, R., and Curnow, A. (1993). The Genesis and Collapse of Third Millennium North Mesopotamian Civilization. *Science*, *261*(5124), 995–1004. https://doi.org/10.1126/science.261.5124.995

Whipple, K. X. (2009). The influence of climate on the tectonic evolution of mountain belts. *Nature Geoscience*, *2*(2), 97–104. https://doi.org/10.1038/ngeo413

White, W. B. (1984). Rate processes: chemical kinetics and karst landform development. In *Groundwater as a geomorphic agent* (pp. 227–248). Allen & Unwin, London.

White, W. B. (1990). Surface and near-surface karst landforms. Groundwater geomorphology: *Geol. Soc. Am. Special Paper*, *252*, 157-175.

Wick, L., Lemcke, G., and Sturm, M. (2003). Evidence of Lateglacial and Holocene climatic change and human impact in eastern Anatolia: High-resolution pollen, charcoal, isotopic and geochemical records from the laminated sediments of Lake Van, Turkey. *The Holocene*, *13*(5), 665–675. https://doi.org/10.1191/0959683603hl653rp

Wilcken, K. M., Fink, D., Hotchkis, M. A. C., Garton, D., Button, D., Mann, M., … and O'Connor, A. (2017). Accelerator Mass Spectrometry on SIRIUS: New 6 MV spectrometer at ANSTO. *Nuclear Instruments and Methods in Physics Research Section B: Beam Interactions with Materials and Atoms*, *406*, 278–282. https://doi.org/10.1016/j.nimb.2017.01.003

Wilcken, K. M., Fujioka, T., Fink, D., Fülöp, R. H., Codilean, A. T., Simon, K., Mifsud, C., and Kotevski, S. (2019). SIRIUS Performance: ^{10}Be, ^{26}Al and ^{36}Cl measurements at ANSTO. *Nuclear Instruments and Methods in Physics Research Section B: Beam Interactions with Materials and Atoms*, *455*, 300–304. https://doi.org/10.1016/j.nimb.2019.02.009

Willett, S. D. (1999). Orogeny and orography: The effects of erosion on the structure of mountain belts. *Journal of Geophysical Research: Solid Earth*, *104*(B12), 28957–28981. https://doi.org/10.1029/1999JB900248

Wilson, P., Barrows, T. T., Lord, T. C., and Vincent, P. J. (2012). Surface lowering of limestone pavement as determined by cosmogenic (^{36}Cl) analysis. *Earth Surface Processes and Landforms*, *37*(14), 1518–1526. https://doi.org/10.1002/esp.3260

Xu, S., Liu, C., Freeman, S., Lang, Y., Schnabel, C., Tu, C., Wilcken, K., and Zhao, Z. (2013). In-situ cosmogenic ^{36}Cl denudation rates of carbonates in Guizhou karst area. *Chinese Science Bulletin*, *58*(20), 2473–2479. https://doi.org/10.1007/s11434-013-5756-8

Yang, Y., Lang, Y.-C., Xu, S., Liu, C.-Q., Cui, L.-F., Freeman, S. P. H. T., and Wilcken, K. M. (2020). Combined unsteady denudation and climatic gradient factors constrain carbonate landscape evolution: New insights from in situ cosmogenic ^{36}Cl. *Quaternary Geochronology*, *58*, 101075. https://doi.org/10.1016/j.quageo.2020.101075

Yavuz, H., Altindag, R., Sarac, S., Ugur, I., and Sengun, N. (2006). Estimating the index properties of deteriorated carbonate rocks due to freeze–thaw and thermal shock weathering. *International Journal of Rock Mechanics and Mining Sciences*, *43*(5), 767–775. https://doi.org/10.1016/j.ijrmms.2005.12.004

Zerathe, S., Lebourg, T., Braucher, R., and Bourlès, D. (2014). Mid-Holocene cluster of large-scale landslides revealed in the Southwestern Alps by ^{36}Cl dating. Insight on an Alpine-scale landslide activity. *Quaternary Science Reviews*, *90*, 106–127. https://doi.org/10.1016/j.quascirev.2014.02.015

Zerathe, S., Litty, C., Blard, P.-H., Delgado, F., Audin, L., Carcaillet, J. and ASTER Team (2022). Cosmogenic ^{3}He and ^{10}Be denudation rates in the Central Andes: Comparison with a natural sediment trap over the last 18 ka. *Earth and Planetary Science Letters*, *599*, 117869. https://doi.org/10.1016/j.epsl.2022.117869

Url-1 < *http://cronus.cosmogenicnuclides.rocks/2.1/*>, date retrieved 10.09.2020

Url-2 < *http://www.agisoft.com/*>, date retrieved 15. 11.2020

APPENDICES

APPENDIX A: Additional information on ^{36}Cl cosmogenic samples

APPENDIX B: Additional information on Schmidt Hammer measurments

APPENDIX C: Publications from this thesis

APPENDIX A: Additional information on ^{36}Cl cosmogenic samples

Table A. 1 : Major and trace elemens, AMS results, blank and spike data, and corrections to local production rates for denudation samples.

Sample ID	percent35spike	percent37spike	Clspike	mspike	mspikeblank	mdiss	Rm36/35	Rm36/35error	Rm35/37
Definition	relative abundance of 35Cl in the spike	relative abundance of 37Cl in the spike	Cl concentration in spike solution	mass of spike solution	mass of spike solution for blank	mass of sample dissolved for 36Cl extraction	AMS measured 36Cl/35Cl ratio	AMS measured 36Cl/35Cl ratio-error	AMS measured 35Cl/37Cl ratio
Unit	%	%	mg/g	g	g	g	[-]	[-]	[-]
DEN-01	0.95	0.05	1.2218	1.5718	1.0087	37.11	0.00	2.15E-14	8.174317281
DEN-02	0.95	0.05	1.2227	1.3203	1.0087	40.29	1.10E-12	4.29E-14	6.195280954
DEN-03	0.95	0.05	1.2227	1.3236	1.0087	39.46	4.28E-12	1.60E-13	9.379640226
DEN-04	0.95	0.05	1.2227	1.3397	1.0087	38.44	4.54E-12	1.71E-13	8.425972255
DEN-05	0.95	0.05	1.2236	1.0910	1.0087	37.94	3.68E-12	1.38E-13	5.996735494
DEN-06	0.94	0.06	1.1616	1.0072	1.0087	38.36	5.90E-12	2.25E-13	8.655388344
DEN-07	0.95	0.05	1.2236	1.0169	1.0087	34.91	5.95E-12	2.24E-13	13.33161175
DEN-08	0.95	0.05	1.2236	1.1623	1.0087	36.67	9.00E-12	3.39E-13	14.63426299
DEN-09	0.95	0.05	1.2236	1.0942	1.0087	35.29	8.87E-12	3.32E-13	13.63282206
DEN-10	0.95	0.05	1.2236	1.0912	1.0087	31.59	5.95E-12	2.23E-13	13.39762923
DEN-11	0.95	0.05	1.2236	1.0427	1.0087	34.94	1.48E-11	6.50E-13	10.17342002
DEN-12	0.94	0.06	1.1616	0.9977	1.0087	39.41	8.72E-12	3.33E-13	6.118300355
DEN-13	0.94	0.06	1.1616	1.0110	1.0087	38.90	6.89E-12	2.73E-13	9.077641535
BLANK-C25	0.94	0.06	1.1616	1.0087					

Table A. 1 (continued) : Major and trace elemens, AMS results, blank and spike data, and corrections to local production rates for denudation samples.

Rm35/37error	Rm36/35blank	Rm36/35blankerror	Rm35/37blank	Rm35/37blankerror	Percent of Total Production			Attenuation length	Contemporary depth average production rate (Marrero et al., 2016)	
AMS measured 35Cl/37Cl ratio-error	AMS measured 36Cl/35Cl ratio-blank	AMS measured 36Cl/35Cl ratio-blank-error	AMS measured 35Cl/37Cl ratio-blank	AMS measured 35Cl/37Cl ratio-blank-error	Ca (sp. + muons)	K (sp. + muons)	Cl (neutron cap.)	(calculated)	Ca, spallation	K, spallation
[-]	[-]	[-]	[-]	[-]	%	%	%	g cm-2	atoms/g/yr	atoms/g/yr
0.132169045	4.8793E-14	7.31582E-15	16.19230096	0.16975698	94.21	0.1941	5.589	155.1837	22.6012	0.046531
0.108384026	4.8793E-14	7.31582E-15	16.19230096	0.16975698	93.19	0.1668	6.64	154.5527	24.6598	0.044098
0.189793737	4.8793E-14	7.31582E-15	16.19230096	0.16975698	97.31	0.05682	2.631	156.0953	54.3724	0.03168
0.159537967	4.8793E-14	7.31582E-15	16.19230096	0.16975698	96.55	0.05733	3.384	157.0184	65.2223	0.038632
0.09954019	4.8793E-14	7.31582E-15	16.19230096	0.16975698	93.26	0.5568	6.176	157.6921	68.286	0.40674
0.124011259	4.8793E-14	7.31582E-15	16.19230096	0.16975698	97.93	0.05821	2.008	158.5608	76.5468	0.045391
0.139217954	4.8793E-14	7.31582E-15	16.19230096	0.16975698	99.16	0.1788	0.6494	157.6935	60.8404	0.10948
0.145745782	4.8793E-14	7.31582E-15	16.19230096	0.16975698	99.47	0.05896	0.457	157.4323	59.5767	0.035231
0.166863892	4.8793E-14	7.31582E-15	16.19230096	0.16975698	99.33	0.05973	0.6095	157.1861	54.9864	0.032996
0.153131144	4.8793E-14	7.31582E-15	16.19230096	0.16975698	99.15	0.1168	0.724	156.9904	55.0263	0.064705
0.372548713	4.8793E-14	7.31582E-15	16.19230096	0.16975698	97.87	0.1751	1.95	156.0099	42.7329	0.076298
0.097616012	4.8793E-14	7.31582E-15	16.19230096	0.16975698	95.37	0.05544	4.571	155.5215	39.5978	0.022976
0.107431275	4.8793E-14	7.31582E-15	16.19230096	0.16975698	98.17	0.0564	1.768	155.1843	40.2405	0.023075

Table A. 1 (continued) : Major and trace elemens, AMS results, blank and spike data, and corrections to local production rates for denudation samples.

Contemporary depth average production rate (Marrero et al., 2016)					Scalling factors	Ca	K	Fe	Ti	Fast	Slow	Cl	Cl
Fe, spallation	Ti, spallation	Ca, muons	K, muons	Cl, low energy	Lal/Stone, Time-independent Lal (1991); Stone (2000)	spallation	spallation	spallation	spallation	muons	muons	epithermal	thermal
atoms/g/yr	atoms/g/yr	atoms/g/yr	atoms/g/yr	atoms/g/yr		[-]	[-]	[-]	[-]	[-]	[-]	[-]	[-]
0.0022578	0.00038947	1.0432	0.002197	1.4028	ST	1.6887	1.6887	1.6887	1.6887	1.2027	1.2027	1.6887	1.6887
0.0014058	0.00036672	1.1153	0.0020312	1.8367	ST	1.5885	1.5885	1.5885	1.5885	1.1332	1.1332	1.5885	1.5885
0.0028679	0.00082874	1.7921	0.0011169	1.5184	ST	3.3138	3.3138	3.3138	3.3138	1.8652	1.8652	3.3138	3.3138
0.0030868	0.001026	2.0082	0.0012841	2.3566	ST	4.0531	4.0531	4.0531	4.0531	2.1662	2.1662	4.0531	4.0531
0.0060446	0.0010869	2.1074	0.013556	4.6615	ST	4.2742	4.2742	4.2742	4.2742	2.2696	2.2696	4.2742	4.2742
0.0025059	0.0012261	2.3021	0.0014794	1.6166	ST	4.7884	4.7884	4.7884	4.7884	2.4825	2.4825	4.7884	4.7884
0.0068533	0.0009704	1.9738	0.0038112	0.41138	ST	3.8718	3.8718	3.8718	3.8718	2.124	2.124	3.8718	3.8718
0.0046955	0.00093387	1.9516	0.0012368	0.2827	ST	3.7603	3.7603	3.7603	3.7603	2.0739	2.0739	3.7603	3.7603
0.0017422	0.0008699	1.8405	0.0011794	0.34871	ST	3.4838	3.4838	3.4838	3.4838	1.9636	1.9636	3.4838	3.4838
0.0034007	0.00085103	1.8479	0.0023191	0.41527	ST	3.4142	3.4142	3.4142	3.4142	1.9302	1.9302	3.4142	3.4142
0.002912	0.001315	1.5674	0.0029515	0.8828	ST	2.718	2.718	2.718	2.718	1.6333	1.6333	2.718	2.718
0.0014383	0.00058892	1.4961	0.00091018	1.9694	ST	2.4215	2.4215	2.4215	2.4215	1.5024	1.5024	2.4215	2.4215
0.0011496	0.00059068	1.501	0.00090387	0.75157	ST	2.4166	2.4166	2.4166	2.4166	1.4915	1.4915	2.4166	2.4166

Table A. 2 : Major and trace elemens, AMS results, blank and spike data, and corrections to local production rates for the rock avalanche samples.

Sample ID	percent35spike	percent37spike	Clspike	mspike	mspikeblank	mdiss	Rm36/35	Rm36/35error	Rm35/37
	relative abundance of ^{35}Cl in the spike	relative abundance of ^{37}Cl in the spike	Cl concentration in spike solution	mass of spike solution	mass of spike solution for blank	mass of sample dissolved for 36Cl extraction	AMS measured $^{36}Cl/^{35}Cl$ ratio	AMS measured $^{36}Cl/^{35}Cl$ ratio-error	AMS measured $^{35}Cl/^{37}Cl$ ratio
Unit	%	%	mg/g	g	g	g	[-]	[-]	[-]
RF19-01	0.9526	0.0474	1.2236	1.1182	1.0087	35.34	5.97E-13	2.21E-14	9.0387
RF19-02	0.9449	0.0551	1.1616	1.088	1.0087	35.55	6.11E-13	2.38E-14	8.7184
RF19-03	0.9449	0.0551	1.1616	1.1386	1.0087	36.42	5.70E-13	2.21E-14	8.2291
RF19-04	0.9449	0.0551	1.1616	1.0985	1.0087	35.43	1.48E-12	5.47E-14	8.6580
RF19-05	0.9449	0.0551	1.1616	1.1105	1.0087	36.6	2.29E-12	8.59E-14	6.6754
RF19-06	0.9449	0.0551	1.1616	1.1028	1.0087	37.68	4.83E-13	2.10E-14	7.5329
RF19-07	0.9449	0.0551	1.1616	1.1071	1.0087	36.55	5.44E-13	2.11E-14	9.6275
RF19-08	0.9449	0.0551	1.1616	1.1261	1.0087	37.22	4.64E-13	1.78E-14	6.9368
BLANK-C25	0.9449	0.0551	1.1616	1.0087	1.0087	NA	4.88E-14	7.32E-15	16.1923

Table A. 2 (continued) : Major and trace elemens, AMS results, blank and spike data, and corrections to local production rates for the rock avalanche samples.

Rm35/37error	Rm36/35blank	Rm36/35blankerror	Rm35/37blank	Rm35/37blankerror	Percent of Total Production			Attenuation length
AMS measured $^{35}Cl/^{37}Cl$ ratio-error	AMS measured 36Cl/35Cl ratio-blank	AMS measured 36Cl/35Cl ratio-blank-error	AMS measured $^{35}Cl/^{37}Cl$ ratio-blank	AMS measured 35Cl/37Cl ratio-blank-error	Ca (sp. + muons)	K (sp. + muons)	Cl (neutron cap.)	(calculated)
[-]	[-]	[-]	[-]	[-]	%	%	%	g cm-2
0.3518	4.879E-14	7.316E-15	1.619E+01	1.698E-01	97.1	0.2	2.7	157.9
0.1853	4.879E-14	7.316E-15	1.619E+01	1.698E-01	97.5	0.1	2.4	157.9
0.1690	4.879E-14	7.316E-15	1.619E+01	1.698E-01	96.8	0.1	3.1	157.9
0.1604	4.879E-14	7.316E-15	1.619E+01	1.698E-01	97.4	0.1	2.5	157.9
0.1588	4.879E-14	7.316E-15	1.619E+01	1.698E-01	95.3	0.2	4.5	157.9
0.1100	4.879E-14	7.316E-15	1.619E+01	1.698E-01	96.3	0.4	3.3	157.8
0.1170	4.879E-14	7.316E-15	1.619E+01	1.698E-01	98.2	0.1	1.8	157.9
0.1059	4.879E-14	7.316E-15	1.619E+01	1.698E-01	95.2	0.6	4.2	157.9
0.1698	NA	NA	NA	NA				

Table A. 2 (continued) : Major and trace elemens, AMS results, blank and spike data, and corrections to local production rates for the rock avalanche samples.

Contemporary depth average production rate (Marrero et al., 2016)							Scalling factor	Ca,	K	Fe	Ti	Fast	Slow	Cl	Cl
Ca spallation	K spallation	Fe spallation	Ti spallation	Ca muons	K muons	Cl, low energy	Lal-Stone (Lal, 1991; Stone, 2000)	spallation	spallation	spallation	spallation	muons	muons	epithermal	thermal
[atoms/g/yr]								[-]	[-]	[-]	[-]	[-]	[-]	[-]	[-]
91.9	0.2	0.0	0.0	2.2	0.0	2.6	ST	4.6135	4.6135	4.6135	4.6135	2.4008	2.4008	4.6135	4.6135
93.1	0.1	0.0	0.0	2.2	0.0	2.3	ST	4.6197	4.6197	4.6197	4.6197	2.4032	2.4032	4.6197	4.6197
91.0	0.1	0.0	0.0	2.2	0.0	3.0	ST	4.5679	4.5679	4.5679	4.5679	2.3831	2.3831	4.5679	4.5679
91.5	0.1	0.0	0.0	2.2	0.0	2.4	ST	4.5256	4.5256	4.5256	4.5256	2.3668	2.3668	4.5256	4.5256
91.5	0.2	0.0	0.0	2.2	0.0	4.5	ST	4.5106	4.5106	4.5106	4.5106	2.361	2.361	4.5106	4.5106
89.9	0.3	0.0	0.0	2.2	0.0	3.2	ST	4.4927	4.4927	4.4927	4.4927	2.354	2.354	4.4927	4.4927
92.2	0.1	0.0	0.0	2.2	0.0	1.7	ST	4.5167	4.5167	4.5167	4.5167	2.3633	2.3633	4.5167	4.5167
89.6	0.5	0.0	0.0	2.2	0.0	4.1	ST	4.5167	4.5167	4.5167	4.5167	2.3633	2.3633	4.5167	4.5167

Table A. 3 : Compilation of ^{36}Cl-derived denudation rates for carbonate bedrock samples in the previous studies.

#	Reference	Type	Name	latitude	longitude	elevation	Precipitation	Denudation rate		
			-	dd	dd	m	mm	mm/kyr		
1	This study	bedrock- flat	DEN-01	36.32714	30.39047	770	676.00	45.77	±	3.91
2	This study	bedrock- flat	DEN-02	37.26044	30.73323	675	611.00	22.35	±	2.31
3	This study	bedrock- flat	DEN-03	38.26791	30.73365	1630	586.00	11.72	±	1.17
4	This study	bedrock- flat	DEN-04	37.78375	31.24911	1935	630.00	12.49	±	1.25
5	This study	bedrock- flat	DEN-05	36.96748	31.92970	2040	693.00	17.32	±	1.83
6	This study	bedrock- flat	DEN-06	36.34117	32.58952	2230	769.00	19.00	±	1.81
7	This study	bedrock- flat	DEN-07	36.42975	32.71398	1910	730.00	18.70	±	1.89
8	This study	bedrock- flat	DEN-08	36.69687	32.83882	1860	656.00	7.33	±	0.82
9	This study	bedrock- flat	DEN-09	36.68194	32.94462	1750	636.00	7.30	±	0.82
10	This study	bedrock- flat	DEN-10	36.89926	33.31964	1715	548.00	12.42	±	1.31
11	This study	bedrock- flat	DEN-11	37.30657	33.81848	1385	424.00	1.92	±	0.31
12	This study	bedrock- flat	DEN-12	37.51569	33.16922	1224	405.00	3.88	±	0.5
13	This study	bedrock- flat	DEN-13	38.13348	32.73594	1205	436.00	6.93	±	0.75
14	Krklec et al. (2022)	bedrock- flat	SJ-C1	43.7642	16.0026	200	1050.00	19.91	±	0.86
15	Krklec et al. (2022)	bedrock- flat	SJ-C2	43.7642	16.0026	200	1050.00	19.03	±	0.86
16	Krklec et al. (2022)	bedrock- flat	SJ-C3	43.7642	16.0026	200	1050.00	14.78	±	0.61
17	Krklec et al. (2022)	bedrock- flat	SJ-C4	43.7642	16.0026	200	1050.00	22.65	±	0.99
18	Krklec et al. (2022)	bedrock- flat	SJ-C5	43.7642	16.0026	200	1050.00	14.74	±	0.62
19	Krklec et al. (2022)	bedrock- flat	SJ-C6	43.7642	16.0026	200	1050.00	21.72	±	0.97
20	Krklec et al. (2022)	bedrock- flat	SJ-C7	43.7642	16.0026	200	1050.00	22.76	±	0.97
21	Krklec et al. (2022)	bedrock- flat	SJ-C8	43.7642	16.0026	200	1050.00	18.26	±	0.78
22	Krklec et al. (2022)	bedrock- flat	SJ-C9	43.7642	16.0026	200	1050.00	17.75	±	0.76
23	Krklec et al. (2022)	bedrock- flat	SJ-C10	43.7642	16.0026	200	1050.00	17.50	±	0.74
29	Ben-Asher et al. (2021)	bedrock- flat [soil covered]	G 0	31.361882	34.82886	398	250.00	30.00		
30	Ben-Asher et al. (2021)	bedrock- flat [soil covered]	Ga 36	31.361882	34.82886	398	250.00	5.00		
31	Ben-Asher et al. (2021)	bedrock- flat [soil covered]	GA 51	31.361882	34.82886	398	250.00	4.00		
32	Ben-Asher et al. (2021)	bedrock- flat [soil covered]	GA 73	31.361882	34.82886	398	250.00	6.00		
33	Ben-Asher et al. (2021)	bedrock-hillslope [soil covered]	GA82	31.361882	34.82886	398	250.00	5.00		
34	Ben-Asher et al. (2021)	Bedrock-flat	GA1	31.361882	34.82886	398	250.00	19.00		
35	Ben-Asher et al. (2021)	bedrock- flat [soil covered]	GB 1	31.361882	34.82886	398	250.00	13.00		
36	Ben-Asher et al. (2021)	bedrock- flat [soil covered]	RMA 1	32.56012	35.119455	241	650.00	67.00		
37	Ben-Asher et al. (2021)	bedrock- flat [soil covered]	RMA 4	32.56012	35.119455	241	650.00	74.00		
38	Ben-Asher et al. (2021)	bedrock-hillslope [soil covered]	RMD	32.56012	35.119455	241	650.00	97.00		
39	Ben-Asher et al. (2021)	bedrock- flat [soil covered]	ZTA 1	33.001956	35.485523	776	800.00	210.00		
40	Ben-Asher et al. (2021)	bedrock- flat [soil covered]	ZTA 2	33.001956	35.485523	776	800.00	173.00		
41	Ben-Asher et al. (2021)	bedrock- flat [soil covered]	ZTA 3	33.001956	35.485523	776	800.00	180.00		
42	Ben-Asher et al. (2021)	bedrock- flat [soil covered]	GLA 1	32.530407	35.36435	232	450.00	24.00		
43	Ben-Asher et al. (2021)	Bedrock-flat	GLA4	32.530407	35.36435	232	450.00	21.00		
44	Ben-Asher et al. (2021)	bedrock-downslope [soil covered]	GLB	32.530407	35.36435	232	450.00	13.00		

Table A. 3 (continued) : Compilation of ^{36}Cl-derived denudation rates for carbonate bedrock samples in the previous studies.

#	Reference	Type	Name	latitude	longitude	elevation	Precipitation	Denudation rate		
			-	dd	dd	m	mm	mm/kyr		
45	Ben-Asher et al. (2021)	Bedrock-flat	UB15			510	550.00	15.00		
46	Ben-Asher et al. (2021)	Bedrock-flat	UB19			510	550.00	14.00		
47	Ben-Asher et al. (2021)	Bedrock-flat	MEA4	32.984762	35.3956379	910	900.00	121.00		
48	Ben-Asher et al. (2021)	Bedrock-downslope	MEB	32.984762	35.3956379	910	900.00	123.00		
24	Yang et al. (2020)	bedrock- flat	GZ01	106.52	26.4	1235	1105.00	51.40	±	5
25	Yang et al. (2020)	bedrock- slope	BJ01	115.93	39.78	310	539.00	53.60	±	6.7
26	Yang et al. (2020)	bedrock- slope	BJ02	115.93	39.78	310	539.00	51.90	±	5.3
27	Yang et al. (2020)	bedrock- flat	GS02	103.83	35.88	2100	372.00	17.40	±	2
28	Yang et al. (2020)	bedrock- flat	GS03	103.22	36.83	2300	320.00	7.00	±	0.7
49	Avni et al. (2019)	Bedrock-flat	MS-1br	33.319	35.805	2200	1510.00	11.00	±	3
50	Avni et al. (2019)	Bedrock-flat	MS-2br	33.317	35.8	2170	1525.00	17.00	±	4
51	Avni et al. (2019)	Bedrock-flat [enclosed karst]	MS-3br	33.311	35.797	1950	1550.00	21.00	±	4
52	Avni et al. (2019)	Bedrock-flat [enclosed karst]	MS-4br	33.31	35.798	1960	1550.00	59.00	±	11
53	Avni et al. (2019)	Bedrock-flat	MS-5br	33.303	35.793	2070	1515.00	17.00	±	4
54	Avni et al. (2019)	Bedrock-hillslope	MS-6br	33.311	35.794	2000	1540.00	27.00	±	6
55	Avni et al. (2019)	Bedrock-flat	MS-7br	33.318	35.782	1980	1495.00	30.00	±	6
56	Avni et al. (2019)	Bedrock-flat	MS-8br	33.306	35.779	1930	1430.00	26.00	±	5
57	Avni et al. (2019)	Bedrock-hillslope	MS-9br	33.298	35.783	1930	1395.00	14.00	±	3
58	Avni et al. (2019)	Bedrock-flat	MS-10br	33.309	35.758	1700	1290.00	23.00	±	5
59	Avni et al. (2019)	Bedrock-hillslope	AR-1br	33.297	35.757	1420	1255.00	85.00	±	16
60	Avni et al. (2019)	Bedrock-hillslope	AR-2br	33.297	35.757	1429	1260.00	118.00	±	25
61	Avni et al. (2019)	Bedrock-hillslope	AR-3br	33.298	35.756	1500	1245.00	78.00	±	15
62	Avni et al. (2019)	Bedrock-hillslope	AR-4br	33.299	35.755	1555	1260.00	130.00	±	23
63	Avni et al. (2019)	Bedrock-hillslope	AR-5br	33.3	35.755	1568	1240.00	61.00	±	12
64	Avni et al. (2019)	Bedrock-flat	AR-6br	33.301	35.755	1615	1240.00	45.00	±	9
65	Avni et al. (2019)	Bedrock-flat	AR-7br	33.301	35.753	1633	1220.00	40.00	±	8
66	Avni et al. (2019)	Bedrock-flat	SN-1br	33.286	35.734	1411	1170.00	58.00	±	10
67	Avni et al. (2019)	Bedrock-flat	SN-2br	33.286	35.732	1388	1165.00	39.00	±	8
68	Avni et al. (2019)	Bedrock-flat	SN-3br	33.286	35.732	1390	1160.00	42.00	±	9
69	Avni et al. (2019)	Bedrock-hillslope	SN-4br	33.287	35.731	1350	1160.00	36.00	±	8
70	Avni et al. (2019)	Bedrock-hillslope	SN-5br	33.287	35.728	1247	1135.00	60.00	±	12
71	Avni et al. (2019)	Bedrock-hillslope	SN-6br	33.29	35.725	1105	1075.00	63.00	±	12
72	Avni et al. (2019)	Bedrock-hillslope	SN-7br	33.293	35.723	955	1055.00	48.00	±	10
73	Avni et al. (2019)	Bedrock-hillslope	SN-9br	33.292	35.722	940	1050.00	81.00	±	16

Table A. 3 (continued) : Compilation of ^{36}Cl-derived denudation rates for carbonate bedrock samples in the previous studies.

#	Reference	Type	Name	latitude	longitude	elevation	Precipitation	Denudation rate		
			-	dd	dd	m	mm	mm/kyr		
74	Avni et al. (2019)	Bedrock-flat	SNA-1br	33.274	35.722	1140	1030.00	39.00	±	8
75	Avni et al. (2019)	Bedrock-flat [soil-covered]	SNA-2sbr	33.274	35.722	1140	1030.00	48.00	±	9
76	Avni et al. (2019)	Bedrock-flat	SNA-5br	33.273	35.712	1077	985.00	29.00	±	6
77	Avni et al. (2019)	Bedrock-hillslope	SNA-6br	33.269	35.706	918	905.00	32.00	±	7
78	Avni et al. (2019)	Bedrock-hillslope	SNA-7br	33.267	35.705	815	875.00	34.00	±	7
79	Avni et al. (2019)	Bedrock-hillslope	SNA-8br	33.261	35.7	720	810.00	36.00	±	7
80	Avni et al. (2019)	Bedrock-hillslope	SNA-9br	33.257	35.696	550	740.00	20.00	±	5
81	Avni et al. (2019)	Bedrock-hillslope	SNA-10br	33.256	35.693	428	685.00	16.00	±	4
82	Avni et al. (2019)	Bedrock-hillslope	SNA-11br	33.255	36.692	400	665.00	11.00	±	3
83	Avni et al. (2019)	Bedrock-hillslope [soil-covered]	SNA-12sbr	33.255	36.692	400	665.00	19.00	±	4
84	Marrero et al. (2018)	Bedrock-flat	MH12-68	−80.30576	−82.11405	1681		0.27	±	0.18
85	Marrero et al. (2018)	Bedrock-flat	MH12-30A	−80.26309	−82.18705	1381		0.08	±	0.19
86	Marrero et al. (2018)	Bedrock-flat	MH12-30B	−80.26309	−82.18705	1381		0.26	±	0.18
87	Marrero et al. (2018)	Bedrock-flat	MH12-31	−80.26309	−82.18705	1381		0.23	±	0.19
88	Marrero et al. (2018)	Bedrock-flat	MH12-32	−80.26309	−82.18705	1381		0.16	±	0.22
89	Marrero et al. (2018)	Bedrock-flat	MH12-C1-TO	−80.26334	−82.18677	1393		0.25	±	0.21
90	Marrero et al. (2018)	Bedrock-flat	MH14-13	−80.2642	−82.18933	1343		0.50	±	0.21
91	Marrero et al. (2018)	Bedrock-flat	MH14-31	−80.26735	−82.21628	1273		0.38	±	0.2
92	Marrero et al. (2018)	Bedrock-flat	MH12-75	−80.27371	−82.10712	1163		0.59	±	0.21
93	Marrero et al. (2018)	Bedrock-flat	MH14-15	−80.26105	−82.10672	1102		2.08	±	0.37
94	Marrero et al. (2018)	Bedrock-flat	MH14-38	−80.29905	−82.00345	826		8.40	±	1
95	Marrero et al. (2018)	Bedrock-flat	MH14-21	−82.097926	−80.28305	746		10.90	±	1.3
96	Marrero et al. (2018)	Bedrock-flat	MH14-37	−80.2794	−82.02958	809		99.00	±	10
97	Thomas et al. (2018)	Bedrock-flat	NE2	43.341	5.2403	211	558.00	29.00	±	3.1
98	Thomas et al. (2018)	Bedrock-flat	NE3	43.3562	5.1596	163	541.00	18.60	±	2
99	Thomas et al. (2018)	Bedrock-flat	CA1	43.22	5.4363	230	573.00	34.40	±	3.6
100	Thomas et al. (2018)	Bedrock-flat	CA3	43.2321	5.4638	382	652.00	35.40	±	3.8
101	Thomas et al. (2018)	Bedrock-flat	AL1	43.7561	5.0245	260	668.00	21.60	±	2.3
102	Thomas et al. (2018)	Bedrock-flat	AL4	43.762	5.0318	240	657.00	35.80	±	4
103	Thomas et al. (2018)	Bedrock-flat	SB2	43.3187	5.7332	984	827.00	50.60	±	5.5
104	Thomas et al. (2018)	Bedrock-flat	SB5	43.3143	5.6979	997	927.00	34.20	±	3.6
105	Thomas et al. (2018)	Bedrock-flat	SB7	43.3189	5.6823	865	860.00	39.40	±	4.3
106	Thomas et al. (2018)	Bedrock-flat	GL1	43.8192	5.5158	1051	1004.00	85.50	±	9.4
107	Thomas et al. (2018)	Bedrock-flat	GL3	43.8196	5.5277	1049	1008.00	116.50	±	12.9

Table A. 3 (continued) : Compilation of ^{36}Cl-derived denudation rates for carbonate bedrock samples in the previous studies.

#	Reference	Type	Name	latitude	longitude	elevation	Precipitation	Denudation rate		
			-	dd	dd	m	mm	mm/kyr		
108	Thomas et al. (2018)	Bedrock-flat	GL4	43.8182	5.5361	1032	944.00	54.60	±	5.9
109	Thomas et al. (2018)	Bedrock-flat	LF1	43.5625	5.211	219	580.00	30.50	±	3.3
110	Thomas et al. (2018)	Bedrock-flat	LF2	43.5613	5.1963	192	562.00	41.70	±	4.5
111	Thomas et al. (2018)	Bedrock-flat	CO1	43.6937	5.2725	477	709.00	23.80	±	2.5
112	Thomas et al. (2018)	Bedrock-flat	VE1	44.1743	5.2678	1835	1484.00	48.90	±	5.2
113	Thomas et al. (2018)	Bedrock-flat	VE2	44.174	5.2633	1838	1434.00	27.00	±	2.9
114	Thomas et al. (2018)	Bedrock-flat	VE4	44.173	5.2749	1851	1484.00	35.70	±	3.8
115	Thomas et al. (2018)	Bedrock-flat	VE5	44.1851	5.2604	1440	1206.00	35.50	±	3.8
116	Thomas et al. (2018)	Bedrock-flat	LU1	44.1225	5.7853	1725	1377.00	119.10	±	13.3
117	Thomas et al. (2018)	Bedrock-flat	LU2	44.1231	5.7887	1751	1377.00	111.10	±	12.4
118	Thomas et al. (2018)	Bedrock-flat	LU3	44.1232	5.8	1795	1410.00	141.40	±	15.9
119	Thomas et al. (2018)	Bedrock-flat	SV1	43.5321	5.6182	1012	822.00	26.50	±	2.7
120	Thomas et al. (2018)	Bedrock-flat	SV3	43.531	5.6081	1004	947.00	22.30	±	2.3
121	Thomas et al. (2018)	Bedrock-flat	SV4	43.5391	5.6463	1000	927.00	40.30	±	4.2
122	Thomas et al. (2017)	Bedrock-flat	PLCR-01B	43.8038	5.2871	653	700.00	26.50	±	3.1
123	Thomas et al. (2017)	Bedrock-flat	PLCR-02B	43.8035	5.2888	644	700.00	30.10	±	3.4
124	Thomas et al. (2017)	Bedrock-flat	PLCR-03B	43.7965	5.231	660	700.00	33.70	±	4
125	Thomas et al. (2017)	Bedrock-flat	PLCR-08B	43.796	5.2426	659	700.00	30.80	±	3.4
126	Thomas et al. (2017)	Bedrock-flat	PHA01C-B	43.7663	5.1856	384	700.00	29.20	±	3.3
127	Thomas et al. (2017)	Bedrock-flat	PHA02C-B	43.765	5.1931	374	700.00	31.80	±	3.9
128	Thomas et al. (2017)	Bedrock-flat	VID03C-B	43.8002	5.125	548	700.00	39.80	±	5.7
129	Godard et al.(2016)	Bedrock-flat		43.8059	5.1516	706	750.00	60.20	±	6.3
130	Godard et al.(2016)	Bedrock-flat		43.8143	5.1421	707	750.00	69.10	±	7.2
131	Godard et al.(2016)	Bedrock-flat		43.8163	5.1407	694	750.00	74.60	±	7.8
132	Godard et al.(2016)	Bedrock-flat		43.8111	5.1508	672	750.00	67.70	±	7.1
133	Godard et al.(2016)	Bedrock-flat		43.814	5.1422	687	750.00	47.60	±	4.9
134	Godard et al.(2016)	Bedrock-flat		43.8095	5.1768	680	750.00	42.60	±	4.4
135	Godard et al.(2016)	Bedrock-flat		43.8092	5.1744	622	750.00	71.10	±	7.4
136	Godard et al.(2016)	Bedrock-flat		43.8082	5.1724	624	750.00	52.90	±	5.5
137	Godard et al.(2016)	Bedrock-flat		43.8091	5.1719	625	750.00	60.40	±	6.4
138	Godard et al.(2016)	Bedrock-flat		43.8084	5.1582	663	750.00	64.10	±	6.7
139	Godard et al.(2016)	Bedrock-flat		43.797	5.231	660	750.00	30.90	±	3.7
140	Ryb et al. (2014a)	Bedrock-hillslope	AR1	31.6376	35.1366	947	581.50	23.00	±	1.4
141	Ryb et al. (2014a)	Bedrock-hillslope	AR2	31.6382	35.1363	960	580.70	13.60	±	0.8

Table A. 3 (continued) : Compilation of ^{36}Cl-derived denudation rates for carbonate bedrock samples in the previous studies.

#	Reference	Type	Name	latitude	longitude	elevation	Precipitation	Denudation rate		
			-	dd	dd	m	mm	mm/kyr		
142	Ryb et al. (2014a)	Bedrock-hillslope	AR4	31.6377	35.1354	948	583.00	11.60	±	0.7
143	Ryb et al. (2014a)	Bedrock-hillslope	AR5	31.6375	35.1342	921	585.70	15.20	±	0.9
144	Ryb et al. (2014a)	Bedrock-hillslope	AR6	31.6365	35.1327	888	589.80	21.30	±	1.4
145	Ryb et al. (2014a)	Bedrock-flat [interfluve]	AR7	31.6476	35.1817	865	373.00	10.30	±	0.3
146	Ryb et al. (2014a)	Bedrock-flat [interfluve]	AR9	31.6034	35.2151	819	181.40	8.60	±	0.5
147	Ryb et al. (2014a)	Bedrock-hillslope	AR11	31.605	35.211	626	194.60	32.60	±	2
148	Ryb et al. (2014a)	Bedrock-hillslope	AR12	31.6048	35.2116	664	192.70	8.40	±	0.5
149	Ryb et al. (2014a)	Bedrock-hillslope	AR13	31.6046	35.2121	710	190.90	7.20	±	0.5
150	Ryb et al. (2014a)	Bedrock-hillslope	AR14	31.6041	35.2135	762	186.50	12.10	±	0.8
151	Ryb et al. (2014a)	Bedrock-hillslope	AR15	31.6039	35.2143	795	183.90	12.10	±	0.8
152	Ryb et al. (2014a)	Bedrock-flat [interfluve]	AR16	31.6021	35.226	769	153.00	2.30	±	0.1
153	Ryb et al. (2014a)	Bedrock-flat [interfluve]	AR18	31.5864	35.2283	717	153.20	6.40	±	0.4
154	Ryb et al. (2014a)	Bedrock-flat [interfluve]	AR19	31.5836	35.1998	874	272.10	9.00	±	0.6
155	Ryb et al. (2014a)	Bedrock-flat [interfluve]	AR21	31.5817	35.2057	837	232.30	4.00	±	0.2
156	Ryb et al. (2014a)	Bedrock-flat [interfluve]	AR23	31.577	35.2158	776	182.00	4.50	±	0.3
157	Ryb et al. (2014a)	Bedrock-flat [interfluve]	AR24	31.5702	35.2201	711	172.70	5.50	±	0.3
158	Ryb et al. (2014a)	Bedrock-flat [interfluve]	AR25	31.5569	35.2261	606	161.40	5.60	±	0.3
159	Ryb et al. (2014a)	Bedrock-hillslope	AR26	31.5567	35.2247	560	163.70	12.60	±	0.7
160	Ryb et al. (2014a)	Bedrock-hillslope	AR27	31.5564	35.2241	544	165.10	8.40	±	0.5
161	Ryb et al. (2014a)	Bedrock-hillslope	AR28	31.5562	35.2237	513	165.60	13.70	±	0.8
162	Ryb et al. (2014a)	Bedrock-flat [interfluve]	AR30	31.5533	35.2331	501	150.70	5.90	±	0.3
163	Ryb et al. (2014a)	Bedrock-flat [interfluve]	AR31	31.4644	35.3771	182	52.60	2.40	±	0.1
164	Ryb et al. (2014a)	Bedrock-flat [interfluve]	AR32	31.4648	35.3765	172	53.10	3.30	±	0.2
165	Ryb et al. (2014a)	Bedrock-flat [interfluve]	AR33	31.465	35.3766	173	53.10	2.70	±	0.1
166	Ryb et al. (2014a)	Bedrock-flat [interfluve]	AR38	31.4436	35.3661	218	53.10	1.40	±	0.1
167	Ryb et al. (2014a)	Bedrock-flat [interfluve]	AR39	31.4443	35.3659	210	53.50	0.90	±	0.05
168	Ryb et al. (2014a)	Bedrock-flat [interfluve]	AR40	31.4719	35.2918	338	105.90	11.00	±	0.6
169	Ryb et al. (2014a)	Bedrock-flat [interfluve]	AR41	31.4826	35.3107	319	100.00	2.30	±	0.1
170	Ryb et al. (2014a)	Bedrock-hillslope	AR42	31.4823	35.3114	284	99.90	19.10	±	1.1
171	Ryb et al. (2014a)	Bedrock-hillslope	AR43	31.4824	35.3118	241	99.80	38.00	±	2.3
172	Ryb et al. (2014a)	Bedrock-hillslope	AR44	31.4825	35.3122	220	99.80	22.30	±	1.3
173	Ryb et al. (2014a)	Bedrock-hillslope	AR45	31.4827	35.3125	200	99.70	34.70	±	2.1
174	Ryb et al. (2014b)	Bedrock-hillslope	SQ1	31.7714	35.0818	789	587.00	46.00	±	4.6
175	Ryb et al. (2014b)	Bedrock-hillslope	SQ2	31.7693	35.0731	701	582.00	43.00	±	4.3

Table A. 3 (continued) : Compilation of ^{36}Cl-derived denudation rates for carbonate bedrock samples in the previous studies.

#	Reference	Type	Name	latitude	longitude	elevation	Precipitation	Denudation rate		
			-	dd	dd	m	mm	mm/kyr		
176	Ryb et al. (2014b)	Bedrock-hillslope	SQ3	31.7634	35.0688	415	579.00	17.00	±	1.7
177	Ryb et al. (2014b)	Bedrock-hillslope	SQ4	31.7681	35.0737	649	584.00	28.00	±	2.8
178	Ryb et al. (2014b)	Bedrock-hillslope	SQ5	31.7652	35.0728	549	579.00	22.00	±	2.2
179	Ryb et al. (2014b)	Bedrock-hillslope	SQ6a	31.7489	35.0606	625	564.00	22.00	±	2.2
180	Ryb et al. (2014b)	Bedrock-hillslope	SQ7	31.7505	35.0613	564	566.00	34.00	±	3.4
181	Ryb et al. (2014b)	Bedrock-hillslope	SQ8	31.7513	35.0642	450	570.00	51.00	±	5.1
182	Ryb et al. (2014b)	Bedrock-hillslope	SQ9	31.7516	35.0652	406	570.00	22.00	±	2.2
183	Ryb et al. (2014b)	Bedrock-hillslope	SQ10	31.7355	35.1756	770	502.00	15.00	±	1.5
184	Ryb et al. (2014b)	Bedrock-hillslope	SQ11	31.7358	35.1738	733	504.00	25.00	±	2.5
185	Ryb et al. (2014b)	Bedrock-hillslope	SQ12	31.7355	35.1731	713	511.00	17.00	±	1.7
186	Ryb et al. (2014b)	Bedrock-hillslope	SQ13	31.7364	35.171	657	512.00	6.00	±	0.6
187	Ryb et al. (2014b)	Bedrock-hillslope	SQ14	31.7369	35.1705	641	512.00	13.00	±	1.3
188	Ryb et al. (2014b)	Bedrock-hillslope	SQ15	31.8126	35.1617	788	627.00	26.00	±	2.6
189	Ryb et al. (2014b)	Bedrock-hillslope	SQ16	31.8115	35.163	748	619.00	24.00	±	2.4
190	Ryb et al. (2014b)	Bedrock-hillslope	SQ17	31.811	35.1649	703	609.00	33.00	±	3.3
191	Ryb et al. (2014b)	Bedrock-hillslope	SQ18	31.8106	35.1674	660	609.00	35.00	±	3.5
192	Ryb et al. (2014b)	Bedrock-hillslope	SQ19	31.8099	35.1684	609	609.00	28.00	±	2.8
193	Ryb et al. (2014b)	Exposed bedrock/interfluve	UB1	31.7708	35.1974	765	525.00	20.00	±	2
194	Ryb et al. (2014b)	Exposed bedrock/interfluve	UB3	31.7709	35.0542	727	574.00	28.00	±	2.8
195	Ryb et al. (2014b)	Exposed bedrock/interfluve	UB5	31.7814	35.1451	699	601.00	54.00	±	5.4
196	Ryb et al. (2014b)	Exposed bedrock/interfluve	UB7	31.7632	35.022	344	546.00	20.00	±	2
197	Ryb et al. (2014b)	Exposed bedrock/interfluve	UB9	31.7656	35.0268	475	549.00	18.00	±	1.8
198	Ryb et al. (2014b)	Exposed bedrock/interfluve	UB11	31.767	35.0364	543	553.00	19.00	±	1.9
199	Ryb et al. (2014b)	Exposed bedrock/interfluve	UB13	31.7514	35.0418	654	550.00	15.00	±	1.5
200	Ryb et al. (2014b)	Exposed bedrock/interfluve	UB15	31.7252	35.0141	361	522.00	15.00	±	1.5
201	Ryb et al. (2014b)	Exposed bedrock/interfluve	UB17	31.7242	35.0198	451	525.00	13.00	±	1.3
202	Ryb et al. (2014b)	Exposed bedrock/interfluve	UB19	31.7238	35.0235	515	528.00	14.00	±	1.4
203	Ryb et al. (2014b)	Exposed bedrock/interfluve	UB21	31.7262	35.0515	614	546.00	15.00	±	1.5
204	Ryb et al. (2014b)	Exposed bedrock/interfluve	UB23	31.726	35.1562	846	543.00	29.00	±	2.9
205	Ryb et al. (2014b)	Exposed bedrock/interfluve	UB25	31.718	35.1219	787	586.00	17.00	±	1.7
206	Xu et al. (2013)	Bedrock-flat	GZCl-3	26.4012	106.5286	1226	1150.00	44.00		
207	Xu et al. (2013)	Bedrock-flat	GZCl-4	26.4758	106.9644	1110	1050.00	40.00		
208	Xu et al. (2013)	Bedrock-flat	GZCl-5	26.9742	104.5183	2329	900.00	41.00		
209	Xu et al. (2013)	Bedrock-flat	GZCl-7	26.6977	104.7101	1959	1250.00	47.00		
210	Xu et al. (2013)	Bedrock-flat	GZCl-9	27.8801	108.3038	586	1150.00	17.00		
211	Xu et al. (2013)	Bedrock-flat	GZCl-10	28.0976	108.3222	577	1180.00	19.00		
212	Matsushi et al. (2010)	Bedrock-flat	Nt-2A	44.9890	142.3363	133	1280.00	55.00	±	4

Table A. 3 (continued) : Compilation of ^{36}Cl-derived denudation rates for carbonate bedrock samples in the previous studies.

#	Reference	Type	Name	latitude	longitude	elevation	Precipitation	Denudation rate		
			-	dd	dd	m	mm	mm/kyr		
213	Matsushi et al. (2010)	Bedrock-flat	Nt-3.2A	44.9890	142.3311	104	1280.00	24.00	±	2
214	Matsushi et al. (2010)	Bedrock-flat	Sb-1A	44.0923	142.5781	611	1003.00	25.00	±	1
215	Matsushi et al. (2010)	Bedrock-flat	Sb-3.2A	44.0922	142.5741	524	1003.00	60.00	±	4
216	Matsushi et al. (2010)	Bedrock-flat	Iz-3A	39.9321	141.7443	778	1049.00	38.00	±	2
217	Matsushi et al. (2010)	Bedrock-flat	Iz-5A	40.0657	141.7088	490	1049.00	34.00	±	2
218	Matsushi et al. (2010)	Bedrock-flat	Tn-2A	39.1781	141.5762	594	1171.00	31.00	±	2
219	Matsushi et al. (2010)	Bedrock-flat	Tn-3A	39.1766	141.5765	614	1171.00	39.00	±	3
220	Matsushi et al. (2010)	Bedrock-flat	Ab-2A	37.3581	140.6695	851	1230.00	20.00	±	1
221	Matsushi et al. (2010)	Bedrock-flat	Ab-3A	37.3585	140.6698	855	1230.00	43.00	±	3
222	Matsushi et al. (2010)	Bedrock-flat	Ab-4A	37.3496	140.6738	834	1230.00	28.00	±	1
223	Matsushi et al. (2010)	Bedrock-flat	Ak-1D	34.2650	131.3061	401	2001.00	22.00	±	2
224	Matsushi et al. (2010)	Bedrock-flat	Ak-4A	34.2528	131.3183	336	2001.00	31.00	±	2
225	Matsushi et al. (2010)	Bedrock-flat	Hr-2C	33.76		432	1800.00	28.00	±	3
226	Matsushi et al. (2010)	Bedrock-flat	Hr-3B	33.7644	130.9078	487	1800.00	23.00	±	1
227	Matsushi et al. (2010)	Bedrock-flat	Hd-1B	26.8544	128.2578	248	2479.00	49.00	±	3
228	Matsushi et al. (2010)	Bedrock-flat	Ym-2B	26.6747	127.9172	219	2086.00	48.00	±	4
229	Stone et al. (1994)	Bedrock-flat	Buchan	-37.1500	147.6000	800	650	18	±	3
230	Stone et al. (1994)	Bedrock-flat	Buchan	-37.1500	147.6000	800	650	19	±	3
231	Stone et al. (1994)	Bedrock-flat	Buchan	-37.1500	147.6000	800	650	25	±	4
232	Stone et al. (1994)	Bedrock-flat	Yarrangobilly	-36.1800	147.8900	290	809	22	±	3
233	Stone et al. (1994)	Bedrock-flat	Yarrangobilly	-36.1800	147.8900	290	809	26	±	3
234	Stone et al. (1994)	Bedrock-flat	Yarrangobilly	-36.1800	147.8900	290	809	29	±	3
235	Stone et al. (1994)	Bedrock-flat	Tindal	-14.4400	133.2400	260	1089	14	±	3
236	Stone et al. (1994)	Bedrock-flat	Nullarbor Plain	31.6800	128.9000	100	274	4.5	±	0.7

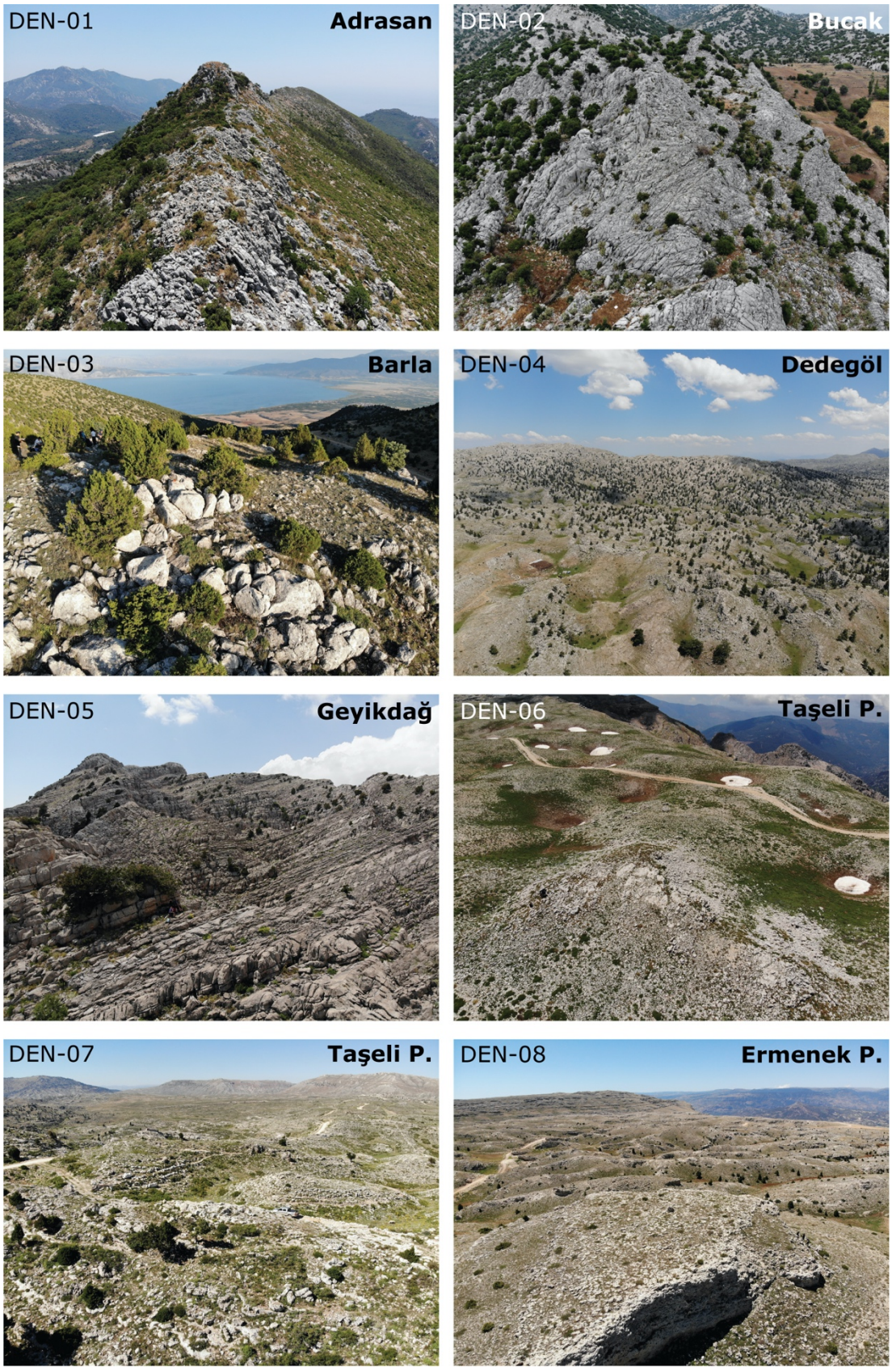

Figure A. 1 : Field photos of sampling locations. P. stands for plateau.

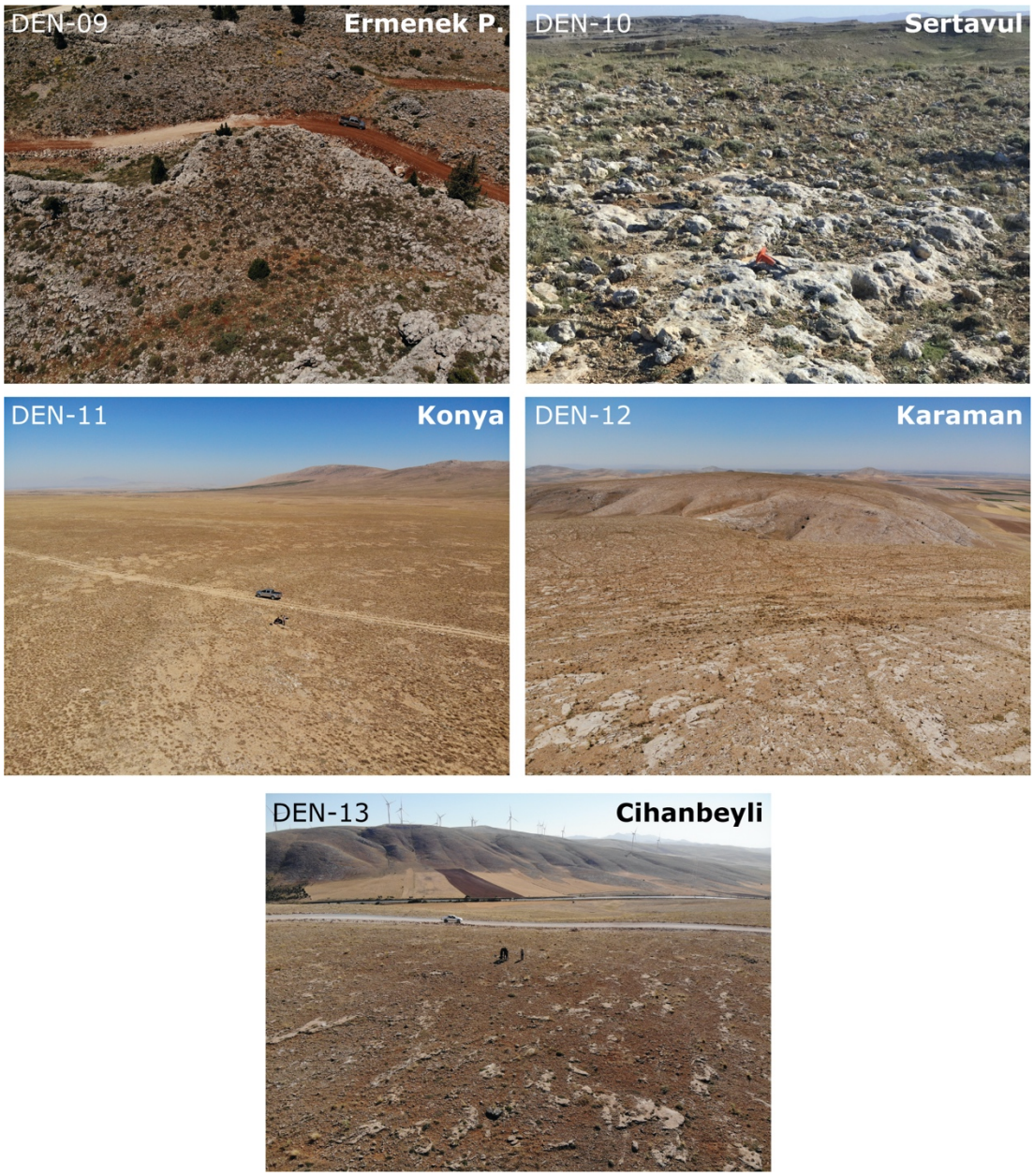

Figure A.1 (continued) : Field photos of sampling locations. P. stands for plateau.

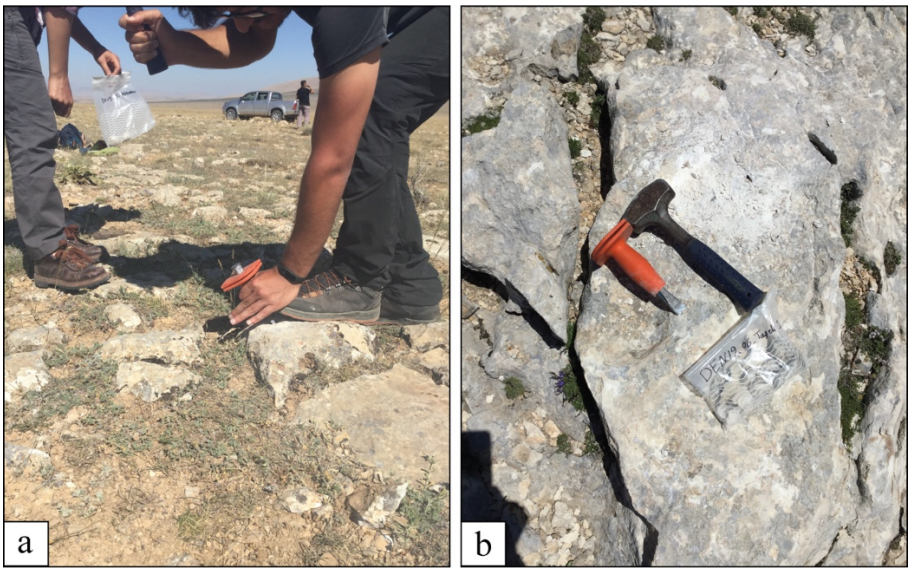

Figure A. 2 : Sampling carbonate bedrocks for quantifying denudation rates.

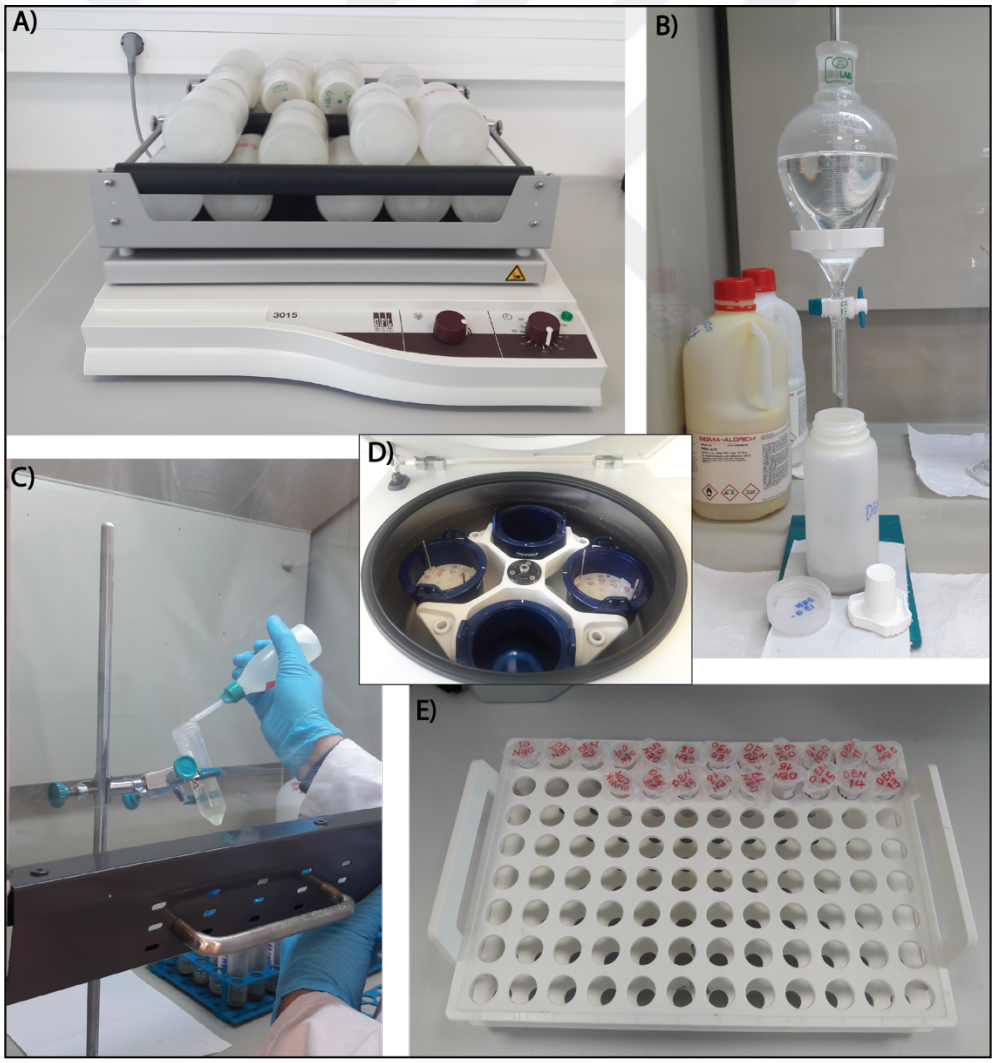

Figure A. 3 : Some steps of sample preparation: A) Leaching with MilliQ water, B) Leaching with 10 % HNO_3, C) First Chlorine extraction, D) The final centrifuge to precipitate AgCl, E) AgCl precipitation in labeled Teflon vial.

APPENDIX B: Additional information on Schmidt Hammer measurements

Table B. 1 : Schmidt Hammer measurements in each sampling location.

Sample Name	Number of Impacts																				R Values
	#1	#2	#3	#4	#5	#6	#7	#8	#9	#10	#11	#12	#13	#14	#15	#16	#17	#18	#19	#20	
TestMarble.BF	53	52	54	54	54	56	54	54	54	56	52	52	50	52	54	54	55	55	51	54	54.6
DEN19-01	35	42	52	36	22	44	36	48	54	50	45	40	50	49	48	48	50	44	38	30	49.4
DEN19-02	56	54	52	34	55	28	24	56	52	47	52	30	42	43	50	54	45	28	51	39	53.2
DEN19-03	45	49	49	33	41	50	48	45	46	31	45	43	50	44	43	47	39	41	43	41	47.4
DEN19-04	47	22	47	29	22	25	28	32	42	46	45	43	40	33	47	46	29	36	31	42	44.5
DEN19-05	19	35	26	31	19	46	43	21	36	36	37	47	27	41	47	41	40	46	28	33	42.4
DEN19-06	24	22	26	26	24	34	32	50	38	36	38	44	44	38	34	35	33	29	25	20	39.1
DEN19-07	20	26	35	28	24	32	18	24	24	33	34	32	30	25	21	35	30	26	21	27	31.6
DEN19-08	44	43	19	17	44	47	35	18	21	37	18	48	40	23	44	31	42	43	30	29	43.2
DEN19-09	32	28	22	20	46	20	36	40	15	18	34	46	16	20	20	20	34	33	32	32	36.5
DEN19-10	30	34	18	30	38	36	20	31	35	21	42	18	30	18	31	38	18	28	35	19	35
DEN19-11	45	18	23	44	27	26	17	20	25	21	48	42	37	48	49	44	40	52	53	50	47.5
DEN19-12	48	20	25	22	46	45	55	44	22	49	27	26	44	52	30	49	21	47	48	48	48.7
DEN19-13	30	52	24	47	50	48	18	20	50	48	56	47	46	50	46	53	49	55	51	51	51.7
TestMarble.AF	50	52	54	54	52	54	49	50	53	51	52	52	50	52	49	48	52	51	51	50	52.7

Figure B. 1 : Schmidt Hammer measurements in the field.

APPENDIX C: Published papers related to this thesis

- **Hashemi, A.,** Sarıkaya, M. A., Wilcken, K. M., and Öztürk, M. Z. (2023). Controls on long-term denudation rate of carbonate terrains in the Eastern Mediterranean. *Quaternary Science Reviews*, *321*, 108351. https://doi.org/10.1016/j.quascirev.2023.108351
- **Hashemi, A.,** Sarıkaya, M. A., Görüm, T., Wilcken, K. M., Ciner, A., Žebre, M., ... and Yıldırım, C. (2022). The Namaras rock avalanche: Evidence of mid-to-late Holocene paraglacial activity in the Central Taurus Mountains, SW Turkey. *Geomorphology*, *408*, 108261. https://doi.org/j.geomorph.2022.108261

CURRICULUM VITAE

Name Surname **:** Ayda HASHEMI

EDUCATION **:**

- **B.Sc.:** 2005, University of Tabriz, Faculty of Natural Sciences
- **M.Sc. :** 2010, Geological Survey of Iran, Research Institute for Earth Sciences

PROFESSIONAL EXPERIENCE AND REWARDS:

- November 2019– August 2020: Istanbul Technical University Scientific Research Project Unit, **BAP** Project [grant number **MDK-2019-42116**]. I recived bursary fund.
- December 2018– October 2019: **TÜBİTAK** project No. **118Y052**. I took part in the project and received bursary fund.
- October 2011– June 2015: Teaching geology at high school.

PUBLICATIONS ON THE THESIS

- **Hashemi, A.,** Sarıkaya, M. A., Wilcken, K. M., & Öztürk, M. Z. (2023). Controls on long-term denudation rate of carbonate terrains in the Eastern Mediterranean. *Quaternary Science Reviews*, *321*, 108351. https://doi.org/10.1016/j.quascirev.2023.108351
- **Hashemi, A.,** Sarıkaya, M. A., Görüm, T., Wilcken, K. M., Ciner, A., Žebre, M., Stepišnik, U., Yıldırım, C. (2022). The Namaras rock avalanche: Evidence of mid-to-late Holocene paraglacial activity in the Central Taurus Mountains, SW Turkey. *Geomorphology*, *408*, 108261. https://doi.org/10.1016/j.geomorph.2022.108261

PRESENTATIONS ON THE THESIS

- **Hashemi K.,** Sarıkaya M. A., Wilcken K. M., Öztürk M. Z., Çiner A. (2022) Long-term denudation rate of carbonate terrains in the southern part of Central Anatolian Plateau. X. Quaternary Symposium of Turkey, 2-4 November 2022, Istanbul Technical University-Eurasia Institute of Earth Sciences, Istanbul / Türkiye
- **Hashemi, K.,** Sarıkaya, M. A., and Wilcken, K. M.: Defining denudation rate of carbonate rocks using cosmogenic ^{36}Cl in the Taurus Mountain, S-SW Turkey, EGU General Assembly 2021, online, 19–30 Apr 2021, EGU21-2915, https://doi.org/10.5194/egusphere-egu21-2915, 2021

- **Hashemi, K.,** Sarıkaya, M. A. (2020). Defining long-term denudation rates of carbonate rocks by cosmogenic ^{36}Cl in the Taurus Mountain, Turkey. IX. Quaternary Symposium of Turkey, 20-23 October 2020, Istanbul Technical University-Eurasia Institute of Earth Sciences, Istanbul / Türkiy

OTHER PUBLICATIONS:

- **Hashemi, K.,** Oveisi, B., & Saeedi, A. (2014). Offering a Kinematic Model for Lar Fault-Related Fold and Its Structural Relation with 1960 Lar Earthquake, SE Zagros. Scientific Quarterly Journal of Geosciences, 24(93), 9-18 (In Persion). https://doi.org/10.22071/gsi.2014.43442
- **Hashemi, K.,** Oveisi, B., & Saeedi, A. (2013). Kinematic Analysis of Geomorphic Markers and Estimation of the Relative Rate of Active Deformations along the Hormud Quaternary Fault-East of Central Zagros. Scientific Quarterly Journal of Geosciences, 22(86), 135-142 (In Persion). https://doi.org/10.22071/gsi.2012.54078